Title
Controlling the Dynamics of Nanoscopic Matter with Electromagnetic Fields

Author
Li, Haokun

Publication Date
2019

Peer reviewed|Thesis/dissertation

Controlling the Dynamics of Nanoscopic Matter with Electromagnetic Fields

By

Haokun Li

A dissertation submitted in partial satisfaction of the
requirements for the degree of
Doctor of Philosophy
in
Applied Science and Technology
and the
Designated Emphasis
in
Nanoscale Science and Engineering
in the
Graduate Division
of
University of California, Berkeley

Committee in charge:
Professor Xiang Zhang, Chair
Professor Hartmut Haeffner
Professor Ming C. Wu
Professor Alex Zettl

Spring 2019

Abstract

Controlling the Dynamics of Nanoscopic Matter with Electromagnetic Fields

by

Haokun Li

Doctor of Philosophy in Applied Science and Technology

with the Designated Emphasis in Nanoscale Science and Engineering

University of California, Berkeley

Professor Xiang Zhang, Chair

The electromagnetic force is one of the four basic interactions discovered in nature and it plays an essential role in determining the internal properties of most matter seen in daily life. In this dissertation, we present the endeavor on exploiting electromagnetic fields to actively control the dynamics of various nanoscopic matter, including atomic ion rings, monolayer semiconductors, and nanomechanical membranes. The achieved controls open up unique opportunities to study fundamental many-body quantum physics and to facilitate information and energy transfer processes at the nanoscale.

This dissertation consists of three sets of experiments. 1. We design and fabricate a surface-electrode Paul trap and confine up to fifteen $^{40}Ca^{+}$ ions into a microscopic ring using radio-frequency electric fields. The achieved unprecedented circular symmetry enables the first observation of localization-delocalization transitions of ion rings at millikelvin temperatures. 2. We propose and demonstrate a scheme to couple electron valley degree-of-freedom with macroscopic mechanical motion using a magnetic field gradient perpendicular to suspended monolayer semiconducting transition metal dichalcogenides (for example MoS_2). Direct transduction of valley excitation into mechanical states is realized for the first time. 3. We perform the first experiment to probe and manipulate the phonon energy transfer driven by quantum fluctuations of electromagnetic fields (the Casimir effect). With a delicate approach to place two nanomechanical membranes parallel and close to each other, we realize the first strong Casimir phonon coupling condition and thus observe the thermal energy exchange across vacuum between individual phonon modes.

Dedicated to my parents

Xinghui Wu & Tanping Li

Dedicated to my wife

Xuexin Ren

Contents

List of Figures

parabolic dependence on the bias voltage between the membranes (solid curves are parabolic fits). The curvatures of the parabolas are proportional to the electrostatic interaction strength, which have a distance dependence of d^{-3} according to the Coulomb law. We determine the frequency splitting by fitting the two peak positions in the spectra, which gives a precision of ~1 Hz (smaller than the data markers).

Figure 7.3.2 | Dependence of electrostatic strength (**a**) and minimum splitting voltage V_0 (**b**) on the distance between the membranes.

Figure 7.3.3 | The minimum frequency splitting for each distance shows a dependence of $d^{-4.91\pm0.12}$. This power law verifies that the Casimir interaction is dominant over the electrostatic interaction in our measurement.

Figure 7.4.1 | **a,** Because of the Casimir interaction, the mode temperatures deviate from their bath temperatures when the two membranes are brought close. At d < 400 nm, T_1' and T_2' become nearly identical, showing thermalization of the two phonon modes. The mode temperatures are measured from the thermal Brownian motion $k_B T_i' = m_i \Omega^2 \langle z_i^2 \rangle$. The error bars represent the standard error determined by ~4 hours' continuous measurement. The data agrees well with the calculation using coupled-mode Langevin equations (solid lines). **b, c,** The measured quadrature components of the thermal displacement of phonon modes 1 (**b**) and 2 (**c**) at mode temperatures $T_1' = 287.0$ K and $T_2' =$ 312.5 K, respectively. Dashed lines indicate the standard deviations of the distriubtions and the enclosed areas are proportional to the mode temperatures. **d,** Probability distributions of the phonon mode energy follow the statistics of a canonical ensemble $P(E_i) \propto e^{-E_i/k_B T_i'}$ represented by the solid lines.

Figure 7.4.2 | When the frequency offset $(\Omega_2 - \Omega_1)$ is much larger than the linewidths of the modes, the mode temperatures T_1' and T_2' keep the same as their bath temperatures and no heat transfer effect is observed. Here, the distance between the membrane is d = 430 nm.

Figure 7.5.1 | | Frequency shifts of the two modes versus the distance (**a**). In (**b**), the Casimir force contribution is excluded. Measurement is performed at bath temperatures T_1 = 287.0 K and T_2 = 312.5 K, and the frequencies of the modes are offset by ~250 Hz.

Figure 7.5.2 | | Distance dependence of the ratio between the radiation pressure driven by thermal fluctuations and the Casimir pressure driven by quantum fluctuations.

Acknowledgements

First, I would like to express my deepest gratefulness to my advisor, Professor Xiang Zhang, for shaping my vision in research and providing me all the freedom and resources to pursue science. Your constant enthusiasm, perseverance, confidence, and crave for innovation have rooted deep in my soul.

Thank you every former and present member in Xlab, who devoted their passion in science and created such a dynamic and flourishing research environment. The inspiring discussions in group meetings and seminars from broad perspectives echo continually in my mind. In particular, I would like to thank my mentors and collaborators, including Dr. King Yan Fong, Dr. Hamidreza Ramizani, and Dr. Tongcang Li, for generously sharing your knowledge and skills and for serving as fantastic role models of different research styles. I am also grateful to Dr. Yuan Wang and Dr. Sui Yang for their precious guidance and tremendous lab service.

I am grateful to Professor Hartmut Haeffner for serving my prelim/thesis committee and for being a great physics mentor and a wonderful collaborator. Many thanks also go to his group members Erik Urban, Crystal Noel, Maya Berlin-Udi, and Dr. Borge Hemmerling.

Many thanks to Prof. Ming Wu, Prof. David Attwood, Prof. Feng Wang, Prof. Joel Moore, Prof. Irfan Siddiqi, Prof. Jie Yao, and Prof. Alex Zettl for being my prelim/qualify/thesis committee. Those hot debates and interactions are truly inspiring and influential.

I would like to thank my buddies at Berkeley including Yi Chen, Xiaoya Qu, Qian Zhong, Siqi Wang, Ying Wang, Jun Xiao, Yang Xia, Weidi Zhu, Hanyu Zhu, for your friendship, and for the days and nights we spent on climbing, hiking, skiing, rafting, as well as eating, drinking, cooking, and gaming. Your company and encouragement are invaluable to me.

I would like to dedicate my sincere gratitude to my parents and my entire family, for your endless love and support. Thank you so much for the strength you have given me over the years. I hope I make you proud.

Finally, I am deeply indebted to my wife Xuexin Ren. It has been a marvelous adventure with you from Beijing to Berkeley. As lovers, friends, and labmates, we share our happiness and experience various aspects of life. I cannot imagine PhD life without you. Our days at 928 San Benito are destined to be remembered.

Chapter 1

Introduction

Our quest to understand how electromagnetic fields interact with matter and affect the internal thermal, electrical, and mechanical properties of materials has been a fruitful journey for several centuries. On the other hand, huge success has also been made by actively using electromagnetic force to control the movement of matter for promoting our understanding of the physical world and for realizing a variety of technological applications. In accelerator physics, oscillating electromagnetic fields are implemented to generate high energy particle beams, with which new particles have been produced and discovered. In atomic physics, optical tweezers and laser cooling technologies have led to the observation of new phases of matter (for example Bose-Einstein condensation) and extremely precise clocks with neutral atoms. The electrodynamic ion traps have enabled us to explore quantum mechanics down to single particle level and to perform quantum information processing. In nuclear reactors, strong magnetic fields are manipulated to confine hot plasmas for generating thermonuclear fusion power. Electromagnetically actuated micro/nano electromechanical systems (NEMS /MEMS) have been widely used in many areas, such as sensing, switching, biological studies, and wireless communications.

This dissertation presents continued efforts in this context, on using electromagnetic fields to control the dynamics of various nanoscopic matter, including atomic ion rings, monolayer semiconductors, and nanomechanical membranes. We have achieved unprecedented control of those matter and observed exotic physical phenomena. 1. We confined up to fifteen atomic ions into a microscopic ring and observed the localization to delocalization transitions at millikelvin temperature. 2. We realized valley-mechanical coupling and directly transduced electron valley excitation into macroscopic mechanical motion in suspended monolayer semiconductors. 3. We realized strong phonon coupling induced by the Casimir force and observe the resulting phonon thermal energy transfer between nanomechanical membranes. These experimental results and technological developments open up new realms to explore many-body quantum physics, and to facilitate information and energy transfer processes at the nanoscale.

1.1 Controlling the dynamics of atoms and nanomaterials

1.1.1 Atom trapping and cooling

The study of the intrinsic properties of atoms is a highly fruitful area of scientific research. Nearly a century ago, such inquiry led to the formulation of quantum mechanics, one of the cornerstones of modern physics. Since then, measurements with atoms continuously shed light on fundamental physics, such as relativity and quantum field theory.

The successfulness of understanding matter by probing atomic systems highly depends on the capability to make precise measurement and control. However, the desired precision and control cannot be easily accessed. In solids or liquids, one cannot isolate individual atoms from their neighbors. In atomic gases, thermal motions strongly disturb the measurement.

In light of this, laser cooling and atom trapping technologies were developed in the 1980s, including optical trapping of neutral atoms and electrodynamic trapping of charged ions. These technologies revolutionize the spectroscopy measurements of atoms. Gigantic success has been achieved in making extremely precise atomic clocks and probing fundamental physical constants, which further bring insights to the frontier of high energy physics.

The delicate control of atomic movements has also led to huge triumphs in creating and observing new quantum phases of matter. Significant examples include Bose-Einstein condensation and Mott insulator to superfluid transition. As far as we know, nearly all quantum phases of matter under exploration can be interpreted as a result of symmetry breaking [1]. In brief, the equations of motions are invariant under certain symmetry operations while physical consequences are not. Usually, the consequences of invariance are studied in large systems (for example condensed matter systems [2] and optical lattices of cold atoms [3]) to suppress edge effects which can cause undesired symmetry breaking. This approach works for investigating global properties, however, it is difficult to be used for probing local observables and their correlations, which are the critical aspects of quantum matter.

To this end, quantum systems that naturally embody symmetry (or invariance) and allow for single particle control are much desired. Through the implementation of periodic boundary conditions, one can hope to realize translational symmetry in small systems where single-particle control is achievable. This quest motivates us to confine cold ions into a ring shape and establish exquisite control [4].

1.2.1 Nanoelectromechanical systems

The first reported electromechanical device dated back to 1785. In the measurement of electrical charge, Coulomb used an electrical torsion balance which consisted of two metal balls – one of which was fixed, the other attached to a moving rod that acted as capacitor plates, converting a charge difference into an attractive force. This device illustrates the two main components in most electromechanical systems: a mechanical element and a transducer. The mechanical element either deflects or vibrates in response to an electromagnetic force. These mechanical outputs are then detected by a readout transducer.

With the advancement of nanofabrication and the emergence of nanomaterials (for example carbon nanotube and graphene), electromechanical devices have been tremendously scaled down. The miniaturization gives rise to many advantages of nanoelectromechanical systems, such as ultrasmall mass, ultrahigh resonance frequency, and ultralow mechanical dissipation. These properties bring excellent performance in information processing (high speed and low power) and sensing (approaching the quantum limit). Nowadays, nanoelectromechanical systems are playing important roles in wireless radio-frequency communications and studies of biology, chemistry, and quantum physics [5-7].

One important social drive for nanoscience is from the information aspect, which demands increasing functionalities and scaling. Utilizing the electron valley degree-of-freedom (local minima in the band structure of solids) as a new type of information carrier, recently emerged valleytronics promises exciting applications in computation and communication beyond conventional electronics and spintronics [8,9]. A fruitful scientific question becomes how to transfer valley information to mechanical motion? To this end, we realize valley-mechanical coupling and demonstrate the first transduction of valley excitation into mechanical states in suspended monolayer semiconducting MoS_2 [10].

Another important motivation for nanoscience is from the energy perspective, which quests for increasing efficiency and sustainability. At nanoscale, quantum mechanical effects play important roles in many aspects. How do they affect the energy transfer processes [11-13], and how can we utilize them to facilitate and manage energy transfer? With this motivation, we perform the first experiment using nanomechanical systems to probe and control the phonon coupling and thermal energy transfer driven by the quantum vacuum fluctuations of electromagnetic fields (the Casimir effect) [14].

1.2 Fundamentals of electromagnetic force

Electromagnetic fields can exert force onto matter and affect their movements [15]. Consider a single particle with charge q moving with a velocity **v** in an electric field **E** and a magnetic field **B**, the force is given by the Lorentz formula

$$\mathbf{F} = q\mathbf{E} + q\mathbf{v} \times \mathbf{B}. \tag{1.2.1}$$

For a continuum with charge and current densities ρ and **J**, the force density **f** (force per unit volume) can be written as

$$\mathbf{f} = \rho\mathbf{E} + \mathbf{J} \times \mathbf{B}. \tag{1.2.2}$$

By introducing the Maxwell stress tensor

$$\mathrm{T}_{ij} = \epsilon_0 \left(E_i E_j - \frac{1}{2}\delta_{ij} E^2 \right) + \left(B_i B_j - \frac{1}{2}\delta_{ij} B^2 \right) / \mu_0 \tag{1.2.3}$$

and the Pointing vector

$$\mathbf{S} = (\mathbf{E} \times \mathbf{B})/\mu_0 \tag{1.2.4}$$

the electromagnetic force can be calculated by

$$\mathbf{f} = \nabla \cdot \mathbf{T} - \frac{1}{c^2}\frac{\partial \mathbf{S}}{\partial t}. \tag{1.2.5}$$

The above equation describes the momentum conservation law in classical electrodynamics, where $\nabla \cdot \mathbf{T}$ is the momentum flux density. We note that the equation assumes complete knowledge of both ρ and **J** (both free and bounded charges and currents). For the case of nonlinear materials, the nonlinear Maxwell stress tensor must be used.

Equation (1.2.3) provides a convenient way to calculate the electromagnetic force on objects with complex shape, by evaluating the integral of the stress tensor on the surfaces. With the development of computational electrodynamics modeling techniques and the advancement of computation power and resource, larger and more complex structures can be numerically simulated today.

1.3 Thesis overview

This dissertation is summarized into three parts: 1. Realization of translational invariant cold ion rings. 2. Valley-mechanical transduction. 3. Casimir phonon coupling and heat transfer.

In Chapter 2, we introduce the design considerations on achieving circular symmetric ion rings using surface-electrode Paul trap. We then describe the fabrication process flow of the silicon ring trap which has electrical vias through glass substrate. In Chapter 3, we explore the dynamics of laser cooled microscopic ion rings, including the common oscillations and localization to delocalization transitions. Both experimental results and numerical simulation are presented.

In Chapter 4, we introduce our design for realizing valley-mechanical coupling in monolayer transition metal dichalcogenides through the use of a strong perpendicular magnetic field gradient. Chapter 5 describes our experiments on achieving valley-mechanical transduction. We fabricate suspended monolayer MoS_2 resonators with both dry transfer and critical point dry methods. In the optical interferometric measurement, we implement a double lock-in technique to single out the valley-actuated mechanical motion. We present effective control of valley-mechanical interaction by adjusting the pump light, magnetic field gradient, and temperature.

In Chapter 6, we discuss our experimental design to realize phonon coupling and thermal transfer driven by the Casimir force. We analyze the dynamics with coupled-mode Langevin equations. Chapter 7 describes our experimental implementations and observations. We fabricate nanomechanical membranes with lateral dimensions of ~300 μm and align them in parallel with high precision ($<10^{-4}$ rad) using optical and electrical methods. We bring the nanomembranes as close as ~300 nm. A double optical interference setup with multiple feedback loops controlling the membrane distance, resonance frequency, and detection sensitivity is constructed, and successfully identifies the strong phonon coupling and thermal energy transfer induced by the Casimir force.

1.4 Summary of key results

The key results of this dissertation are summarized in the following. 1. We trap atomic ions into a microscopic ring and preserve the circular symmetry at millikelvin temperatures [4]. 2. We realize direct transduction of electron valley excitation into mechanical motion in monolayer MoS_2 resonators [10]. 3. We utilize nanomechanical systems to realize strong phonon coupling driven by the Casimir force, and observe the resulting thermal energy exchange between individual phonon modes [14].

Chapter 2

Towards freely rotating cold ion rings

2.1 Background and motivation

Due to the strong interactions between charge and electromagnetic fields, charged particles can be tightly confined in vacuum. Significant examples are the Paul trap using oscillating electric fields and Penning trap combining static electric and magnetic fields [16,17]. With the revolutionary development of laser cooling and laser spectroscopy over the past several decades, both the internal electronic and external motional degrees-of-freedom of trapped ions are now controllable down to the single quantum level [18].

Today, trapped ions are playing significant roles in studies of many-body physics, quantum information processing, and precision measurements. While most experiments are carried out with linear ion strings, a particularly interesting structure is a ring of ions which ideally would exhibit circular symmetry and periodic boundary condition. Many exciting theoretical proposals with ion rings have emerged over the past decade [19-25], including the simulation of Hawking radiation, the exploration of quantum phase transition, and the test of symmetry breaking with indistinguishable particles. However, experimental investigation remains at a standstill because of the long-standing challenge to preserve the symmetry of ion rings at low temperatures [26-29]. Overcoming such a challenge and creating freely rotating cold ion rings thus become the critical requirement to stimulate further research.

This Chapter presents the design and fabrication of a new surface-electrode microscopic ring Paul trap. With this implementation, the circular symmetry of the ion ring is preserved at laser cooling temperatures (millikelvin) and can potentially maintained much further [4], as demonstrated by our experiments discussed in the following Chapter. This quantum system opens up a new regime to explore many-body quantum physics with translational invariance where individual particles can be accessed and controlled. In addition, the symmetry and periodicity of the ion ring provide a unique platform to explore quantum computing and quantum simulation.

2.2 Introduction to Paul trap

Maxwell equations forbid trapping of a charged particle using only static electric fields. The idea of utilizing oscillating electric fields to dynamically confine charged particles was pioneered by Wolfgang Paul in 1953. To illustrate the concept, we consider a plane $x-y$ with a set of radio-frequency (RF) electrodes, as shown in Fig. 2.1.1. At any instant of time, the charged particle experienced a quadrupole potential

$$U(x,y,t) = U_0(x,y)\cos(\Omega_{\mathrm{RF}}t). \tag{2.1.1}$$

The fast oscillating potential effectively shakes the ion back and forth, resulting in a dipole moment of the moving particle. The induced dipole moment is then pulled by the electric field gradient toward the saddle point (the RF null), where electric field gradient is zero. When the electric field oscillation is much faster than the motion of the charged particle, the process can be described with a pseudo potential

$$\Phi(x,y) = Q^2|\nabla U_0(x,y)|^2/4M\Omega_{\mathrm{RF}}^2, \tag{2.1.2}$$

where Q and M are the charge and mass of the particle. The principle can be extended to design traps with various geometries. In recent years, the goal of building scalable quantum information processors has triggered the rapid development of chip-based ion traps [30], where the electrodes are patterned onto surfaces using current semiconductor manufacturing technologies.

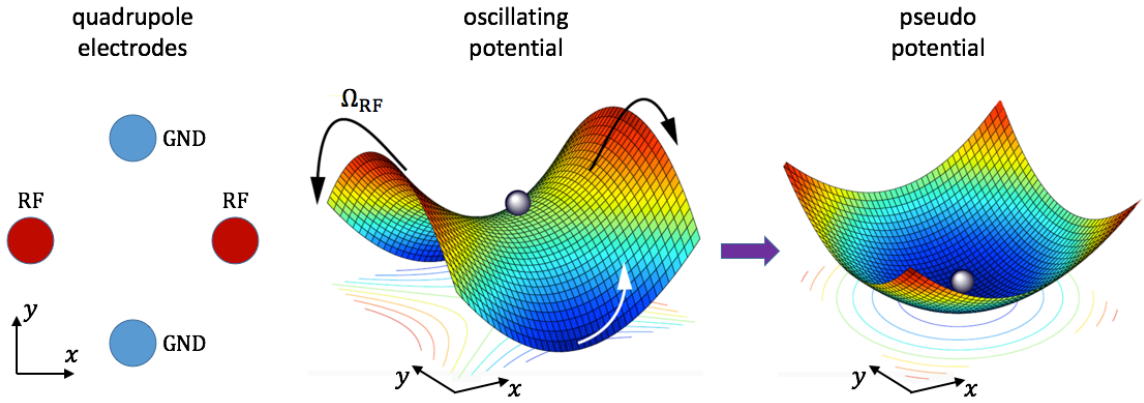

Figure 2.1.1 | The left figure shows the standard quadruple electrode configuration for Paul trap. The middle figure describes the oscillating potential generated by the RF electrodes. Effectively, the charged particle experiences a pseudo potential (right figure). The potential profile is adapted from Ref. [31].

2.3 Surface trap with circular symmetric potential

By implementing circular symmetry to the trap design, one can in principle confine ions into a ring shape. However, in all previous experimental attempts [26-29], because the ion-electrode distances were much smaller than the ion ring diameters, the complex stray electric fields from the trap electrodes substantially disrupt the circular symmetry, as described in Fig. 2.2.1. In our new design [32,33], we address this issue by reducing the ion-ring diameter while keeping the ions far away from the electrodes, such that stray fields from imperfections vary on length scales larger than the ring diameter. This strategy avoids local distortions of the ion ring. The residue global effect can thus be easily compensated with mainly homogeneous electric field.

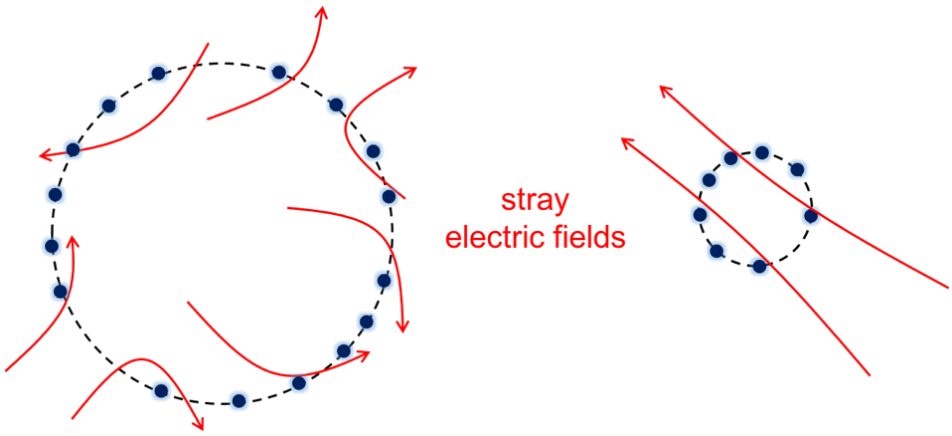

Figure 2.2.1 | The symmetry of the ion ring was disrupted by complex stray electric fields in previous experimental implementations (left). We address this issue by making a small ion ring far from the trap surface. The stray electric fields affect the ion ring in a global manner and thus can be easily compensated (right).

Our chip-based surface-electrode ring trap consists of three concentric circular electrodes surrounded by eight static-voltage compensation electrodes as shown in Fig. 2.2.2. Applying an RF voltage to the innermost and outermost circular electrodes with all other electrodes held at a DC voltage generates a time-averaged circular potential minimum 400 μm above the trap surface. The two radial directions at the time-averaged potential minimum are degenerate according to the symmetry of Maxwell equations. The outer radius of the three circular electrodes are designed to be 125, 600, and 1100 μm, respectively. The gap between the innermost and the next circular electrode is 15 μm, and the gaps between other electrodes are 25 μm. The whole electrode pattern possesses a diameter of 6 mm, outside of which is ground.

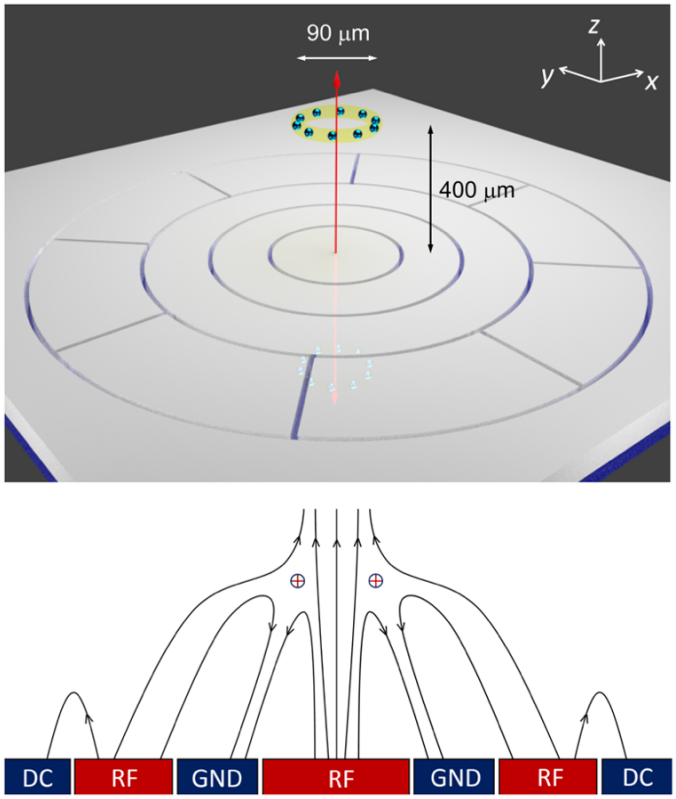

Figure 2.2.2 | The top figure shows the schematics our surface ring trap (not in scale). The bottom figure shows the cross-sectional electric fields at an instant when the RF voltage is positive to ground.

2.4 Fabrication of silicon surface trap with electrical vias

To preserve the circular symmetry, electrical connections need to be established beneath the trap surface. We develop a procedure to fabricate silicon ring trap with electrical vias through a glass substrate. The fabrication process flow is described in Fig. 2.3.1.

The trap is fabricated from boron-doped silicon anodically bonded on borofloat glass (SiO_2). The electrodes are patterned using photolithography followed by deep dry etching of silicon. The deep electrode trenches ensure that stray fields from bound charges in the glass are well shielded. Hydrofluoric acid (HF) etching of the glass underneath the trenches is performed to increase the distance between the electrodes through the glass surface and thus prevents surface flashover. Electrical vias are created on the backside by HF etching of the glass substrate with Au/Cr mask layers, followed by gold deposition and a liftoff process. The trap is glued onto the printed circuit board with epoxy. To secure their electrical connection, the

metal pads on the backside of the trap is Swiss crossed with gold wire bonds, which function as mechanical springs. Below we provide detailed descriptions for each step.

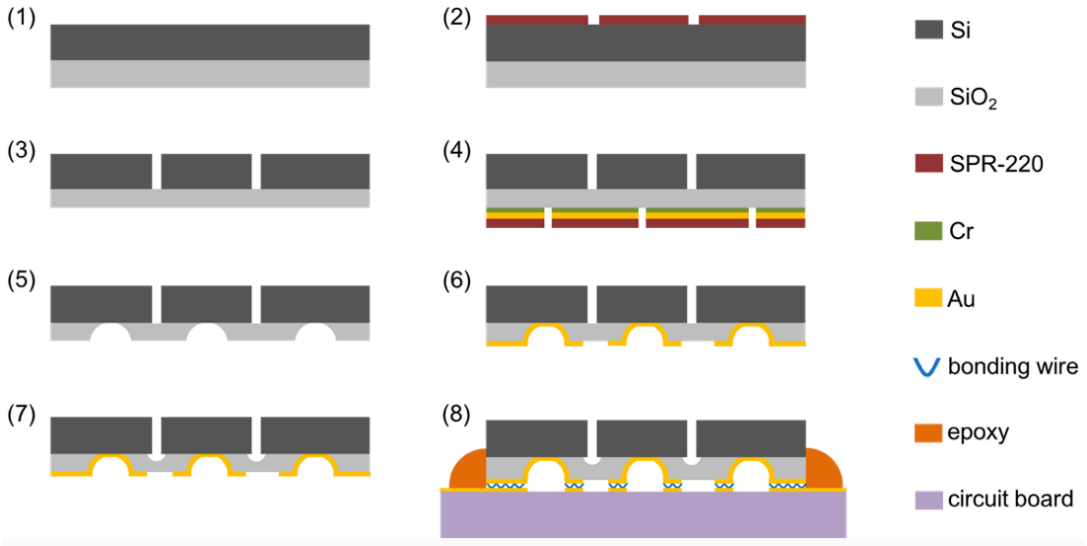

Figure 2.3.1 | Fabrication process of the silicon surface ring trap.

(1) The trap fabrication starts with anodic bonding of 4-inch silicon and borofloat glass wafers with thickness of 250 μm and 175 μm, respectively. The silicon wafer is highly Boron doped with resistivity <0.005 ohm·cm. Before the bonding, the wafers are cleaned in Piranha. Surface cleaning and cleanroom environment is crucial for the success of the bonding. Particles on the wafers will cause bubbles (Fig. 2.3.2) or even the failure of the bonding. The bonded wafers are diced into 12 × 12 mm^2 chips and cleaned again with Piranha.

Figure 2.3.2 | Glass wafer (top side) bonded to silicon wafer (bottom side). Wafer size is 4 inch. The white dots are the bubbles generated from the wafer bonding process.

(2) In order to pattern the top electrodes with photolithography, the chips are coated with SPR-220 photoresist with thickness of ~8 μm. Soft bake is performed at 115 °C for 6 min. To center the electrode pattern, we use the edges of the square-shaped chip for the alignment. The photoresist is exposed with a dose of ~360 mJ/cm^2 and developed in MF-26 A for 5 min. Hard bake is performed at 80 °C for ~100 mins. SPR-220 is viscous and sensitive to thermal shock and humidity change. It is important to prevent bubbles and any abrupt temperature change in the process. It will also be helpful to leave the sample at rest for ~30 mins between the exposure and the develop process.

(3) The deep silicon etching is performed in an Inductively Coupled Plasma (ICP) etch system. The Advanced Silicon Etch (ASE) process consists of alternating cycles of etching and protective polymer deposition to achieve high aspect ratios. To perform etching in the system, the chips are bonded to 6-inch handle wafers coated with thick SPR-220 photoresist. To enhance the thermal conduction to the chip, the photoresist is removed and cool grease is applied in the bonding areas of the handle wafers. After etching, the cool grease is gently removed with Acetone, and chips are cleaned with Isopropyl Alcohol and then Piranha. Optical images of the top electrode pattern after etching are shown below in Fig. 2.3.3.

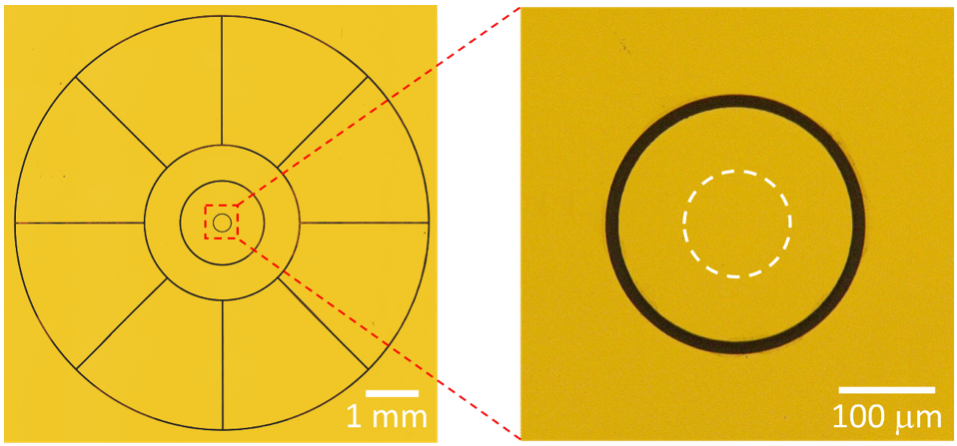

Figure 2.3.3 | Optical images of the top electrodes on the ring trap. The white dashed circle on the right figure shows the size of the ion ring.

(4) To open electric vias through the glass substrate, the glass side is thinned down in 49% hydrogen fluoride (HF) to ~70 μm, during which the topside of the chips are protected with melted wax. Afterwards, the chips are cleaned with hot Acetone and then Piranha. To form the HF etching mask, 60 nm Cr and then 200 nm Au are evaporated onto the backside. The second photolithography using SPR-220 is performed during which the via patterns are aligned to the top electrodes using the edge of the chips. After the hard bake, a short (~1 min) oxygen plasma descum process is performed to remove the photoresist residue. With melted wax protecting the top surface, the chips are dipped into Au and then Cr etchants and an HF etching mask is obtained.

(5) The vias are opened with 49% HF etching, as shown in Fig. 2.3.4. The size of the opening window heavily affects the etching rate. Afterwards, the wax and the metals on the chips are removed with hot Acetone and Au/Cr etchants. The chips are then cleaned thoroughly with Piranha.

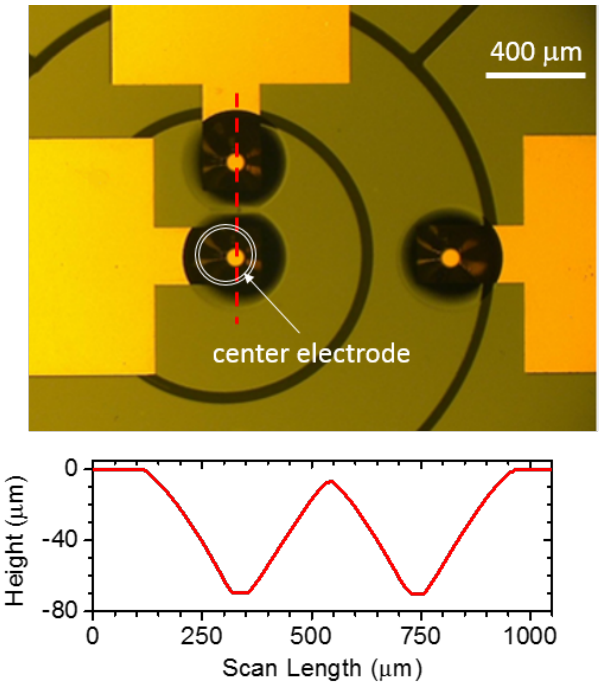

Figure 2.3.4 | Top: optical image of the backside of the ring trap. Bottom: surface profile scan along the dashed line in the top figure. The flatness at bottom of the scan confirms the through etching of the glass substrate.

(6) To pattern the electrical pads on the backside, a double layer photolithography process is performed with g-line & i-line photoresists (or with LOR-5A & i-line). After the develop process, a short (~1 min) oxygen plasma descum process is important to remove the resists residue. To remove the surface oxide on silicon and improve the electrical contact the chip is dipped into diluted HF (1:10) for ~10 s. Immediately after, the chip is placed in vacuum to evaporate ~10 nm Cr (for adhesion) and then ~800 nm Au. Metal liftoff process is then performed with a long soak in Acetone.

(7) To prevent surface flashover between the electrodes when high voltage is applied, HF etching of the glass from the topside is implemented to increase the distances between the electrodes through the glass surface. During the HF etching, the backside of the chip was protected with melted wax. A cross-sectional view of the trap is shown in Fig. 2.3.5. The deep silicon trench ensures that stray fields from bound charges in the glass are well shielded. Afterwards, the wax is removed with hot Acetone and the chip is cleaned with Piranha.

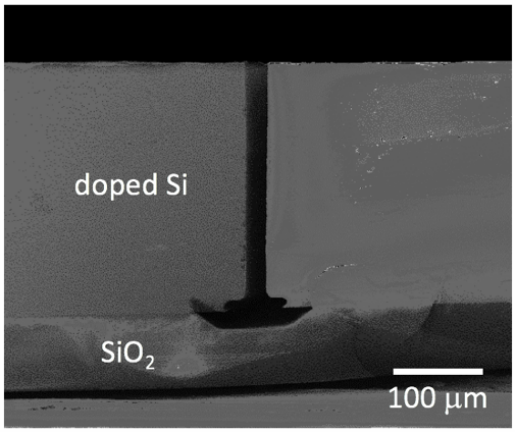

Figure 2.3.5 | Scanning electron microscope image of the trap cross section.

(8) To package the trap, the chip is gently pressed onto printed circuit board without touching the center electrode pattern and glued with epoxy. To secure the electrical bonding, all the electrodes are Swiss-crossed with gold wire bonds, as shown in Fig. 2.3.6. The wire bonds serve as elastic electrical connectors (fuss buttons) between the trap and the printed circuit board. This strategy eventually secures the electrical connections for all the 12 electrodes on the trap. Attempts of soldering the trap onto the circuit board have also been made but ended up with failure. The thin layer of electrical pads on the backside can be sucked into the solder paste during the heating.

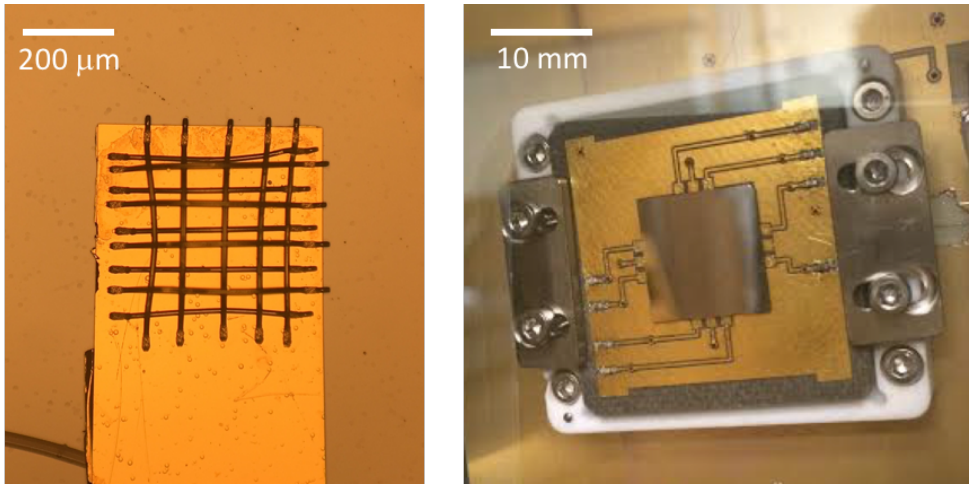

Figure 2.3.6 | Left: an electrical pad on the backside of the trap with Swiss crossed wire bonds, which act as a fuss button to secure the electrical bonding between the trap and the printed circuit board. Right: a silicon surface trap bonded on a printed circuit board.

2.5 Assembling the ring trap with ion trapping apparatus

The electrical connection between the trap electrodes and their corresponding pads on the printed circuit board needs to be checked thoroughly to secure the trap performance. This is achieved by probing the trap surface with an aluminum bonding wire. Since the smallest electrode on the trap is ~250 μm in diameter, the probe can be operated with hands under human eyes. After loading the trap, the chamber is pumped down and baked for weeks at ~160 °C to obtain the ultrahigh vacuum $<10^{-10}$ Torr, which is important for long ion lifetime (~hours). All electrical connection needs to be strong enough to survive the baking. Other necessary components for trapping include the atom oven (with ^{40}Ca source), ionization and cooling lasers (422 nm, 375 nm, 397 nm, 866 nm for $^{40}Ca^{+}$), a sensitive imaging setup, electric feedthroughs with RF and DC inputs, and an ion pump to keep the ultrahigh vacuum. An optical image of the assembled setup is shown below in Fig. 2.4.1. The experimental implementation of trapping and cooling is introduced in the following Chapter.

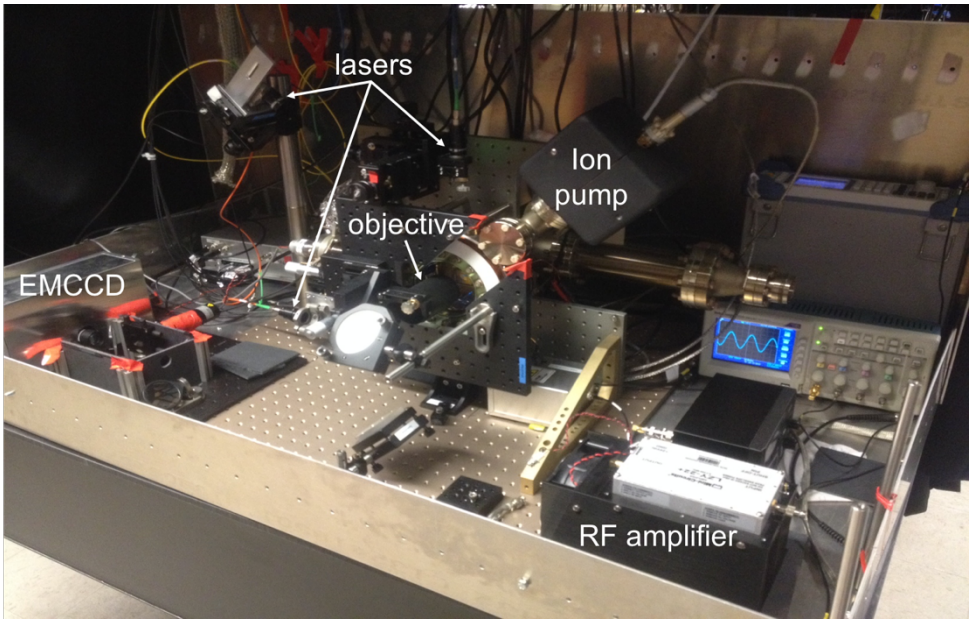

Figure 2.4.1 | Ion trapping experimental setup.

Chapter 3

Dynamics of microscopic ion rings at millikelvin

With the microfabricated surface trap discussed in Chapter 2, we are able to confine single $^{40}Ca^{+}$ ions into a microscopic ring and study the ion dynamics in this unique geometry. In this Chapter, we introduce our experimental characterization of the ion rings combined with the numerical analysis. In particular, we observe the transition from localized states to delocalized states by preserving the symmetry at laser cooling temperatures. We model the system and quantitatively explain our observation with numerical calculation.

The experimental data in this Chapter was taken with Erik Urban in Prof. Haeffner's lab [34].

3.1 Cooling and trapping of $^{40}Ca^{+}$ ions

In the experiment, we perform Doppler cooling to reduce the kinetic energy of the $^{40}Ca^{+}$ ions. We use a 397 nm light to excite the $S_{1/2}-P_{1/2}$ transition of the ion with a detuning Δ. In the red detuning case, the ion is more likely to absorb a photon when it is moving towards the laser than away from it, resulting in a net cooling effect. The process can be described semi-classically. Consider the ion is moving with a velocity v and each scattered photon transfers momentum $\hbar k$ onto the ion, the radiation pressure force is given by

$$F = \frac{s/2}{1 + s + [2(\Delta - kv)/\Gamma]^2}\hbar k\Gamma, \tag{3.1.1}$$

where s represents the saturation parameter and Γ denotes the transition linewidth. For small velocities, the force can be approximately written as a constant force plus a damping force proportional to the ion velocity. The damping force reduces the kinetic energy of the ion while the random nature of the scattering events provides a heating mechanism. The heating and the cooling processes are balanced at the equilibrium temperature called the Doppler limit, which can be expressed as

$$T_{min} = \frac{\hbar\Gamma}{4k_B}\sqrt{1+s}\,(1+\xi)\,, \tag{3.1.2}$$

where k_B is the Boltzmann constant and ξ is the geometric projection of an emission recoil kick onto the considered axis [18]. For dipole emission, ξ = 2/5.

To implement the trapping, we apply a 2π × 5.81 MHz signal with 220 V amplitude to the RF electrodes. A flux of neutral calcium atoms generated from a heated atom oven travels parallel to the trap surface. The neutral calcium is then ionized inside the trapping region through a two-photon process with laser beams at 422 nm and 375 nm. A red-detuned 397 nm laser beam then cools the ions through the $S_{1/2}$-$P_{1/2}$ transition. The $P_{1/2}$ state may decay into the $D_{3/2}$ state, bringing the cooling process to a halt. To counter this, the ions are re-pumped to the $P_{1/2}$ state with laser light near 866 nm [35]. The fluorescence of the ions at 397 nm is collected with a custom designed objective and imaged on an electron-multiplying charge-coupled device (EMCCD) camera (Fig. 3.1.1).

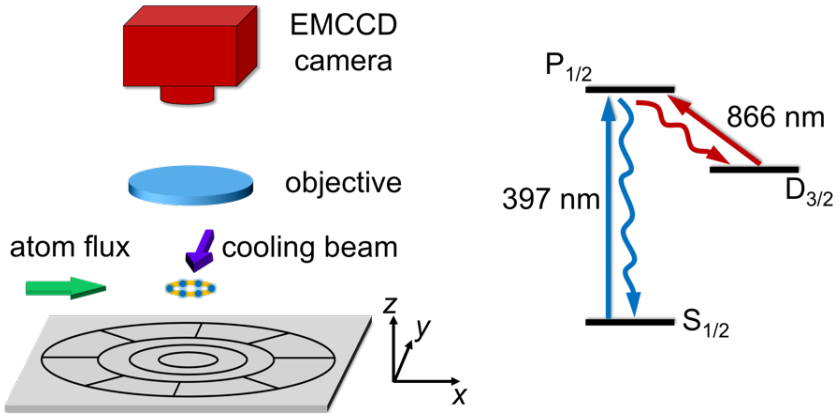

Figure 3.1.1 | Left: experimental schematics of cooling and trapping of atomic ion rings with the surface trap. Right: transitions involved in Doppler cooling of $^{40}Ca^{+}$ ions.

When captured by the RF trapping potential, the ions crystallize into a ring because of their mutual Coulomb repulsion, as shown in Fig. 3.1.2. With no compensating fields applied, the ions are typically pinned to one side of the ring by stray electric fields. The strength of the stray fields in the *x*-*y* plane is measured to be ~3 V/m by recording the compensating field required to reposition the ion crystal to be first symmetric to the *x*-axis and then to the *y*-axis. A local electric field due to a quadrupole moment of ~1 V/m is also present (expressed as the product of the quadrupole moment and ring radius). These stray fields are compensated by using the static voltage compensation electrodes before applying additional electric fields throughout the extent of this Chapter. The measured radial trapping frequency is 2π × 390 kHz. The trapping potential is able to hold up to 15 ions in a ring before the ion crystal forms a zigzag configuration when pinned.

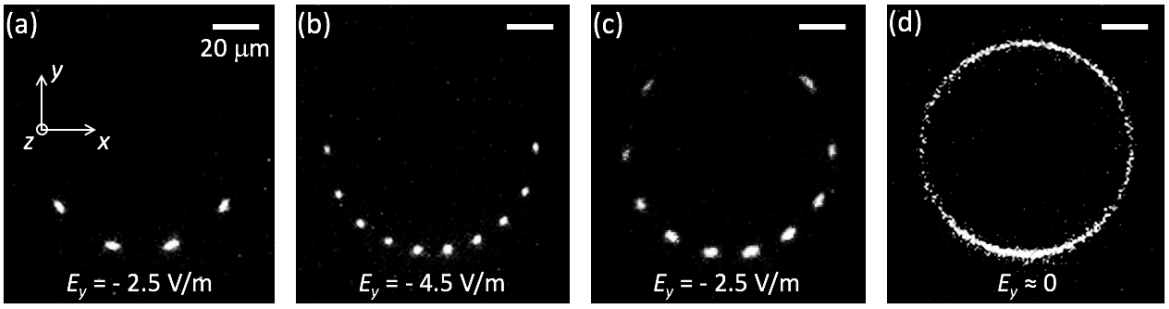

Figure 3.1.2 | (a)–(c) Images of ion crystals composed of four ions (a) and ten ions (b),(c) for different total dipole fields E_y. (d) Image of a delocalized ten-ion ring when the total external dipole field is close to zero. In (a)–(d), the scale bars are 20 μm. The fluorescence inhomogeneity of the images is caused by the size of the Gaussian cooling beam of ~70 μm full width at half maximum.

3.2 Gauging the symmetry of the ion rings

The presence of external electric fields in the trapping plane causes an asymmetry in the ring potential, leading to a finite tangential trapping frequency (common oscillation along the circumference of the ring). We gauge the asymmetry by measuring the tangential trapping frequency of the ion crystal. In the measurement, we apply a sinusoidal voltage to one compensation electrode and observe the excitation of the collective tangential mode with the EMCCD camera. Figures 3.2.1(b) and 3.2.1(c) present the observed dependence of the tangential trapping frequency on the total external dipole field E_y and the ion number N, respectively. As the ion number becomes larger, the increased Coulomb repulsion resulting from the reduced ion-ion spacing enforces a more uniform charge distribution in the ring, as shown in Figs. 3.1.2(a) and 3.1.2(c). For such a homogeneous charge distribution, an external electric field exerts a smaller restoring torque when the ion crystals deviate from the equilibrium position. Therefore, we expect the tangential trapping frequencies to decrease with an increasing ion number and better compensation of the stray fields.

The potential energy of the ion crystals can be modeled by considering only a homogeneous external field and the Coulomb repulsion of the ions confined to a ring. This results in a potential energy of the form

$$V = -\sum_i \frac{1}{2} e E_y d \cos\theta_i + \sum_{i<j} e^2 / \left(4\pi\varepsilon_0 d \sin\left|\frac{\theta_i - \theta_j}{2}\right|\right), \qquad (3.2.1)$$

where d denotes the ring diameter, θ_i describes the angular position of the ith ion, e represents the elementary charge, and ϵ_0 is the vacuum permittivity. We calculate the frequencies of the collective tangential motion by expanding the potential energy of the ion crystals to quadratic order in the ion displacements relative to equilibrium. The results are presented in Figs. 3.2.1(b) and 3.2.1(c). The calculation agrees well with the experimental results over the full extent of the measurement without free fitting parameters. This agreement confirms that homogeneous electric fields are the dominant symmetry-breaking mechanism in our experiment regime.

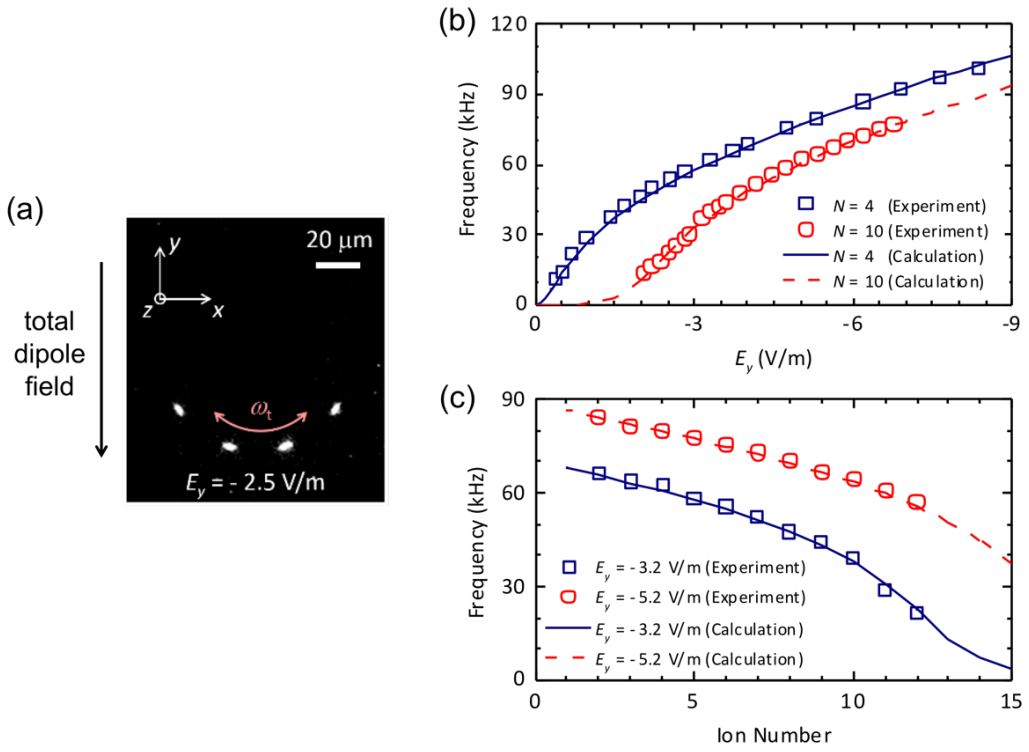

Figure 3.2.1 | (a) Illustration of tangential common mode oscillation of the ion ring under an electric field. (b), (c) Dependence of the tangential trapping frequency ω_t on the total external dipole field strength E_y (b) and ion number N (c), respectively. Error bars are smaller than the sizes of the data points. The curves correspond to the calculated collective tangential frequencies using the electric potential model considering only a homogeneous electric field and the Coulomb repulsion of the ions confined to a ring. The agreement between the calculated results and the experimental data confirms that the homogeneous electric fields are the dominant symmetry-breaking mechanism.

To further examine the effects of possible residual in-plane quadrupole, we add a quadrupole term to the potential energy given by Eq. (3.2.1). By comparing the calculated tangential trapping frequency and the experimental data, we found that the local electric field strength $Ad/2$ due to the residual quadrupole is smaller than 0.2 V/m.

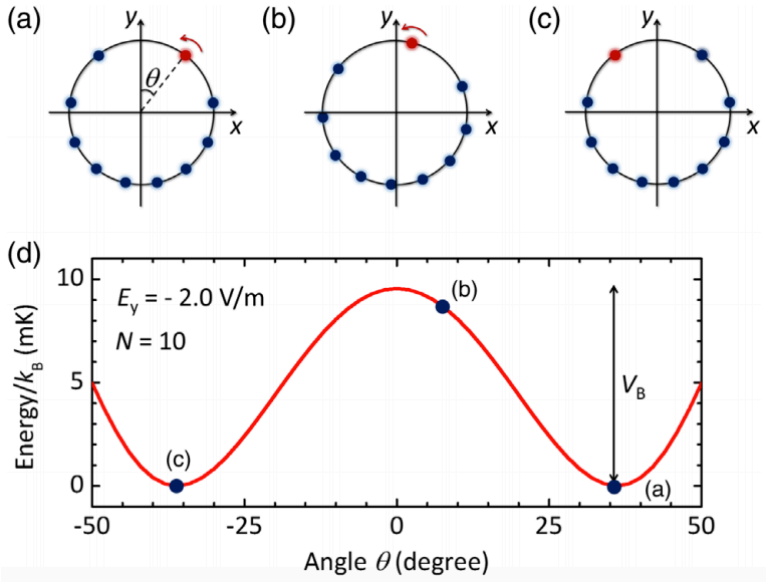

Figure 3.2.2 | The lowest potential energy configurations of a ten-ion crystal as a function of the position of the final ion (marked in red). The original equilibrium configuration is shown in (a). When the final ion moves from right to left, the nine other ions move into a new minimum configuration (b), and the crystal eventually recovers the original equilibrium configuration (c). (d) The calculated potential energy of ten ions as a function of the final ion position angle θ, where the difference between the minimum and the maximum is the rotational energy barrier V_B. The marked points correspond to the equilibrium configurations shown in (a)–(c), respectively. In this figure, $E_y = -2.0$ V/m.

In order to quantify the scale at which the symmetry is broken, we use the magnitude of the potential perturbations that localize the ion ring, defined as the rotational energy barrier. To obtain the rotational energy barrier, we numerically vary the position of the final ion in the chain and use the confirmed model presented in Eq. (3.2.1) to solve for the lowest potential energy configuration of the remaining ions, as described by Figs. 3.2.2(a)–3.2.2(c). The calculated potential energy of a ten-ion crystal versus the final ion position is plotted in Fig. 3.2.2(d). The two minimum energy locations correspond to the original equilibrium configuration of the crystal, and the peak energy represents the rotational energy barrier V_B. For ten ions, we observe localized ring crystals with in-plane electric fields larger than (2.0 $\pm$ 0.1) V/m. At this electric field, the rotational energy barrier is calculated to be $V_B/k_B = (10 \pm 4)$ mK, where k_B represents the Boltzmann constant.

Using similar method, we can also include the possible residual component in the calculation of the rotational energy barrier. The results for ten ion ring at small dipole fields is shown in Fig. 3.2.3. The dashed line indicates the tangential temperature of the ions determined by measuring the Doppler-broadening of the 729 nm $4^2S_{1/2}-3^2D_{5/2}$ transition. The calculated energy barrier can be several orders of magnitude lower than the temperature of the ions (~3 mK, dashed line). This number explains the delocalization of the ion rings shown in Fig.

3.1.2(d), where the kinetic energies of the ions are much larger than the confining energy barrier and thus the ions no longer have a constant angular position.

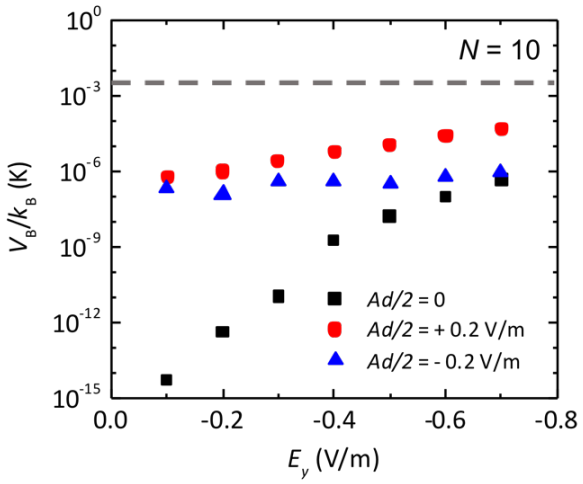

Figure 3.2.3 | Dependence of the calculated rotational energy barrier on the total external dipole field strength E_y for 10 ions at the presence of different in-plane quadrupole fields.

3.3 Transition from localized states to delocalized states

As we decrease the dipole electric field, the symmetry of the ring is restored and the ions start to become delocalize. For a ten-ion crystal, delocalization occurs at $E_y = -(1.9 \pm 0.1)$ V/m, corresponding to a rotational energy barrier of $V_B/k_B = (6 \pm 3)$ mK. When more ions are held in the trap, the field strength at which the ring delocalizes increases, as shown in Fig. 3.3.1(a). This trend is due to the fact that increased Coulomb repulsion from more ions increases the force necessary to deform the ring.

The delocalization point is sensitive to the position of the cooling beam. The radiation pressure from an unbalanced cooling beam exerts a net torque on the ring, leading to a delocalization at larger fields. For this reason, the cooling laser is positioned to the point at which the transition occurs at the smallest field. Numerical analysis of radiation pressure induced ion rotation is described in section 3.4.

Although the electric field strength at which the ring delocalizes increases with an increased ion number, we find that the corresponding rotational energy barrier is independent of the ion number, as shown in Fig. 3.3.1(b). The proximity of the tangential ion temperature to the transition energy barrier V_B/k_B suggests that delocalization occurs when the thermal energy of the ions is large enough to overcome the rotational energy barrier.

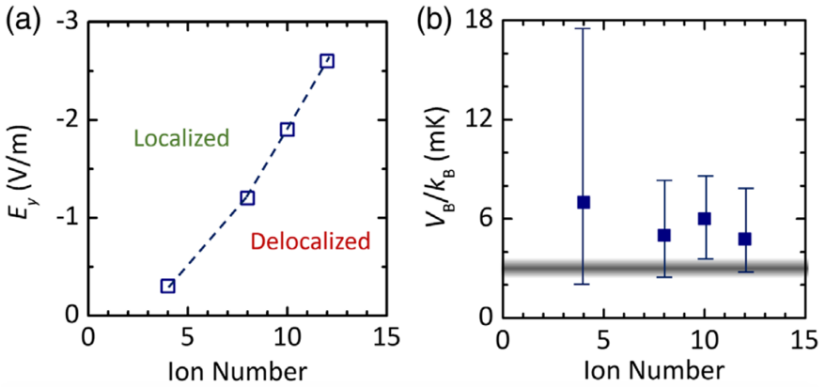

Figure 3.3.1 | Total external electric field strength (a) and corresponding rotational energy barrier V_B/k_B (b) at which the ion crystals are observed to delocalize as a function of the ion number. The errors of the electric fields in (a) are 0.1 V/m. The gray line in (b) denotes the measured tangential temperature ~3 mK of the ions.

3.4 Molecular dynamics simulation of ion rings

In this section, we provide the molecular dynamics simulation of the delocalization process of the ion ring by including the stochastic effect of the temperature using the Langevin equation

$$m\frac{d}{2}\ddot{\theta}_i = -\lambda\frac{d}{2}\dot{\theta}_i + \eta_i(t) - eE_y\sin\theta_i + \sum_{j\neq i}\frac{e^2\cos\left[\left(\theta_i-\theta_j\right)/2\right]}{4\pi\epsilon_0\left\{d\sin\left[\left(\theta_i-\theta_j\right)/2\right]\right\}^2}, \quad (3.4.1)$$

where $\left(\theta_i-\theta_j\right)\in(0,2\pi)$ and m is the mass of $^{40}Ca^+$ ions. The fluctuating forces η_i are related to the tangential ion temperature T_t and the effective laser damping $\lambda\sim\hbar(2\pi/397\,nm)^2$ by $\langle\delta\eta_i(t)\delta\eta_j(t')\rangle = 2\lambda k_B T_t\delta_{ij}\delta(t-t')$. We simulate the fluctuating forces with random number generators in Matlab and obtain the angular distribution $p(\theta)$ of the ions (normalized such that $\int_0^{2\pi}p(\theta)d\theta = N$).

In Fig. 3.4.1, we compare the numerical simulation results with the experimentally observed ion fluorescence distribution near the localization-delocalization transition points. The qualitative agreement between the numerical results and the experimental data suggests that the delocalization can be well described by thermal effects when we balance the radiation pressure of the cooling laser.

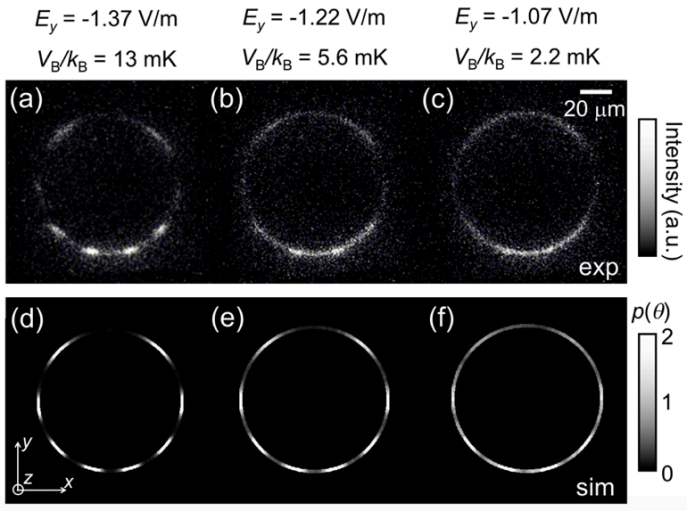

Figure 3.4.1 | (a)–(c) Image of eight-ion rings in the localization-delocalization transition regime. (d)–(f) Corresponding simulated angular distribution $p(\theta)$ of the ions using the Langevin equation with $T_t = 3$ mK. Reduced fluorescence on the extrema of the x axis is due to the Gaussian profile of the detection beam incident from the positive y direction.

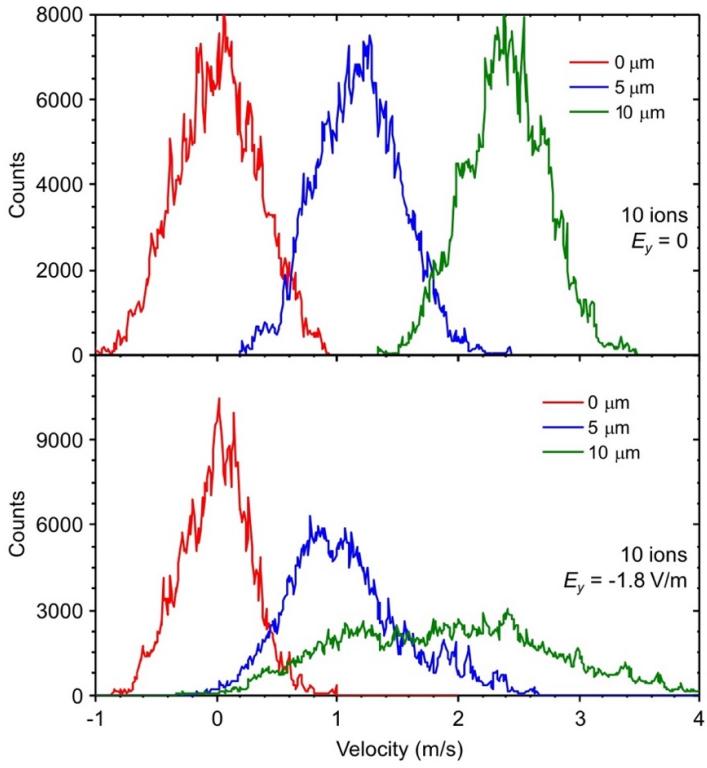

Figure 3.4.2 | Simulated velocity distributions of the ions with different laser displacements from the ring center. The y-axis describes how often a specific velocity is found. The electric dipole fields in the y direction are 0 and -1.8 V/m in the upper and lower figure.

The ion dynamics under the cooling beam can be further studied numerically by considering the quantum jump process. Basically, the ions absorb the photons come from the laser beam and emits photons randomly and abruptly to all directions. The momentum transfer between photons and ions significantly affects the dynamics of the ion ring. When the laser beam is shifted from the center of the ring, the imbalanced radiation pressure push the ions to rotate. As the ion velocities reach certain values, the Doppler effects will change the absorption of the ions and thus balance intensity distribution of the laser beam. As a result, the ion ring will reach a steady rotation state with a nonzero averaged velocity. The velocity distributions for a ten-ion ring at the steady state are shown in Fig. 3.4.2. The presence of a dipole field will broaden the velocity distribution as it can accelerate or deaccelerate the ions when they are rotating. In the simulation, we use realistic parameters that are close to our experimental conditions. The Gaussian laser beam has a width of ~70 μm and the saturation factor at the beam center is 0.3.

3.5 Conclusion and outlook

In conclusion, we have implemented a novel surface trap design and confined rings of $^{40}Ca^{+}$ ions. Unavoidable symmetry-breaking stray electric fields can be nearly compensated with homogeneous fields to provide a high degree of circular symmetry. The circular symmetry of the ion ring is preserved at millikelvin temperatures and can be potentially maintained much further. Approaching smaller energy scales, we expect that higher order multipole fields will become relevant to the circular symmetry, as shown in Fig. 3.2.3. To explore these effects, further cooling of the rotational degree of freedom is required.

Our system opens up a new regime to experimentally explore many-body quantum physics with translational invariance where individual particles can be accessed and controlled. The symmetry and periodicity of the ion ring provide a unique platform in which to explore quantum computing and quantum simulation.

In the classical regime, the control and probe of ion rings may shed light on the puzzled ion transport process in one/two dimensional channels [36,37], where the Coulomb repulsion and ion correlations play a significant role under the strong confinement. Understanding the complex ion transport process at nanoscale is important for cell biology, clean energy and water purification.

Remark: Chapter 2 and Chapter 3 include published materials from H.-K. Li*, E. Urban*, et al. “Realization of translational symmetry in trapped cold ion rings.” *Phys. Rev. Lett.* 118, 053001 (2017). (*contributed equally).

Chapter 4

Valley-mechanical coupling in monolayer semiconductors

4.1 Background and motivation

In addition to charge and spin, electrons travelling in periodic lattice of some solids possess an extra degree-of-freedom called "valley", which specifies which states the electrons occupy among the degenerate energy extrema in the band structure. Different from the conventional electronics and spintronics, valleytronics encodes information to the "valleys" and holds great potential to the developments of communication and computation [38,39]. Over the past decade, significant progresses have been made in controlling and probing the valley dynamics, especially in two dimensional van der Waals monolayer semiconductors [8,9,40].

To date, explorations of valleytronics have focused on optoelectronic and magnetic means [41-48]. Incorporating mechanical degree-of-freedom would stimulate both fundamental studies of valley and mechanical properties of solids and new applications of valleytronics, as evidenced by the huge success of micro/nano electromechanics [5-7]. Mechanical systems are intrinsically immune to electromagnetic interference. Their functionalities as switches, filters, and oscillators are ubiquitous in daily used devices [49], such as cellphones. They are also renowned for their versatility to interact with various physical environments while maintaining low dissipation. Excellent mechanical sensors and transducers have been demonstrated in both classical and quantum scenarios [50-53]. The latter plays an important role in fundamental studies of macroscopic quantum phenomena, such as the Schrödinger cat paradox.

In this Chapter, we introduce a scheme to couple electron valley and mechanical motion in two dimensional semiconductors. With this scheme, we are able to directly transduce valley excitation into macroscopic mechanical motions of the materials [10]. The experimental realization using monolayer MoS_2 is described in the following chapter. Our study lays the foundation for a new class of valley-controlled mechanical devices and facilitates realization of hybrid valley-mechanical systems.

4.2 Electron valley in monolayer transition metal dichalcogenides

Monolayer transition metal dichalcogenides have recently emerged as important materials for valleytronics and optoelectronics applications. The structure of the materials is shown in Fig. 4.1.1. In a monolayer MX_2, a single layer of transition metal atoms (M = Mo, W) is sandwiched by two layers of chalcogen atoms (X = S, Se). The semiconducting materials have direct band gaps in the infrared-visible range. Their honeycomb lattice supports two valleys in momentum space (namely K and K') and thus forms a spin-like binary system called valley-pseudospin. Because of the broken inversion symmetry and the strong spin-orbit coupling, the materials hold intriguing valley properties [39]. First, the two valleys K and K' can be selectively excited by circularly-polarized light with helicity σ^+ and σ^-, respectively. This unique selection rule provides a powerful tool for optical generation and manipulation of the valleys [41,42]. Second, the Berry curvature (effective magnetic field in momentum space) can significantly modify the electron dynamics and generate appealing electrical transport phenomena such as the valley Hall effect, which allows us to probe valley polarization with electrical method [43]. Third, due to the time reversal symmetry, electrons in the two valleys possess magnetic moments that are same in magnitude while opposite in sign. This property enables the valley Zeeman effect and therefore allows us to lift the valley degeneracy with out-of-plane magnetic fields [45,46]. With these properties, the research on valleytronics on two dimensional semiconductors has grown rapidly over the past several years.

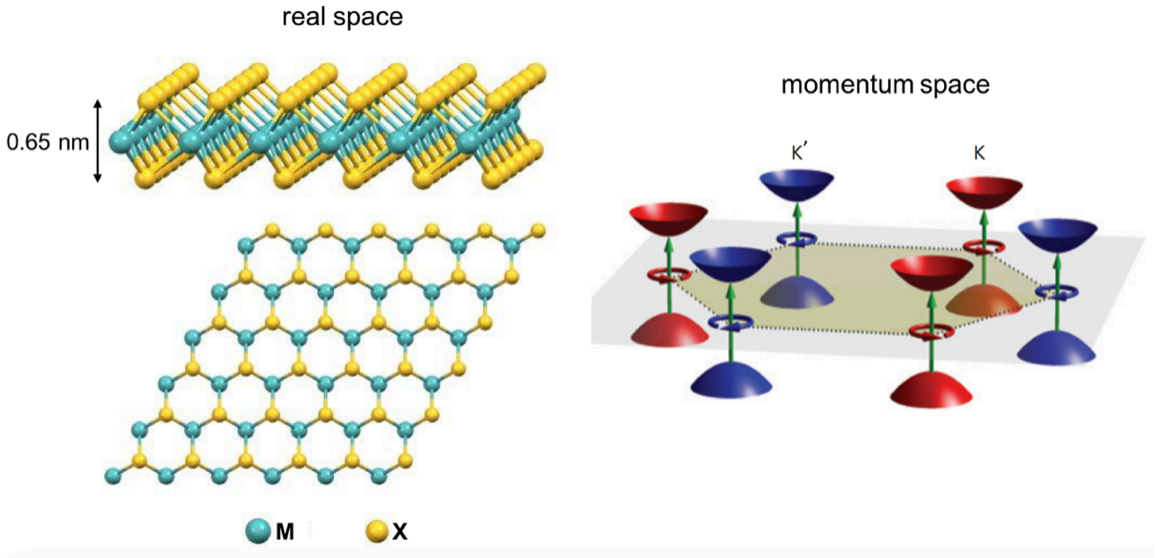

Figure 4.1.1 | Left: structure of monolayer transition metal dichalcogenides. Right: electronic band structure of the materials which consists of two valleys K and K'. The figure is adopted from Ref. [8].

4.3 Valley-mechanical coupling under a magnetic field gradient

In addition to the intriguing valley properties, nanomechanical devices [54-56] made of two dimensional crystals exhibit high mechanical strength [57], high quality-factors [58], and extraordinary force and mass sensitivities [59]. Their extremely small masses also give rise to large quantum zero-point motions which are desirable for the study of quantum dynamics. These facts motivate us to explore valley-mechanical interaction in monolayer van der Waals semiconductors.

Our concept is presented in Fig. 4.2.1. Because of the broken inversion symmetry, electrons at K and K' valleys possess opposite Berry curvatures and undergo clockwise and counter-clockwise hopping motions, which result in out-of-plane valley magnetic moments. This orbital magnetic moment is locked to the magnetic moments from the electron spin and the parent atomic orbitals. As a result, the total magnetic moments carried by electrons at the two valleys are equal in magnitude while opposite in sign.

In the presence of a perpendicular magnetic field gradient, the material encounters a net force which is proportional to the field gradient and the net valley population. Direction of the force is determined by which valley is populated and therefore it enables the transduction of the valley excitation (K or K') to the mechanical displacement (upward or downward), as described below in Fig. 4.2.1. In this scenario, the valley-mechanical interaction strength can be effectively controlled with the magnetic field gradient.

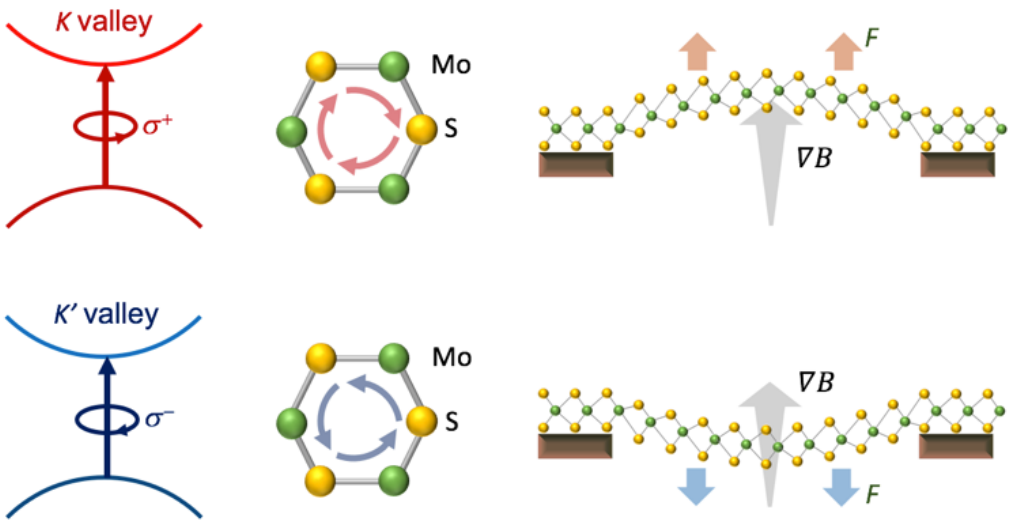

Figure 4.2.1 | Valley-mechanical coupling under an out-of-plane magnetic field gradient.

4.4 Experimental design

The schematics of our experimental design is shown in Fig. 4.3.1. It consists of a monolayer MoS_2 suspended over square hole structures conformally coated with Ni/Fe permalloy films. On top of the permalloy, a thin film of gold (30 nm) is placed to enhance the surface adhesion to monolayers and the optical reflectivity. The lateral dimension of the square hole is 5.2 × 5.2 μm^2. Under an applied magnetic field perpendicular to the substrate, the permalloy structure distort the local field and induces a field gradient. The color-scale represents the magnitude of z-component of the magnetic field B_z simulated by a finite element method. With a magnetic field of 26 mT, the field gradient in the central area of the suspended MoS_2 reaches ~4000 T/m. In the simulation, we use the permeability of the permalloy thin film calibrated by a superconducting quantum interference device. The relative permeability is $\mu_\perp \approx 2.2$ in the out-of-plane direction (hard axis) and $\mu_\parallel \approx 72.2$ in the in-plane direction. The thickness of the permalloy is ~150 nm on the side walls and ~600 nm on the planar surface. At such thicknesses, the field gradient is mostly determined by the geometric size of the hole structure and the applied magnetic field.

The monolayer is normally incident by a pump laser beam at 633 nm whose polarizations are modulated between LCP and RCP. The pump polarization controls the valley population through the optical selection rule mentioned above. The mechanical displacement is detected by a linearly polarized probe laser (654 nm) through the interference between the lights reflected from the monolayer MoS_2 and the bottom gold surface. The MoS_2-gold distance is designed to be 1.83 μm, which enables high displacement sensitivity and high magnetic field gradient.

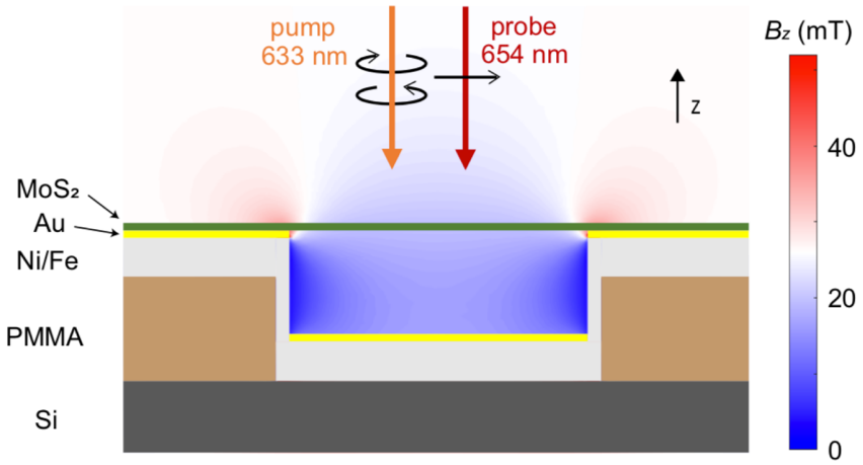

Figure 4.3.1 | Experimental design to realize valley-mechanical transduction.

4.5 Basic analysis of valley-mechanical interaction

For a membrane under tensile-stress occupying the region $-\frac{L}{2} < x < \frac{L}{2}$ and $-\frac{L}{2} < y < \frac{L}{2}$, the displacement of the fundamental mechanical mode can be expressed as

$$z_0(x, y, \omega) = z[\omega]\psi(x, y) \tag{4.4.1}$$

where $\psi(x, y) = \cos\left(\frac{\pi x}{L}\right)\cos\left(\frac{\pi y}{L}\right)$ is the mode profile and $z[\omega]$ is the displacement at the center of the resonator. Under a driving force $F[\omega]$, the displacement follows

$$z[\omega] = \chi[\omega]F[\omega] \tag{4.4.2}$$

where $\chi[\omega] = 1/m_{eff}(\omega^2 - \Omega_m^2 + i\omega\Omega_m/Q)$ is the mechanical susceptibility, $\Omega_m/2\pi$ is the resonance frequency, and Q is the mechanical quality factor. The effective mass m_{eff} is 1/4 of the mass of the suspended MoS_2, and it is calculated to be 21 fg using the density of the material. Consider the distribution of the magnetic field gradient $\nabla B(x, y)$ and the carrier densities n_K and $n_{K'}$ in the plane of the monolayer, the total valley-mechanical force can be expressed as

$$F_{valley}[\omega] = \int_{-\frac{L}{2}}^{\frac{L}{2}} dx \int_{-\frac{L}{2}}^{\frac{L}{2}} dy\, \psi(x, y)[n_K(x, y, \omega) - n_{K'}(x, y, \omega)]\mathrm{g}\mu_B\nabla B(x, y) \tag{4.4.3}$$

Here, g represents the Lande g-factor and μ_B denotes the Bohr magneton. At low pumping power, the valley carrier densities are proportional to the pump intensity, which can be described by a Gaussian function $\exp(-2(x^2 + y^2)/w_1^2)$ with w_1 being the width of the pump beam. In our implementation, the valley carriers mainly distribute in the central area of the suspended material since the pump beam width $w_1 \sim 1$ μm is much smaller than the resonator lateral size (5.2 μm). The magnetic field gradient is also relatively uniform in the pump area as verified by our numerical simulation. Under such conditions, the valley mechanical force can be approximated as

$$F[\omega] \approx (N_K[\omega] - N_{K'}[\omega])\mu_B\mathrm{g}\nabla B(0,0) \tag{4.4.4}$$

where N_K and $N_{K'}$ are the numbers of carriers at the K and K' valleys, respectively. The single-phonon valley-mechanical coupling rate is given by

$$g_0 = \mathrm{g}\mu_B\nabla B x_{zpf}/\hbar, \tag{4.4.5}$$

which describes the valley energy shift induced by the quantum zero-point motion of the resonator $x_{zpf} = \sqrt{\hbar/4\pi f_m m_{eff}}$, where f_m stands for the mechanical resonance frequency.

Chapter 5

Realization of valley-mechanical transduction

Utilizing the experimental scheme discussed in Chapter 4, we are able to realize valley-mechanical coupling and demonstrate the direct transduction of valley excitation into nano-mechanical states. In this Chapter, we discuss about our experiment methods, including sample fabrication, material characterizations, measurement setup, signal acquisition, and data analysis. We observe unambiguous valley-actuated mechanical motion and present effective control of valley-mechanical force using various external conditions, including pump light, magnetic field gradient, and temperature.

5.1 Fabrication of valley-resonators

In this section, we present the fabrication process for making the valley-resonators. Two methods for suspending two dimensional semiconductors are presented here: the dry transfer method and the critical point dry method. Our final experimental design is accomplished by the dry transfer method.

5.1.1 Dry transfer method

Fabrication process of the valley-mechanics device using dry transfer method is illustrated in Fig. 5.1.1. We first spin-coat poly-methyl-methacrylate (PMMA) on a silicon substrate. The thickness of the PMMA is calibrated with both thin film optical interferometry and scanning profilometry. The PMMA is patterned with square hole structures using electron beam lithography. After the develop process, PMMA is reflowed on hotplate at 135 °C for 5 min to smoothen the sharp edges at the top of the square holes. To generate the local magnetic field gradient on the device, we deposit a permalloy thin film (Ni/Fe, Kurt J. Lesker Company, part #: EJTPERM253A2) using magnetron sputtering. The sample is tilted by ~45° during the deposition to ensure that all the sidewalls are well covered. On top of the permalloy, a thin film of gold (30 nm) was deposited by electron-beam evaporation to

enhance the surface adhesion to monolayers and the optical reflectivity. Finally, monolayer MoS_2 is exfoliated onto Polydimethylsiloxane (PDMS) (Gel-Pak, X4) and then transferred onto the patterned substrate with the dry transfer method developed in Ref. [60].

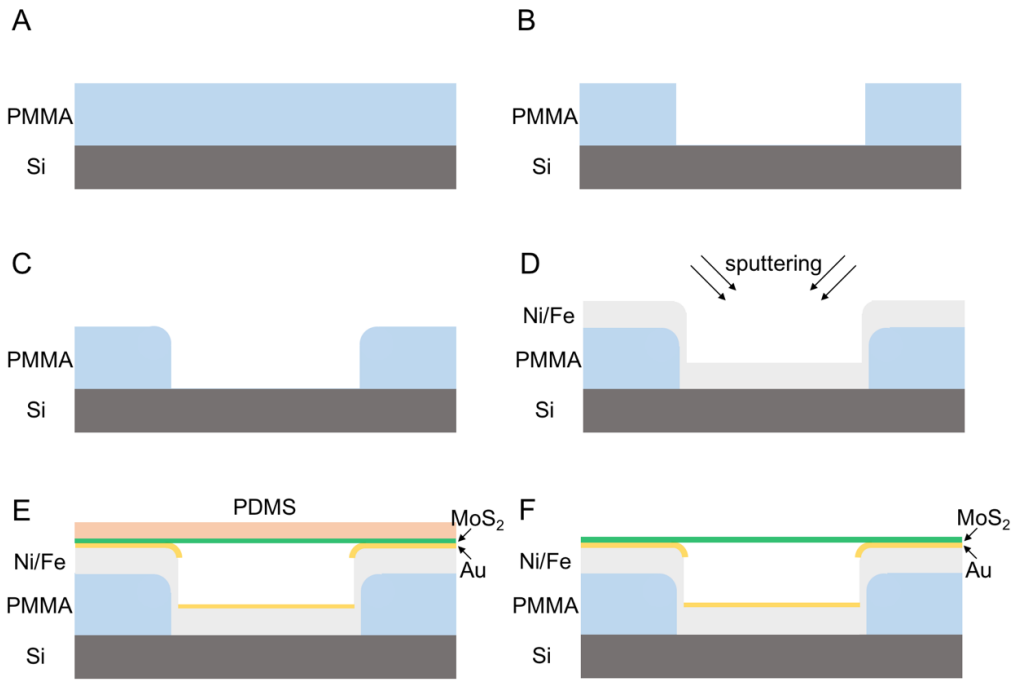

Figure 5.1.1 | Fabrication process flow of monolayer valley-resonator using the dry transfer method.

The monolayer material can be very fragile during the dry transfer process, especially at the empty hole region where the material has no mechanical support beneath. The successfulness of the transfer process heavily relies on reducing the stretch of the material. To lower the chance of breakage, it is very important to align the material parallel to the substrate and reduce the PMMA pickup speed. The parallelism can be identified by the moving speed of the touching boundary under optical microscope by keeping the same pickup speed. For a single hole, the PMMA pickup usually last for 30 to 60 minutes. Another strategy we use is to pattern square holes instead of circular holes. The abrupt change of tension is prevented by starting the pickup from one corner of the square. Finally, heating up the substrate by ~20 degrees after placing on the MoS_2&PMMA can soften the PMMA, and therefore reduce the tension and increase the success rate. The final success rate we obtain is ~20%. An optical image showing the dry transfer process is shown below in Fig. 5.1.2.

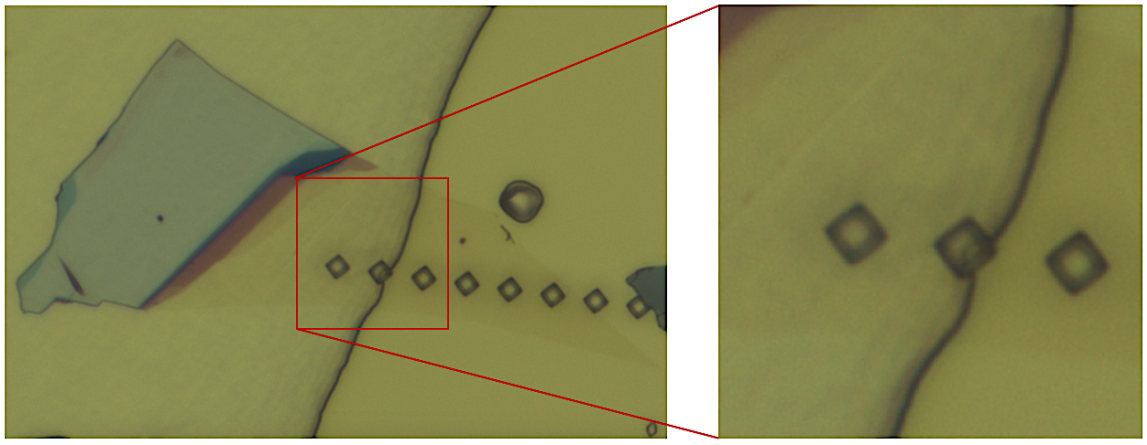

Figure 5.1.2 | Optical image of the sample during the dry transfer process. The PDMS is peeled off from the substrate from the left side to the right side. The black curve shows the peeling off boundary.

An optical image of the device for our final measurement is shown in Fig. 5.1.3. The three holes on the upper right of the optical image are covered with monolayer MoS_2. A slight optical contrast between the three holes and the hole on the lower left is present due to the optical absorption of the material. The photoluminescence emission from the suspended regions is much stronger than that from the metal substrate and thus verifies that the membrane is freestanding, as shown by the inset.

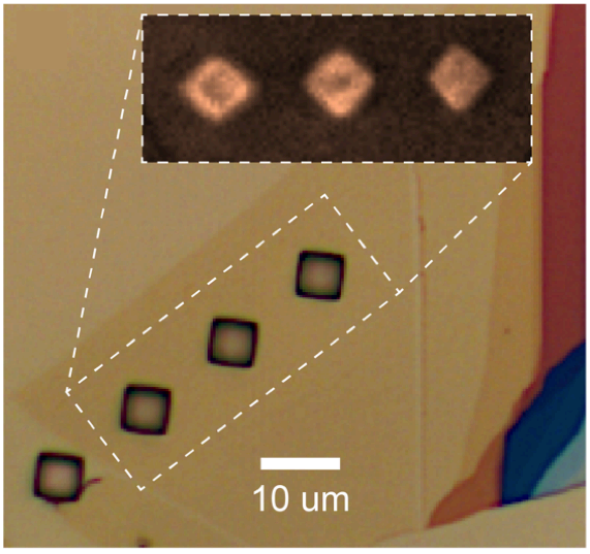

Figure 5.1.3 | Optical image of the final device. The inset shows the photoluminescence emission from the material.

5.1.2 Critical point dry method

At the early stage of the project, we have also used a critical point dry method [61] to suspend two dimensional semiconductors and then test their mechanical properties. The fabrication process flow is presented in Fig. 5.1.4. MoS_2 flakes are first exfoliated onto stackings of PMMA/aquaSave/PMMA. The MoS_2 is then pressed onto a chip coated with HSQ (FOX-15). The two chips are immersed into deionized water which removes the aquaSave and leaves a PMMA layer on top of the MoS_2. Afterwards, the PMMA is patterned with electron beam lithography (EBL). After the development process, the chips are evaporated with 10 nm Cr and 90 nm Au. The samples are then lifted off in acetone, transferred to aquatic KOH/NaCl solution (40 g water, 0.56 g KOH, and 0.58 g NaCl) for the development of HSQ. Finally, the samples are immersed into IPA and released with critical point drying.

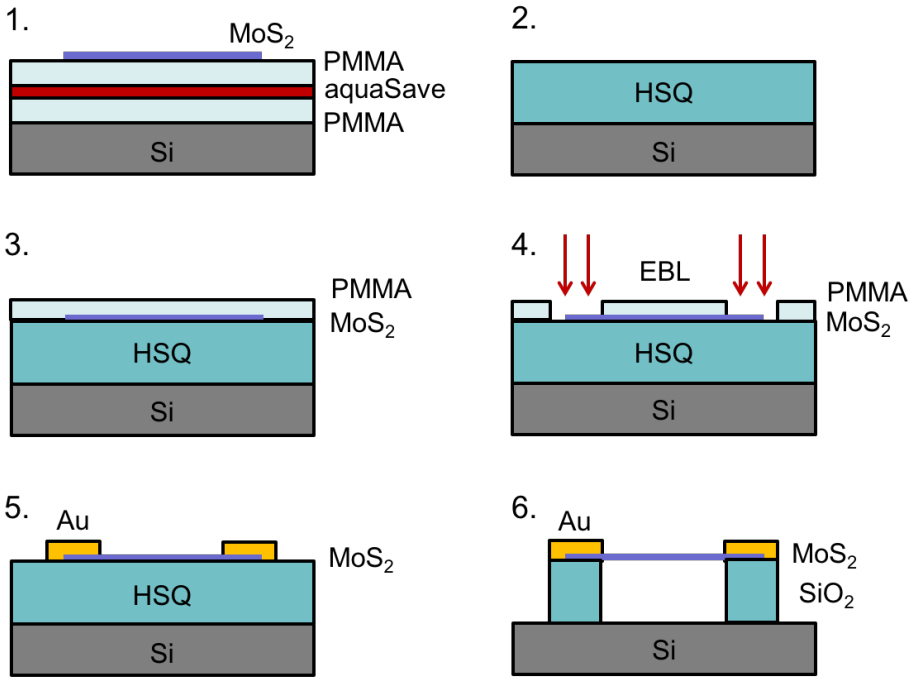

Figure 5.1.4 | Fabrication process flow of monolayer resonator with the critical point dry method.

A scanning electron microscope (SEM) image of a suspended MoS_2 flake is shown in Fig, 5.1.5. This process allows us to electrically access the suspended materials from the sides. However, it is not compatible with the patterning of permalloy film structures, which are required to generate strong magnetic field gradient. Hence, we did not proceed this method for the final measurement.

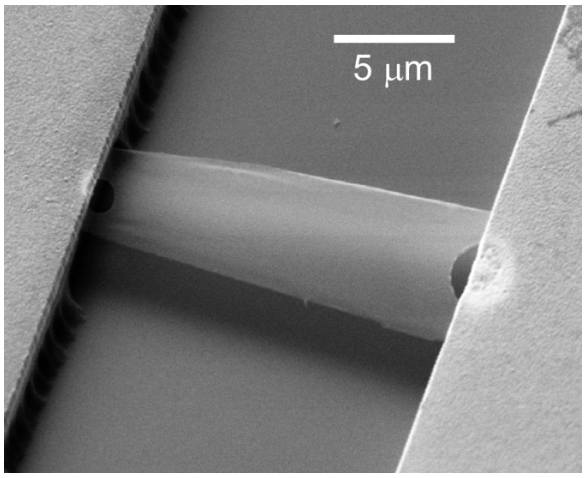

Figure 5.1.5 | SEM image of a suspended MoS_2 fabricated with the critical point dry method. The two sides of the sample are cut with focus ion beam (FIB) to reduce the resonance frequency.

5.2 Material characterizations

We characterize the suspended MoS_2 membrane using photoluminescence and Raman spectroscopy. The results for the sample we use in the final measurement (Fig. 5.1.2) are shown in Fig. 5.2.1. The photoluminescence emission from the suspended region is over 10 times stronger than that from the supported region. As a result of the tensile stress, the photoluminescence peak is slightly red shifted at the suspended region. The Raman peaks of phonon modes A1g and E2g are separated by 19.9 cm^{-1}. These features are in good agreement with previous studies of monolayer MoS_2 and verifies the monolayer nature of our valley-resonator.

On a separate device, the electrical properties of a trilayer MoS_2 exfoliated from the same crystal source is characterized by a field-effect transport measurement, as shown in Fig. 5.2.2. A field-effect transistor (FET) is fabricated on the MoS_2 flake supported on SiO_2 using few layer graphene for ohmic electrical contacts. A transfer curve measured at 20 K shows that the device has a turn-on voltage of 60 V. Such a high turn-on voltage reveals the intrinsic nature of our MoS_2 crystal source.

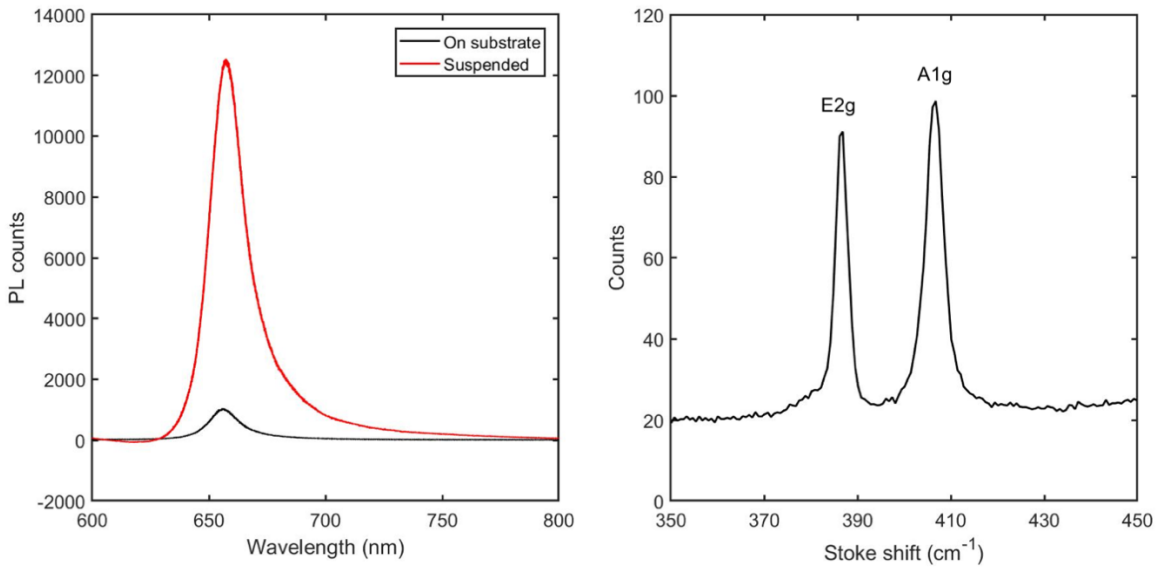

Figure 5.2.1 | Left: Photoluminescence spectrum of the monolayer MoS_2. Right: Raman spectrum measured at the suspended MoS_2 monolayer.

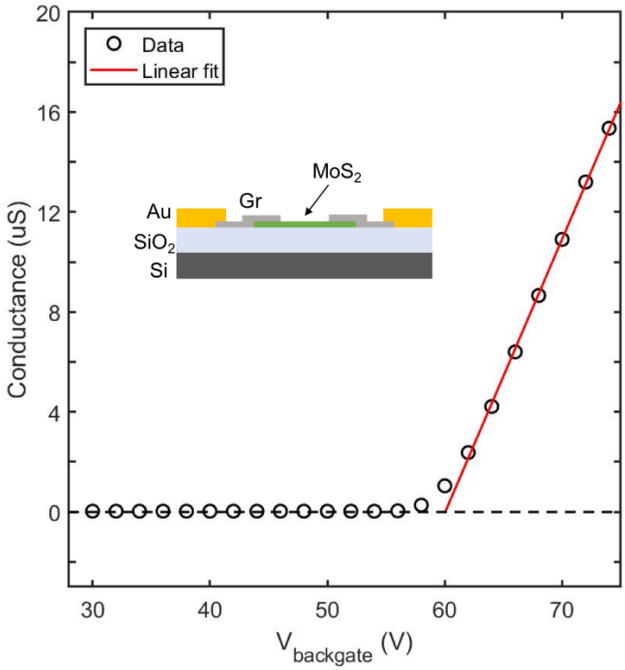

Figure 5.2.2 | Electrical transport curve measured with a separate trilayer MoS_2 FET device made from the same crystal source.

Sample substrate temperature calibration is performed by mounting a temperature sensor directly onto the sample stage. As shown on the left of Fig. 5.2.3, the temperature of the sample stage deviates significantly from the cryostat (Janis ST-500) inner temperature mainly due to thermal radiation entered from the optical viewport. The lowest sample stage temperature we attain in the experiment is 20 K.The optical absorption of the suspended monolayer MoS_2 is measured to be 3.4% at 633 nm (pump) and 4.8% at 654 nm (probe), which is enhanced by the optical interference effect. We estimate the optical absorption heating using finite element simulation. Experimental and theoretical values of the thermal conductivity of monolayer MoS_2 range from ~20 W/mK to ~50 W/mK [62-64]. With laser spot sizes of ~1 μm, central region of the monolayer is estimated to be heated up by 5 to 15 K relative to the surrounding substrate under laser powers of 11 μW for the pump and 4 μW for the probe, as shown on right of Fig. 5.2.3.

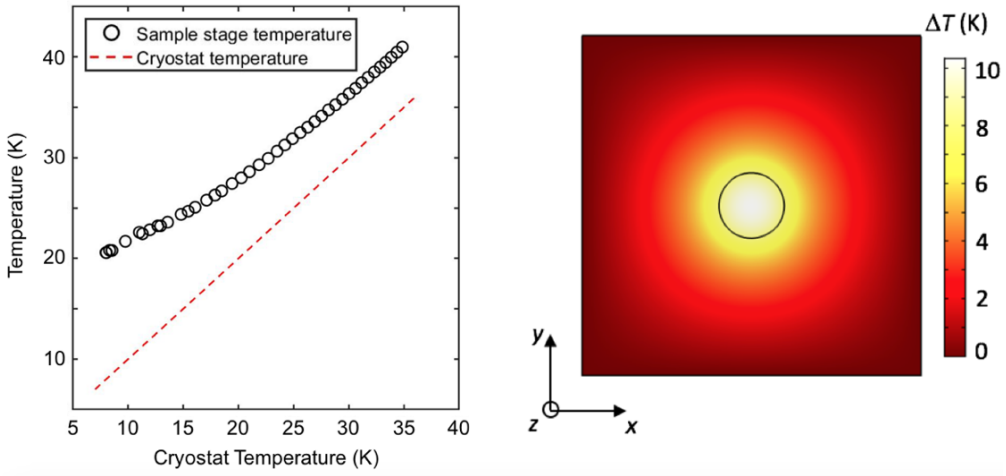

Figure 5.2.3 | Left: Calibration of the sample substrate temperature in the cryostat. Right: Simulation of local temperature distribution of the monolayer MoS_2 under laser heating. The circle indicates the laser spot (~1 μm). Here, the thermal conductivity of MoS_2 is 30 W/mK.

Mechanical response of the device is characterized under vacuum (~10^{-6} Torr) in cryostat. Before lowering the temperature to cryogenic level, the chamber was pumped for 2 days to fully evacuate the residual air trapped under the monolayer. We characterize the mechanical resonance by modulating the intensity of the pump light, which thermo-optically drives the monolayer resonator. The driving signal increases when the laser spots move towards the center of the suspended region, which confirms that the mechanical mode we probe is the fundamental mode. Mechanical spectra measured at 300 K and 30 K are shown in Fig. 5.2.4. At room temperature the resonance frequency is 17.7 MHz and quality factor is 120, while at 30 K the frequency rises to 35.7 MHz and quality factor to 22,000. The quality factor is comparable to the state of the art record of monolayer semiconductor nanoresonators [58]. For the temperature range from 30 K to 46 K, the resonance frequency and quality factor are plotted in Fig. 5.2.5. Both of them decreases with increasing temperature.

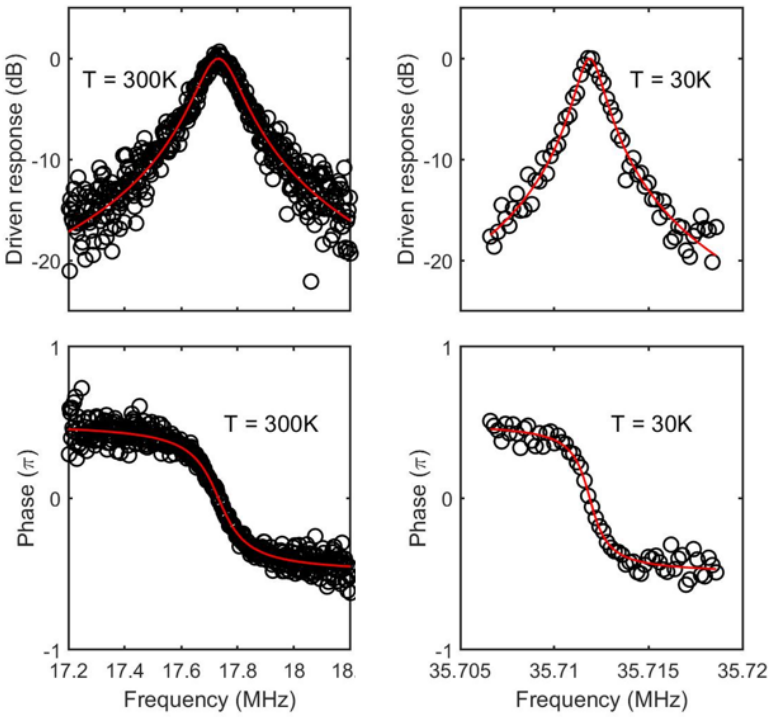

Figure 5.2.4 | Mechanical response of the device at room and cryogenic temperatures.

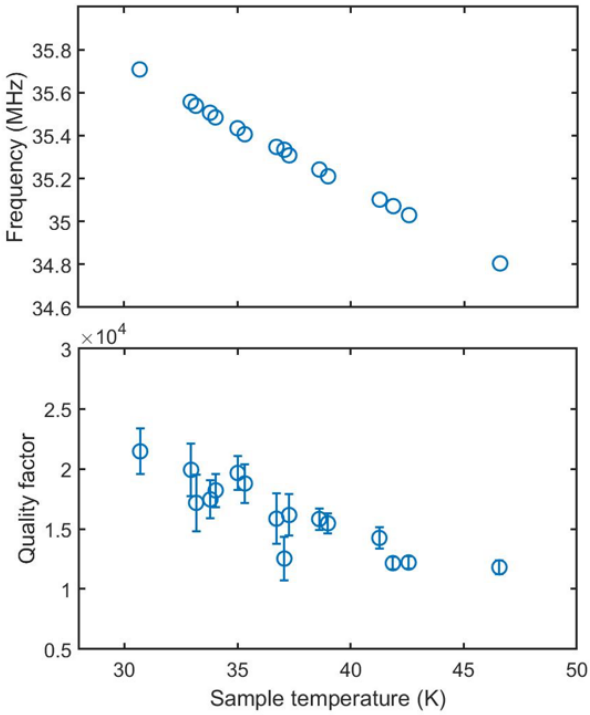

Figure 5.2.5 | Mechanical frequency and quality factor at the low temperature range.

5.3 Measurement setup and signal acquisition

The measurement setup is shown in Fig. 5.3.1. A continuous wave (CW) linearly polarized pump beam (633 nm) passes through an electro-optical modulator (EOM) (Conoptics, model: 350-160) which modulates the laser polarization between horizontal (H) and vertical (V) while keeps the optical intensity constant. The pump polarization is further adjusted by a half wave-plate. Before incident onto the cryostat, it passes through a quarter wave-plate (QWP1). Depending on the angle (θ) between the pump polarization and QWP1 axis, the pump polarization is modulated with LCP-RCP ($\theta = -\pi/4$), H-V ($\theta = 0$), and RCP-LCP ($\theta = +\pi/4$). To examine the polarization modulation, the laser is directed onto a polarizing beam-splitter by a flippable mirror and collected by two AC photodetectors. Typical time-domain signals from the oscilloscope are shown in Fig. 5.3.2, which shows the square-wave modulation of the polarization and constancy of the laser intensity.

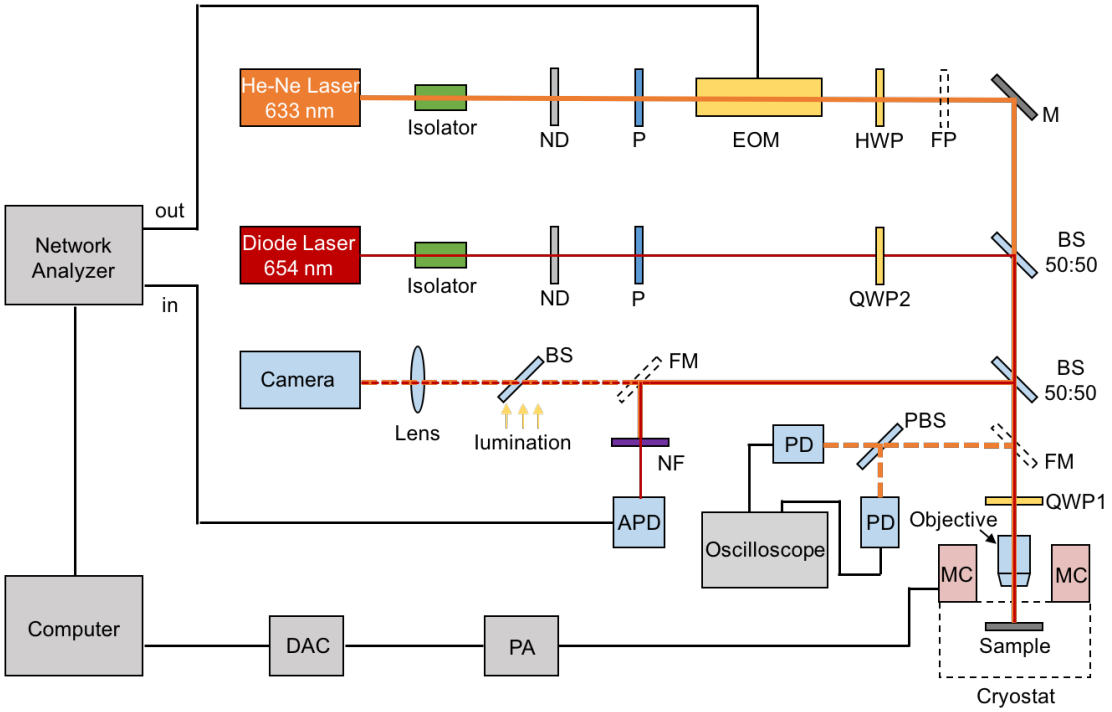

Figure 5.3.1 | Schematics of the measurement setup. (EOM: electro-optical modulator, ND: neutral density filter, P: polarizer, FP: flippable polarizer, HWP: half wave-plate, QWP: quarter wave-plate, M: mirror, BS: beam-splitter, FM: flippable mirror, MC: magnetic coil, PBS: polarization beam-splitter, PD: photodetector, NF: notch filter, APD: avalanche photodetector, DAC: digital analog converter, PA: power amplifier).

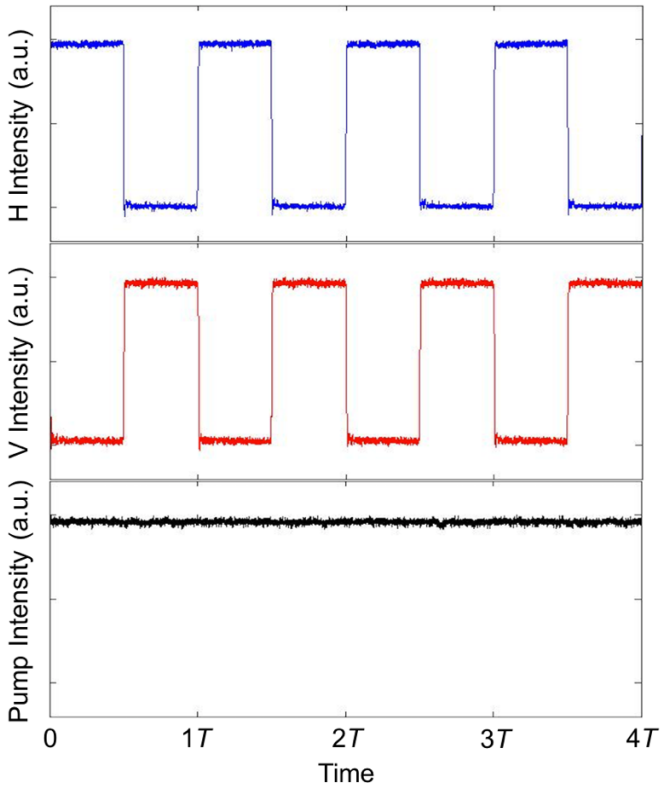

Figure 5.3.2 | Time-domain signal showing the H and V polarization components of the pump light before QWP1. The polarization modulation frequency is close to the mechanical resonance ~36 MHz.

A CW probe beam (654 nm) is used for interferometric detection of the resonator motion. It joins the pump beam through a 50/50 beam-splitter. An additional quarter wave-plate (QWP2) is placed in its path to compensate the effect of QWP1 placed before the objective. This makes sure that the probe light incident onto the sample is always linear polarized. Both the pump and probe beam are focused down to ~1 μm spot size using a long working distance objective and normally incident onto the sample. The reflected light passes through a notch filter, which blocks the pump beam, and is focused onto an avalanche photodetector (APD). The signal from the APD then goes to a network analyzer which controls the modulation frequency of the EOM.

A magnetic coil placed in front of the cryostat generates an out-of-plane magnetic field at the sample, which is distorted locally around the monolayer by the permalloy film to generate the field gradient. The magnetic field from the coil is calibrated using a Hall probe. The current of the coil is supplied by a bipolar power amplifier (Kepco, model: BOP 100-4). A digital analog converter (DAC) controls the output current of the power amplifier and thus controls the magnitude and direction of the magnetic field gradient.

Because of the low laser power used in the measurement (~11 μW for pump and ~4 μW for probe), the interferometric detection is not able to resolve the thermomechanical noise of the resonator, which is commonly used for calibrating the resonator displacement. In order to obtain the actual displacement of the resonator and the force acting on it, we extract the permittivity of MoS_2 monolayer with reflection spectroscopy and calculate the displacement detection responsivity with multilayer optical transfer-matrix method.

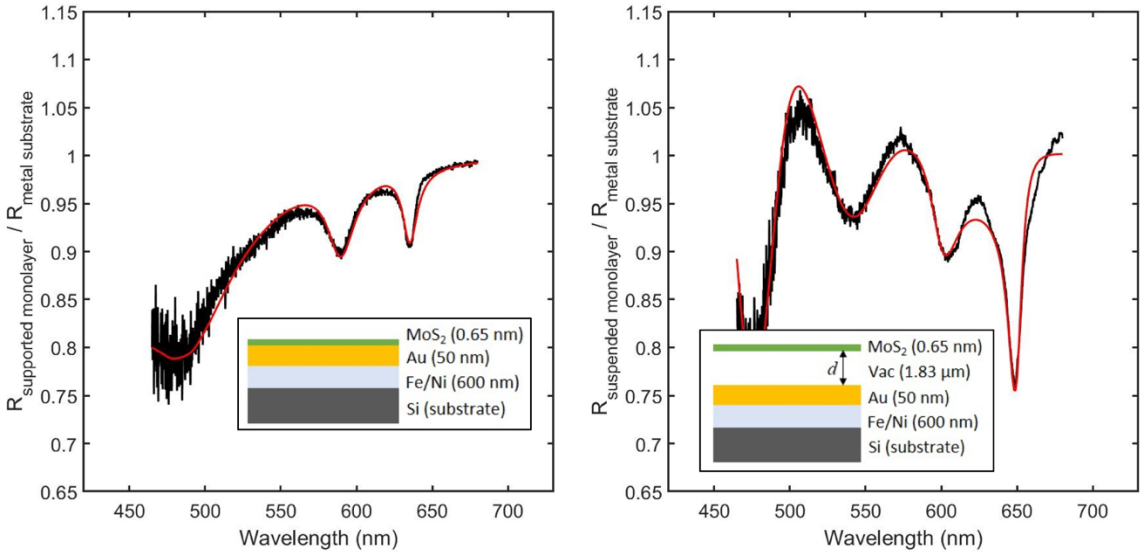

Figure 5.3.3 | Reflection spectrum of the supported (left) and suspended (right) monolayer MoS_2 normalized by the reflection from substrate. The red line is obtained by fitting the MoS_2 permittivity with the model described by Eq. (5.3.1). The inset shows the multi-layer stack used in the calculation.

The reflection spectrum of a supported MoS_2 and that of a suspended MoS_2 (normalized by the reflection from the substrate) are shown in Fig. 5.3.3. For suspended monolayer, the reflection spectrum displays interference fringes, and the exciton absorption peaks are slightly red-shifted due to film stress. To obtain the optical constants, we follow the approach used in Ref. [65]. Assuming that the permittivity of MoS_2 monolayer consists of a sum of Lorentzians, we have

$$\epsilon_{1L-MoS_2}(\omega) = C \cdot \epsilon_{con}(\omega) + \frac{\omega_{p,1}^2}{\omega_1^2 - \omega^2 + i\Gamma_1\omega} + \frac{\omega_{p,2}^2}{\omega_2^2 - \omega^2 + i\Gamma_2\omega} \qquad (5.3.1)$$

The first term $C \cdot \epsilon_{con}(\omega)$ accounts for contributions from oscillators of high energy. Here we use the same value of $\epsilon_{con}(\omega)$ as Ref. [65] and use a proportional constant C as a fitting parameter. For the oscillator terms, we use two Lorentzians to account for the two exciton peaks observed in the reflection spectra. With this model, the reflection spectra from the

multi-layer stacks can be calculated using the standard transfer-matrix method. The fitted reflection spectra show well agreement with the measurement results.

After obtaining the permittivity of the monolayer MoS_2, we calculate the displacement detection responsivity with optical transfer matrices [66]. The calculated optical reflection from the suspended monolayer device and the detection responsivity at the probe wavelength 654 nm are plotted as functions of the separation between the suspended monolayer and the substrate in Fig. 5.3.4. At 1.83 μm, the detection responsivity is -0.45 %/nm. This value is used to calibrate the actual displacement of the resonator.

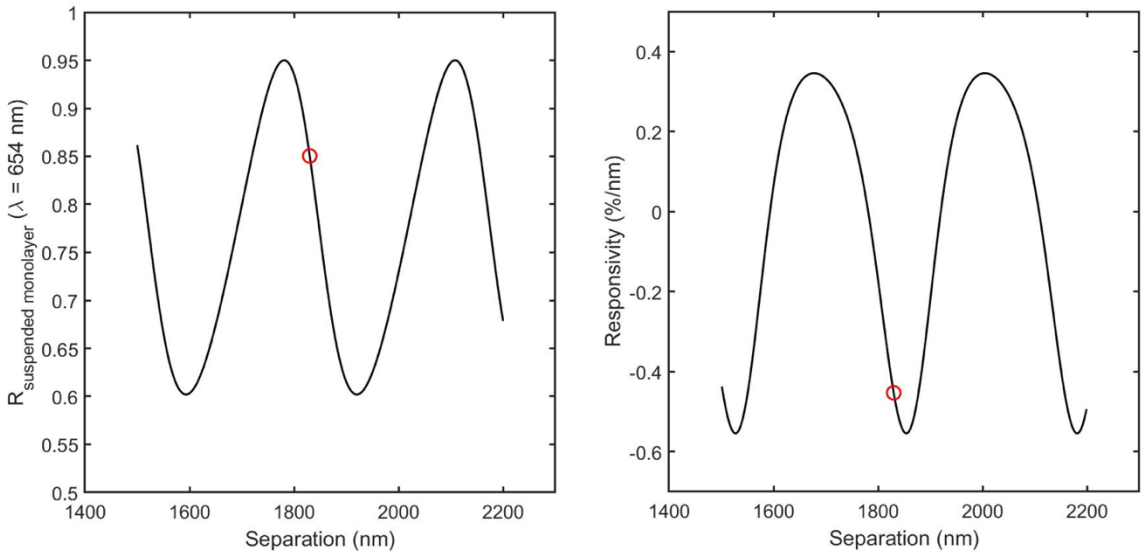

Figure 5.3.4 | Optical reflection and displacement detection responsivity of suspended monolayer MoS_2 at $\lambda = 654$ nm as a function of separation between the monolayer and bottom gold surface calculated using transfer-matrix method.

In the measurement, we employ a double lock-in scheme to single out the valley-mechanical actuation and eliminate the effects of other forces such as the thermo-optical or optical radiation pressure. In this scheme, both the pump laser polarization and magnetic field gradient direction are modulated, as shown in Fig. 5.3.5. Under such condition, only the demodulated signals that correspond to both modulations are measured. The polarization modulation signal has a frequency close to the mechanical resonance frequency and is demodulated in the network analyzer. The magnetic gradient modulation has a frequency of ~0.1 Hz and is demodulated through an in-house computer program.

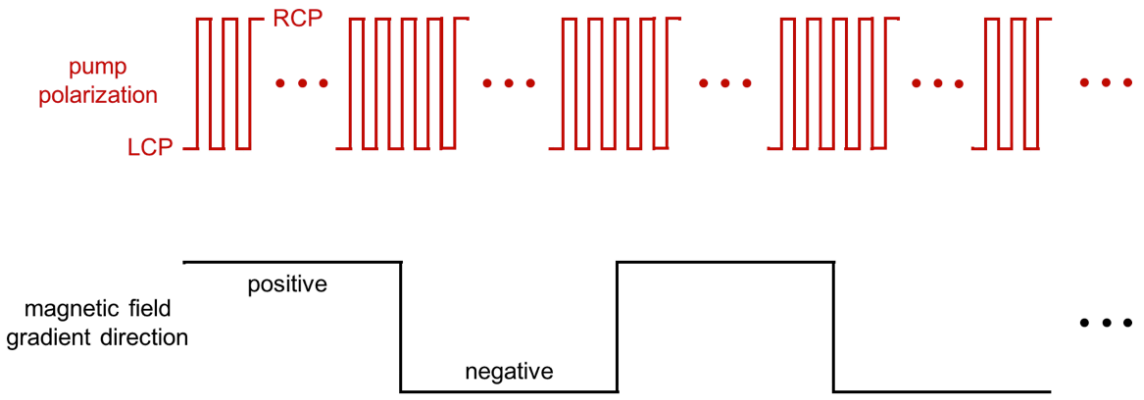

Figure 5.3.5 | Double lock-in scheme to single out the valley-mechanical actuation.

Due to the local laser heating effects, the mechanical resonance frequency is sensitive to the laser spot position on the suspended monolayer. To acquire clean signals of the valley-actuated mechanical motion, it is crucial to stabilize the mechanical resonance by reducing the vibration of the cryostat stage. Another important strategy is to place the laser spots right at the center of the suspended area. Under such condition, the mechanical resonance can be insensitive to the relative displacement between the sample and the laser spots. This critical condition is achieved by precisely varying the laser spot position with piezoelectric motors and searching for the lowest mechanical resonance frequency of the sample.

5.4 Observation and control of valley-mechanical actuation

We observe valley-actuated mechanical motion of the MoS_2 monolayer at low temperature. We alternatingly populate the K and K' valleys by modulating the polarization of the pump beam (633 nm) between left-circular and right-circular (LCP and RCP) while keeping the light intensity constant (with methods discussed in the above Chapter). This modulation results in an oscillating push-pull force that drives the mechanical resonator. The measured mechanical displacement exhibits a Lorentzian shape response that follows the previously characterized mechanical susceptibility, as shown in Fig. 5.4.1a. In contrast, a linearly-polarized pump shows no driving effect because it equally populates both valleys and therefore the net force is zero.

As we switch the pump polarization to opposite helicity, the mechanical displacement displays a π-phase difference, as shown in Fig. 5.4.1b, which confirms that population of different valleys exerts opposite forces onto the material. An opposite magnetic field gradient also induces a π-phase shift of the displacement by switching the sign of the force.

In the measurement, the polarization modulation (close to the mechanical resonance ~36 MHz) is much slower than the depopulation of the valley carriers, whose timescale is between picoseconds and a few nanoseconds [42,67-69]. As a consequence, the valley population adiabatically follows the polarization modulation of the pump light.

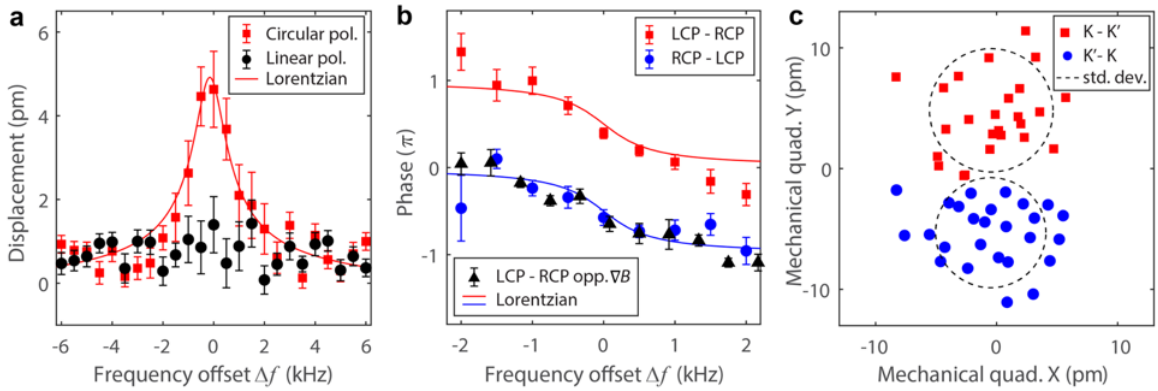

Figure 5.4.1 | **a**, The mechanical displacement driven by circularly- and linearly-polarized pump. Δf is the frequency offset from the mechanical resonance. **b**, Phase response of the driven motion with opposite pump helicity and magnetic field gradient. **c**, The mechanical quadratures of the monolayer driven resonantly by opposite valley excitation. Black dashed lines indicate the standard deviation.

Utilizing the fact that the direction of the force depends on which valley is populated, we demonstrate transduction of the valley excitation into the mechanical state of the nano-resonator. We examine the mechanical quadratures of the monolayer when it is resonantly driven by opposite valley carrier population, as shown in Fig. 5.4.1c. Using a measurement bandwidth of 1 kHz with 1024 averages, we resolve two distinct mechanical states with opposite phases and similar amplitudes. The confidence level of differentiating the two states is approaching unity, according to the independence sample T-test. This result demonstrates that the valley excitation of the monolayer is unambiguously transferred into the mechanical states.

We further quantify the dependence of valley-mechanical force on the pump light and magnetic field gradient. We obtain the force through the measurement of the mechanical displacement and susceptibility with methods discussed in the above Chapter. By varying the angle θ between the quarter-waveplate axis and the pump laser polarization from $-\pi/4$ (LCP) to 0 (linearly-polarized) and to $+\pi/4$ (RCP), the measured force shows a $|\sin 2\theta|$ dependence, as shown in Fig. 5.4.2a, which verifies that the force is proportional to the net valley population. This relation is further confirmed by a measurement of the pump power dependence shown in Fig. 5.4.2b. We also observe that the valley-mechanical force increases linearly as a function of the out-of-plane magnetic field gradient, as shown in Fig. 5.4.2c. This observation verifies that the measured force is originated from the magnetic moment of

the valley polarized carriers. The above results demonstrate effective control over the valley-mechanical interaction through various external conditions.

The valley-mechanical force also displays a strong dependence on temperature, as shown in Fig. 5.4.2d. The force becomes observable when the sample temperature is lowered below 46 K and rises steadily as the temperature is further reduced. These can be attributed to the increase of the steady state net valley populations at lower temperatures due to longer valley polarization lifetime. The temperature dependence of the valley-mechanical force roughly follows exp (Δ/k_BT) with $\Delta \sim 23$ meV. This characteristic energy matches the phonon energy of monolayer MoS_2 at K point, which suggests that such an activation behavior may be caused by phonon-assisted intervalley scattering [41,70].

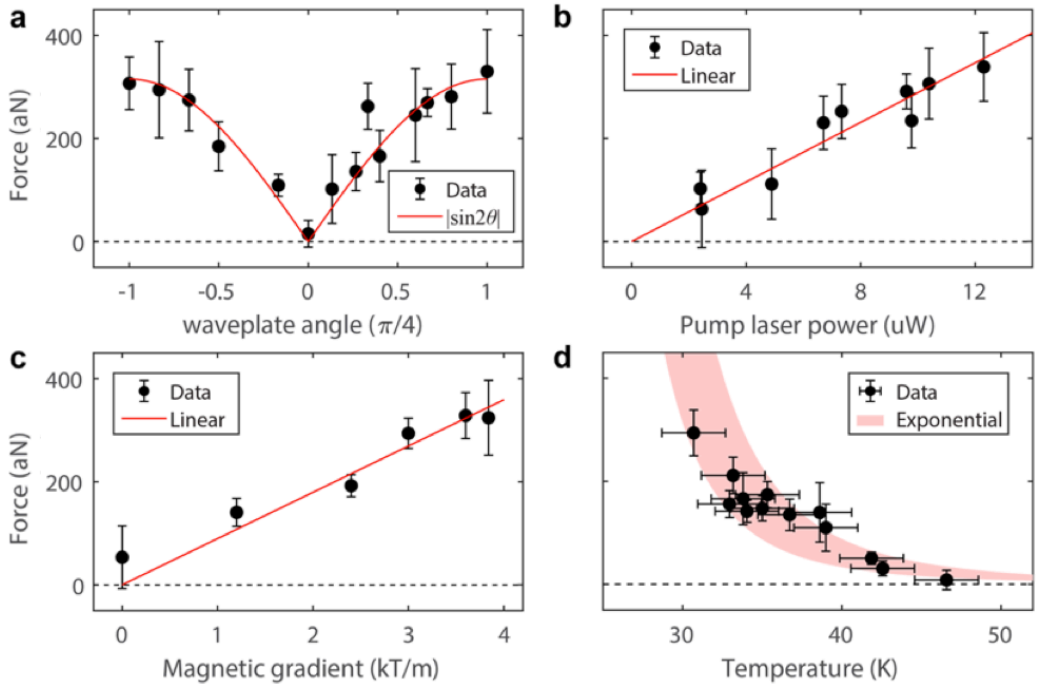

Figure 5.4.2 | Dependence of the valley-mechanical force on the angle θ between the quarter wave-plate axis and the pump laser polarization (**a**), the pump laser power (**b**), the magnetic field gradient (**c**), and the temperature (**d**). Error bars represent the standard errors of the signals. The red band in (d) shows the error estimates obtained from the fitting of the data with the exponential dependence.

From the measured valley-mechanical force, the number of imbalance valley carriers can be calculated from $F = (N_K - N_{K'})g\mu_B\nabla B$. Using the Lande g-factor of 4 for monolayer MoS_2 [71], the number of imbalance valley carriers is estimated to be ~2000. These carriers mainly distribute in the ~1 μm laser spot of the pump light, resulting an imbalance valley carrier density of ~2×10^{11} cm^{-2}, which agrees with the number reported in Ref. [43] for the same

pump intensity of ~11 μW/μm^2. From the rate equation $dN/dt = -N/\tau_v + \alpha P/\hbar\Omega_o$, the valley population at steady state is given by $N = \tau_v \alpha P/\hbar\Omega_o$, where τ_v is the valley lifetime, α the optical absorption, P the pump laser power, and $\hbar\Omega_o$ the photon energy of the pump laser. The calculated valley lifetime is $\tau_v \sim 0.4$ ns. This number is comparable to the reported valley lifetime for resident carriers (electrons or holes) in monolayer MoS_2 [42,68]. With the zero-point motion of $x_{zpf} = 0.11$ pm, the single-phonon coupling rate is calculated to be $g_0/2\pi = g\mu_B \nabla B x_{zpf}/h = 24$ Hz.

5.5 Conclusion and outlook

We have realized coupling of valley and mechanical degrees-of-freedom in a monolayer MoS_2 and demonstrated direct transduction of valley excitation into mechanical states. Stronger valley-mechanical coupling rate can be obtained using magnetic nanostructure which can enhance the magnetic field gradient (up to 10^7 T/m [72]). The valley lifetime ($\tau_v = 1/\gamma_v$) can be extended up to ~1 μs by using 2D heterostructure of MoS_2/WSe_2 to spatially separate the electron and hole layers [73]. With both improvements mentioned above, a single-valley cooperativity (defined as $C_0 = 4g_0^2/\gamma_v\gamma_m$) exceeding 1 is achievable, which would enable us to explore quantum coherent effects of valley-mechanical interaction.

Our experiment facilitates hybridizing valley pseudospin with other information carriers, such as microwave photons and superconducting qubits. The valley-mechanical coupling also lays the foundation for new types of valley-actuated mechanical devices. One interesting example is the "valley switch" which uses a valley signal to switch another valley signal - an analogue of electronic transistor.

Remark: Chapter 4 and Chapter 5 include materials from H.-K. Li*, K. Y. Fong*, et al. "Valley optomechanics in a monolayer semiconductor." (to appear in *Nature Photonics*) (*contributed equally).

Chapter 6

Phonon heat transfer across the quantum vacuum

6.1 Background and motivation

In the theory of quantum mechanics, quantum fields are never at rest but constantly fluctuate even at absolute zero temperature. These fluctuations lead to extraordinary consequences in many areas ranging from atomic physics (e.g. spontaneous emission [74] and the Lamb shift [75]) to cosmology (e.g. the Hawking radiation [76]). In 1948, based on quantum fluctuations of electromagnetic fields, Casimir described a bizarre force acting between neutral objects [77]. Today, probing this effect is of both fundamental interest in quantum field theory and practical importance in nano-/micro- technology [78,79].

While the mechanical consequences of the Casimir effect have been extensively studied and precisely quantified [80-87], its role in thermodynamics is rarely explored. Recently, it is predicted that the Casimir force can induce phonon tunneling between nearby objects and thus transfer heat through a vacuum gap [11-13]. This unique quantum effect represents a different heat transfer mechanism from the conventional concepts of conduction, convection, and radiation. However, such prediction has not been experimentally observed due to the stringent requirements under sub-nanometer gaps. At such small distances, other effects such as evanescent electric fields, charge-charge interaction, and surface phonon polaritons may contribute and obscure the experimental verification [88-91].

In this Chapter, we provide a scheme to observe heat transfer between two objects driven by quantum vacuum fluctuations [14]. We utilize nanomechanical systems to access individual phonon modes and resonantly enhance the thermal energy exchange. With this strategy, the distance range in which the phenomenon becomes significant is boosted up by over two orders of magnitude to hundreds of nanometers, allowing us to rule out other short-range effects. In the following Chapter, we present experimental observation of Casimir strong phonon coupling and the resulting thermal energy transfer. Our experiment reveals a new mechanism of heat transfer through the quantum vacuum. It also opens new opportunities to study quantum thermodynamics and energy transport using nanomechanical devices.

6.2 Introduction to the Casimir force

Long-range forces that act between electrically neutral objects have been discussed for centuries. However, only after the development of quantum mechanics and quantum field theory has the physical picture of these forces become clear and the first quantitative results obtained. The origin of both the Casimir and van der Waals forces is connected to quantum fluctuations, which are the temporary changes of the fields in space, as explained in the Heisenberg uncertainty principle. For each mode (or harmonic oscillation) in space with frequency ω, the lowest possible energy is $\hbar\omega/2$. Summing over all possible oscillators at all points in the whole space gives an infinite quantity, which can be viewed as the energy of the vacuum.

The Casimir force can be understood as a result of electromagnetic vacuum energy change by bulk bodies. Their presence in vacuum changes the electromagnetic boundary conditions and thus affects the mode distribution and the total vacuum energy, as illustrated in Fig. 6.1.1. The total energy change heavily depends on the distance between the two objects and the Casimir force is obtained by taking the first derivative. For two parallel perfect conducting plates, the Casimir force per area is given by $F_{Cas}(d) = -\hbar c\pi^2/240d^4$ [77]. In reality, the dispersion of the material needs to be considered and the Casimir force can be calculated with the Lifshitz formula [78]. Today, experimental quantification of the Casimir force plays an important role in the development of quantum field theory and micro/nano- technologies.

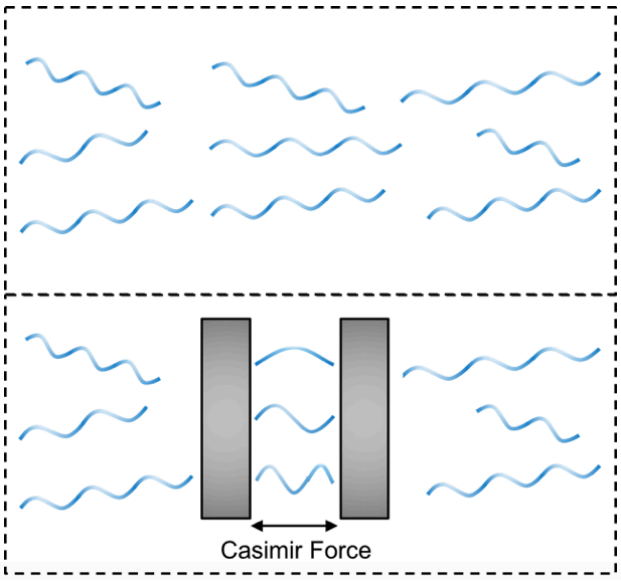

Figure 6.1.1 | Upper: electromagnetic modes in vacuum. Lower: the two objects modify the boundary conditions of electromagnetic fields and changes the total electromagnetic vacuum energy. As a result, the Casimir force emerges.

6.3 Phonon heat transfer driven by the Casimir force

In conventional theory, thermal radiation is the only heat carrier across the vacuum [92]. The story is quite different when two objects are placed in proximity. Near-field thermal radiation emerges when the surface distance is below the wavelengths of thermal photons. Similarly, other near-field mechanisms would also come into play (or even become dominant) as the distance is smaller than the characteristic wavelengths of the energy carriers. Electrons, phonons, phonon-polaritons and so on can tunnel through the vacuum gap through various mechanisms and transfer heat. Understanding these complex processes of energy transfer at the nanoscale is of both fundamental interests and practical significance. With the strong quest of scaling down information, energy, and manufacturing technologies, it is important to know how to manage heat at short length scales.

In many solids, most of the thermal energy lies in the phonon spectrum. Recent theories raise the possibility that phonons may tunnel across the vacuum from one surface to another, mediated by the Casimir force [11-13]. Intuitively, this heat transfer mechanism can be understood as follows. The thermal vibration of some phonon modes in solids could lead to surface displacement, as shown in Fig. 6.2.1. Since the Casimir force depends on the relative distance between the two surfaces, an oscillating force across the vacuum emerges, resulting the coupling between the phonon modes in the two nearby objects. As a consequence of this Casimir coupling, thermal energy is transferred across the phonon modes from the hot to the cold side.

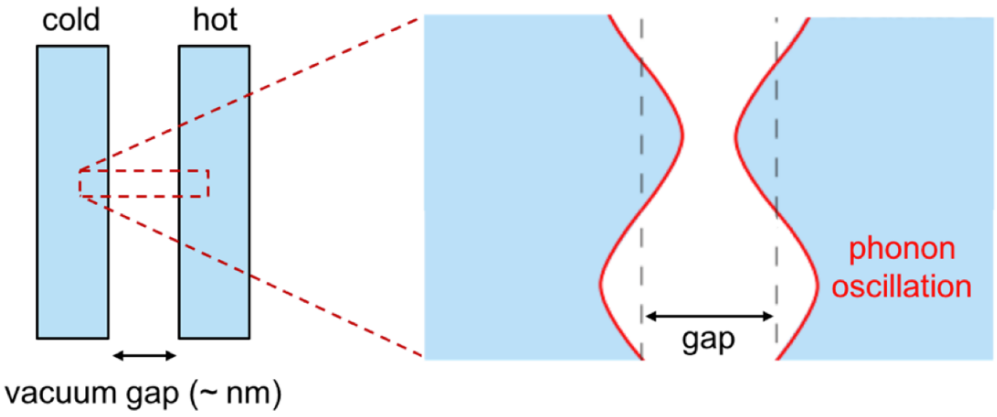

Figure 6.2.1 | Two objects with different temperatures separated by a vacuum gap (left). A zoom-in cartoon picture (right) shows the phonon oscillations that cause the infinitesimal displacements of the object surfaces, which give rise to oscillating force across the vacuum due to the Casimir effect.

6.4 Casimir coupling between individual phonon modes

According to previous calculations, the Casimir phonon heat transfer becomes prominent only when the separation between bulk solids is at sub-nanometer scale [11,12], which is challenging to achieve in experiment. Moreover, at such small distances, other effects such as charge-charge interaction, evanescent electric fields, and surface phonon polaritons may contribute and obscure the experimental verification. To single out the phonon coupling effects driven by the Casimir force, we use nanomechanical oscillators that allow us to access individual phonon modes. The energy transfer can be strongly enhanced under resonance condition, and the distance range in which the phenomenon becomes significant can be boosted up to hundreds of nanometers.

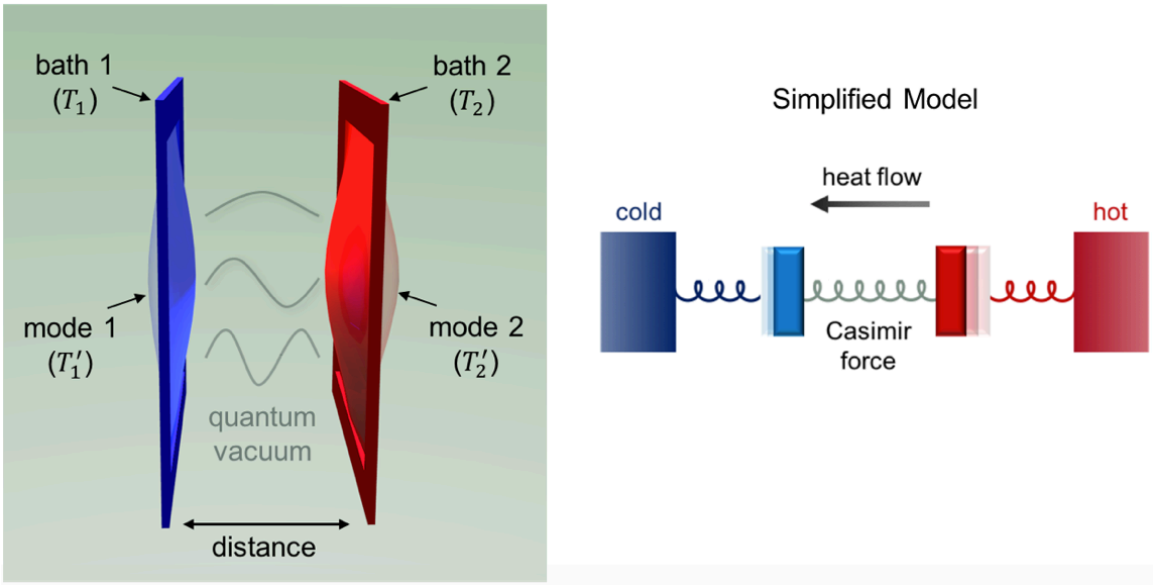

Figure 6.3.1 | Two mechanical membranes are clamped to substrates with different temperatures (left). Their fundamental phonon modes are resonantly coupled through the Casimir force, as described by the simplified model (right). As a result, heat is transferred from the hot to the cold side.

In a specific case shown in Fig. 6.3.1, we consider the fundamental modes of two parallel nanomechanical membranes that are resonantly coupled to each other through the Casimir interaction. The two membranes are clamped to substrates at different temperatures (T_1 and T_2). In the regime where thermal Brownian motions of the phonon modes are much slower than the response time of the Casimir effect, the Casimir force acts instantaneously and is conservative in nature [93-95]. The Casimir interaction effectively acts as a coupling spring that connects the two modes, through which the thermal energy is transferred from the hot

to the cold side. The whole system can be described by a simplified spring-mass model shown on the right side of Fig. 6.3.1.

At large separation, the phonon modes of the membranes are in thermal equilibrium with their thermal baths, i.e., $T_1' = T_1$ and $T_2' = T_2$, where T_1' and T_2' are the mode temperatures determined by the thermal Brownian motion of the modes. At shorter distance, the Casimir interaction dominates and induces thermal energy exchange between the phonon modes. This causes observable deviation of the mode temperatures from their bath temperature. A detailed theoretical analysis is presented below.

We consider two parallel planes separated by a distance d, as shown in Fig. 6.3.2. Within the region $-L_i/2 < x, y < L_i/2$ (i = 1, 2), the membrane can make vertical displacement $u_i(x, y)$. The two membranes are connected to thermal baths at temperatures T_1 and T_2.

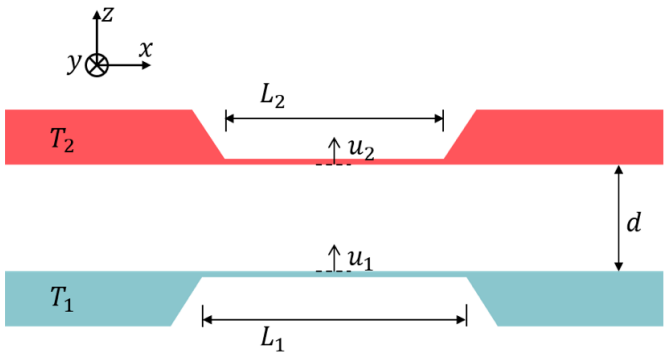

Figure 6.3.2 | Schematics of the structure under theoretical consideration.

Because of the quantum fluctuations of the electromagnetic field, there exists Casimir force acting between the two membranes. Since the phonon wavelength of the fundamental modes are much larger than the distance between the membranes, we can use the Proximity Force Approximation [96]. By expanding the force to the first order, the equations of motion for the two membranes with built-in tensile stress are given by

$$\sigma_1 \nabla^2 u_1(x,y,t) + F'_{Cas}(d)\big(u_1(x,y,t) - u_2(x,y,t)\big) = \rho \frac{\partial^2 u_1(x,y,t)}{\partial t^2} \qquad (6.3.1)$$

$$\sigma_2 \nabla^2 u_2(x,y,t) + F'_{Cas}(d)\big(u_2(x,y,t) - u_1(x,y,t)\big) = \rho \frac{\partial^2 u_2(x,y,t)}{\partial t^2} \qquad (6.3.2)$$

Here, we assume that the two membranes have the same density ρ (mass per area) but different stress σ_1 and σ_2. The stress depends on the bulk temperatures and therefore can be controlled. F_{Cas} represents the Casimir force per area, which depends on the displacement profiles of both membranes.

For tensile-stressed membranes, the fundamental eigenmode profile is given by $u_i(x,y,t) = u_i(t)\cos(\pi x/L_i)\cos(\pi y/L_i)$ (i = 1, 2). When the Casimir force is small compared to the stress force, its existence does not affect the mode profile. Performing integration on both sides, we obtain

$$-\frac{\pi^2\sigma_1}{2}u_1 + F'_{Cas}(d)\left(\frac{L_1^2}{4}u_1 - Cu_2\right) = \rho\frac{L_1^2}{4}\ddot{u}_1 \tag{6.3.3}$$

$$-\frac{\pi^2\sigma_2}{2}u_2 + F'_{Cas}(d)\left(\frac{L_2^2}{4}u_2 - Cu_1\right) = \rho\frac{L_2^2}{4}\ddot{u}_2 \tag{6.3.4}$$

where the correction term C accounts for the mode profile mismatch, i.e.,

$$C = \left[\int_{-\min\{L_1,L_2\}/2}^{\min\{L_1,L_2\}/2} dx\cos\frac{\pi x}{L_1}\cos\frac{\pi x}{L_2}\right]^2 \tag{6.3.5}$$

The two coupled equations can be rewritten as

$$\ddot{u}_1 + \Omega^2 u_1 - 2\Omega g_C(u_1 - \alpha_1 u_2) = 0 \tag{6.3.6}$$

$$\ddot{u}_2 + \Omega^2 u_2 - 2\Omega g_C(u_2 - \alpha_2 u_1) = 0 \tag{6.3.7}$$

assuming the resonance frequencies of the of the two mechanical modes are matched through temperature control of the stress ($\Omega = \Omega_1 = \Omega_2$). The coupling rate g_C and the correction factor α_i are given by $g_c = F'_{Cas}(d)/2\Omega\rho$ and $\alpha_i = 4C/L_i^2$, respectively. We employ the Langevin formula to describe thermal fluctuation and dissipation [97,98]

$$\ddot{u}_1 + 2\gamma_1\dot{u}_1 + \Omega^2 u_1 - 2\Omega g_C(u_1 - \alpha_1 u_2) = \delta F_1/m_1 \tag{6.3.8}$$

$$\ddot{u}_2 + 2\gamma_2\dot{u}_2 + \Omega^2 u_2 - 2\Omega g_C(u_2 - \alpha_2 u_1) = \delta F_2/m_2 \tag{6.3.9}$$

where the fluctuating forces are related to the bath temperatures T_i and mechanical dampings γ_i by $\langle\delta F_i(t)\delta F_j(t')\rangle = \delta_{ij}\delta(t-t')8k_B T_i\gamma_i m_i$. The effective mass m_i is given by one quarter of the total mass of the resonator, i.e., $m_i = L_i^2\rho/4$. Using the quadrature notations defined as $q(t) = \left[\tilde{q}(t)e^{-i\Omega t} + \tilde{q}^*(t)e^{i\Omega t}\right]/2$ for $q \in \{u_1, u_2, \delta F_1, \delta F_2\}$ and assuming $\gamma_i \ll \Omega$, we obtain

$$\dot{\tilde{u}}_1 + \gamma_1\tilde{u}_1 - ig_C(\tilde{u}_1 - \alpha_1\tilde{u}_2) = i\delta\tilde{F}_1/2\Omega m_1 \tag{6.3.10}$$

$$\dot{\tilde{u}}_2 + \gamma_2\tilde{u}_2 - ig_C(\tilde{u}_2 - \alpha_2\tilde{u}_1) = i\delta\tilde{F}_2/2\Omega m_2 \tag{6.3.11}$$

In the frequency domain, they become

$$\begin{pmatrix} \omega + g_C + i\gamma_1 & -g_C\alpha_1 \\ -g_C\alpha_2 & \omega + g_C + i\gamma_2 \end{pmatrix} \begin{pmatrix} \tilde{u}_1[\omega] \\ \tilde{u}_2[\omega] \end{pmatrix} = -\frac{1}{2\Omega} \begin{pmatrix} \delta\tilde{F}_1[\omega]/m_1 \\ \delta\tilde{F}_2[\omega]/m_2 \end{pmatrix}, \tag{6.3.12}$$

which lead to the spectral densities

$$S_{\tilde{u}_1^*\tilde{u}_1}[\omega] = \frac{[(\omega + g_C)^2 + \gamma_2^2]2k_BT_1\gamma_1/m_1 + g_C^2\alpha_1^2 2k_BT_2\gamma_2/m_2}{\Omega^2[[(\omega + g_C)^2 - \gamma_1\gamma_2 - g_C^2\alpha_1\alpha_2\,]^2 + (\gamma_1 + \gamma_2)^2(\omega + g_C)^2]} \tag{6.3.13}$$

$$S_{\tilde{u}_2^*\tilde{u}_2}[\omega] = \frac{[(\omega + g_C)^2 + \gamma_1^2]2k_BT_2\gamma_2/m_2 + g_C^2\alpha_2^2 2k_BT_1\gamma_1/m_1}{\Omega^2[[(\omega + g_C)^2 - \gamma_1\gamma_2 - g_C^2\alpha_1\alpha_2\,]^2 + (\gamma_1 + \gamma_2)^2(\omega + g_C)^2]}. \tag{6.3.14}$$

The mean square of the phonon mode displacements are related to the spectral densities by $\langle|\tilde{u}_i|^2\rangle = \int_{-\infty}^{\infty} d\omega\, S_{\tilde{u}_i^*\tilde{u}_i}[\omega]/2\pi$. Using $k_BT_i' = m_i\Omega^2\langle u_i^2\rangle$, the mode temperatures can be expressed as

$$T_1' = \int_{-\infty}^{\infty} \frac{d\omega}{\pi} \frac{[(\omega + g_C)^2 + \gamma_2^2]T_1\gamma_1 + g_C^2\alpha_1\alpha_2 T_2\gamma_2}{[(\omega + g_C)^2 - \gamma_1\gamma_2 - g_C^2\alpha_1\alpha_2\,]^2 + (\gamma_1 + \gamma_2)^2(\omega + g_C)^2} \tag{6.3.15}$$

$$T_2' = \int_{-\infty}^{\infty} \frac{d\omega}{\pi} \frac{[(\omega + g_C)^2 + \gamma_1^2]T_2\gamma_2 + g_C^2\alpha_1\alpha_2 T_1\gamma_1}{[(\omega + g_C)^2 - \gamma_1\gamma_2 - g_C^2\alpha_1\alpha_2\,]^2 + (\gamma_1 + \gamma_2)^2(\omega + g_C)^2} \tag{6.3.16}$$

In some special cases, the above integrals can be carried out analytically.

Case 1: $g_C \ll \gamma_1, \gamma_2$ (weak coupling)

$$T_1' = T_1, \quad T_2' = T_2 \tag{6.3.17}$$

Case 2: $g_C \gg \gamma_1, \gamma_2$ (strong coupling)

$$T_1' = T_2' = T_{th}' = \frac{T_1\gamma_1 + T_2\gamma_2}{\gamma_1 + \gamma_2} \tag{6.3.18}$$

Case 3: $\gamma_1 = \gamma_2 = \gamma$ and $L_1 = L_2 = L$

$$T_1' = \frac{T_1\left(1 + \frac{g_c^2}{2\gamma^2}\right) + T_2\frac{g_c^2}{2\gamma^2}}{1 + \frac{g_c^2}{\gamma^2}}, \qquad T_2' = \frac{T_2\left(1 + \frac{g_c^2}{2\gamma^2}\right) + T_1\frac{g_c^2}{2\gamma^2}}{1 + \frac{g_c^2}{\gamma^2}} \tag{6.3.19}$$

In case 3, the mode temperatures are solely determined by the ratio $(g_C/\gamma)^2$. Note also that $g_C \propto F'_{Cas}(d)$, therefore, the Casimir heat transfer effect rises sharply at short distance.

Net energy flow rate from the thermal bath to the mode can be calculated from

$$P_i = \langle(\delta F_i - 2\gamma_i m_i \dot{u}_i) \cdot \dot{u}_i\rangle = 2\gamma_i k_B (T_i - T_i') \tag{6.3.20}$$

In the strong coupling regime ($g_C \gg \gamma_1, \gamma_2$), we obtain

$$P_2 = -P_1 = \frac{2\gamma_1\gamma_2}{\gamma_1 + \gamma_2} k_B (T_2 - T_1) \tag{6.3.21}$$

The above theoretical model is picturized below in Fig. 6.3.3.

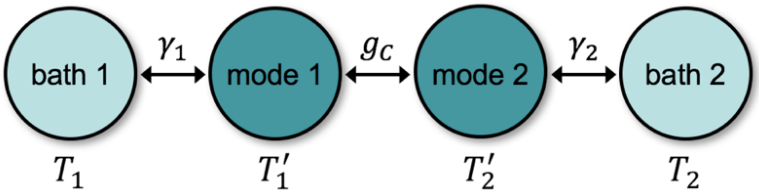

Figure 6.3.3 | Illustration of the theoretical model which includes the mode-mode Casimir coupling and mode-bath interactions.

6.5 Experimental design

Our experimental design is shown in Fig. 6.4.1. Two tensile stressed stoichiometric Si_3N_4 membranes of different dimensions (330×330×0.1 μm^3 and 280×280×0.1 μm^3) are coated with gold (75 nm) on both sides for the purposes of optical reflection and electrical contact. The mesa structure on the left sample and the electrical pads on the right sample are created for high precision parallel alignment (details will be discussed in the next Chapter). Partially reflecting mirrors (M_1 and M_2) are placed behind the membranes, and CW laser beams (633 nm) are sent from both sides to interferometrically measure the thermo-mechanical motion of the membranes. The distance between the mirrors and the membranes are controlled by piezo-actuators with feedback loops to maintain long-term stability of the interferometric detection sensitivity. The samples are mounted on closed-loop thermoelectric cooler and heater to stabilize the bath temperatures and tune the mechanical resonance frequencies. A bias control voltage (V_b) is applied across the two membrane surfaces to compensate any built-in electrostatic potential that may overwhelm the Casimir effect.

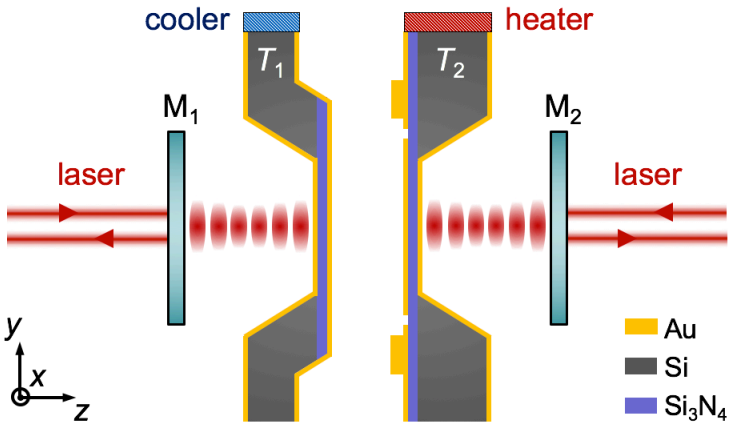

Figure 6.4.1 | Schematics of the experimental design with double optical interferometry to identify phonon thermal transfer driven by the Casimir force.

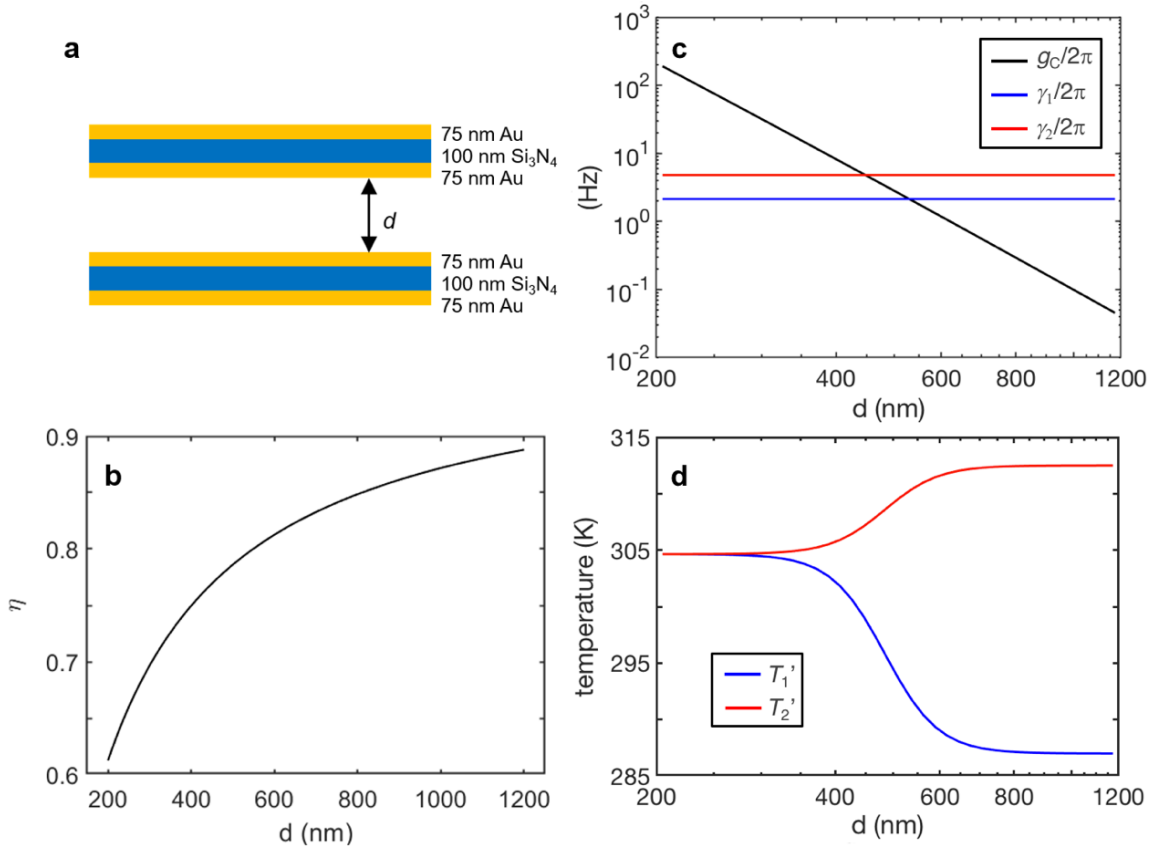

Figure 6.4.2 | **a,** Cross-sectional view of the layered structure used in the experiment. **b,** Calculated Correction factor η against the distance d. **c,** Calculated coupling rate g_C versus the distance d. **d,** Calculated mode temperatures $T_!'$ and T_2' as functions of distance d.

Taking into consideration the finite conductivity and dispersion of the gold film and also the geometry of the membrane structure as shown in Fig. 6.4.2a, the Casimir force per area can be written as

$$F_{Cas}(d) = -\eta \frac{\hbar c \pi^2}{240 d^4} \tag{6.3.22}$$

where η stands for the correction factor applied to the Casimir force between two planar perfect conductors. We numerically calculate the Casimir force using the Lifshitz theory and plot η as a function of distance in Fig. 6.4.2b. Details of the calculation method can be found in Ref. [78]. In the distance range that we concern (between 300 nm and 800 nm), η is between 0.70 and 0.85 according to the calculation.

Figure 6.4.2c compares the Casimir phonon coupling rate (g_C) with the mechanical damping rates (γ_1, γ_2). The corresponding mode temperatures T_1' and T_2' as a function of distance is shown in Fig. 6.4.2d. The results clearly show that thermalization (i.e., $T_1' = T_2'$) occurs when the system enters the strong coupling regime (i.e., $g_C \gg \gamma_1, \gamma_2$).

Chapter 7

Observation of the Casimir phonon heat transfer

In this Chapter, we present our experiments which lead to the realization of strong Casimir phonon coupling and the observation of the resulting thermal energy transfer across the vacuum. We fabricate the nanomechanical membranes and develop a delicate method to place them in parallel with high precision ($<10^{-4}$ rad). We quantify the temperature change of the fundamental phonon modes by measuring their thermal Brownian motion and show the thermalization of the two phonon modes in the strong Casimir phonon coupling regime. The observation agrees well with our theoretical prediction and is clearly distinguished from other effects such as near-field radiation and electrostatic interaction.

7.1 Device fabrication and parallel alignment

Figure 7.1.1 illustrates the device fabrication procedures. The process started with a silicon wafer (500 um thick) coated with LPCVD stoichiometric Si_3N_4 (100 nm thick) on both sides. Photolithography was performed at the backside of the wafer and SF_6 plasma etching was used to remove the Si_3N_4 at the opening windows. The silicon wafer was then etched through in KOH solution (25%, 80^{o}C, 7 hr), creating freestanding Si_3N_4 membranes at the frontside of the wafer.

For the left sample, a photolithography and SF_6 plasma etching were performed to define a square region (500 × 500 um^2) around the membrane, whose corners will contact with the spacers on the right sample. A short KOH (25%, 80^o C, 15 min) etch was used to create a mesa structure with a depth of around 25 μm. After the KOH wet etching, the sample was evaporated with 75 nm Au on both sides.

For the right sample, the first photolithography and liftoff were performed to pattern contact electrodes (75 nm Au) at the corners of the membrane. The second photolithography and liftoff were performed to pattern spacers (150 nm Au). After that, the backside of the sample is evaporated with 75 nm Au.

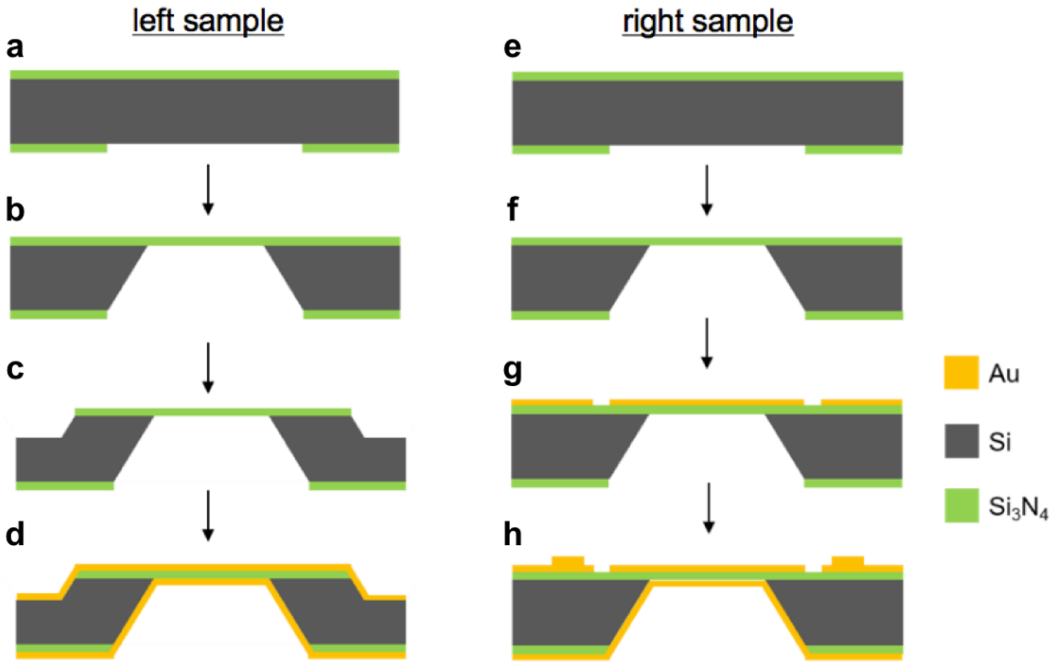

Figure 7.1.1 | Fabrication process flow for the left (**a-d)** and right (**e-h**) samples.

The optical images of the fabricated samples are shown in Fig. 7.1.2. The two suspended nanomechanical membranes have different lateral dimensions (330×330 μm^2 and 280×280 μm^2). To ensure the electrical access to the top surface on the left sample, a small portion of the Si_3N_4 at the corner of the mesa was released onto the bottom surface during the KOH etching, as shown in Fig. 7.1.2b. The evaporated Au eventually connects electricity from the bottom surface to the top of the mesa.

Cleanliness of the membrane surfaces is crucial for aligning the two membranes to short distances (about 300 nm). Samples are inspected under confocal microscope which can clearly identify small particles of ~100 nm size. To maintain high-degree of cleanliness, the sample fabrication, wire-bonding, and mounting of samples onto sample holders are all carried out in high-class cleanroom environment. The left and right samples are attached to a custom-made copper plate and a printed circuit board, respectively, as shown in Fig. 7.1.3. Surface roughness on the membranes is characterized to be less than 1.5 nm using atomic force microscopy.

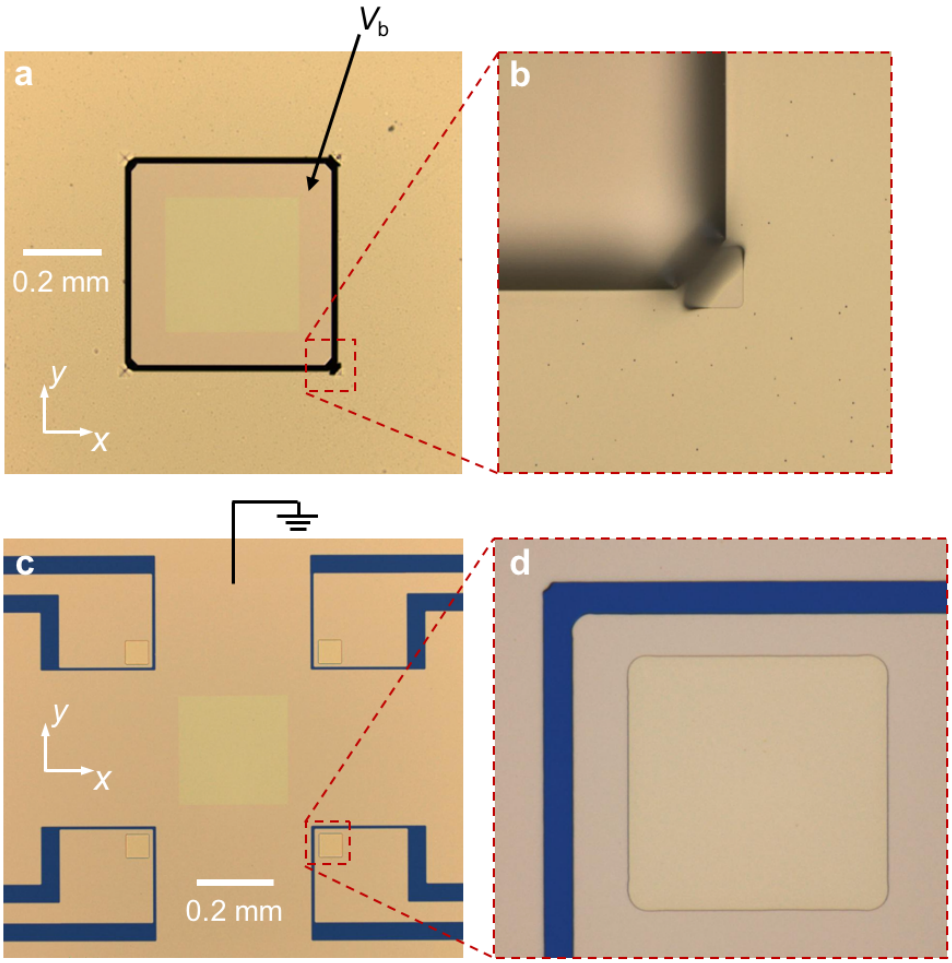

Figure 7.1.2 | Optical images of the left (**a** and **b**) and right (**c** and **d**) sample surfaces.

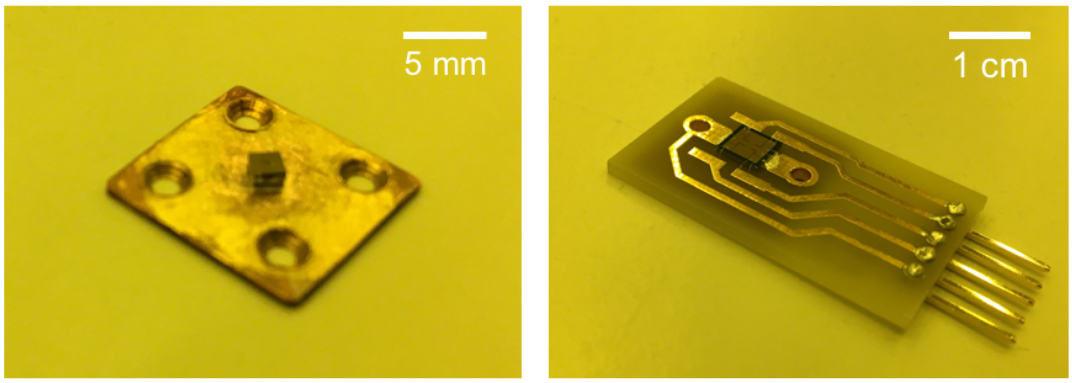

Figure 7.1.3 | Optical images showing the mounting of the two samples. The left and right samples are attached to a custom-made copper plate and a printed circuit board, respectively.

To observe the Casimir interaction between two parallel planes, high degree of parallelism between the two surfaces is crucial. So far, most of the Casimir force measurements were carried out in sphere-plane configuration because of the challenge of high precision parallel alignment. The smallest parallel-plate distance achieved in Casimir measurement is ~600 nm [82]. We overcome this challenge by implementing the mesa-spacer structure (developed previously in Ref. [99]) and employing the optical interference imaging technique. Such effort allows us to explore Casimir interaction between parallel plates with an unprecedented distance of ~300 nm.

The parallel alignment schematics is shown in Fig. 7.1.4. On the left chip, the mechanical membrane is fabricated at the center of a mesa which has a height of ~25 μm. On the right chip, four contact spacers (~150 nm in height) and electrodes are patterned at the four corners outside the membrane. The 75 nm gold film coated on both sides of the membranes block the red detection laser (633 nm) while allowing dim transmission of the blue illumination from a high brightness LED (460 nm). A bias voltage V_b is applied between the two membrane surfaces. When the two samples are brought close and touch each other at the spacer region, an electrical signal will be picked up and the signal will indicate which corner is touching. Simultaneous touching of the four corners indicate good alignment of parallelism. In the experiment, the distance at which the first corner touches and the distance at which all four corners touch are within 80 nm.

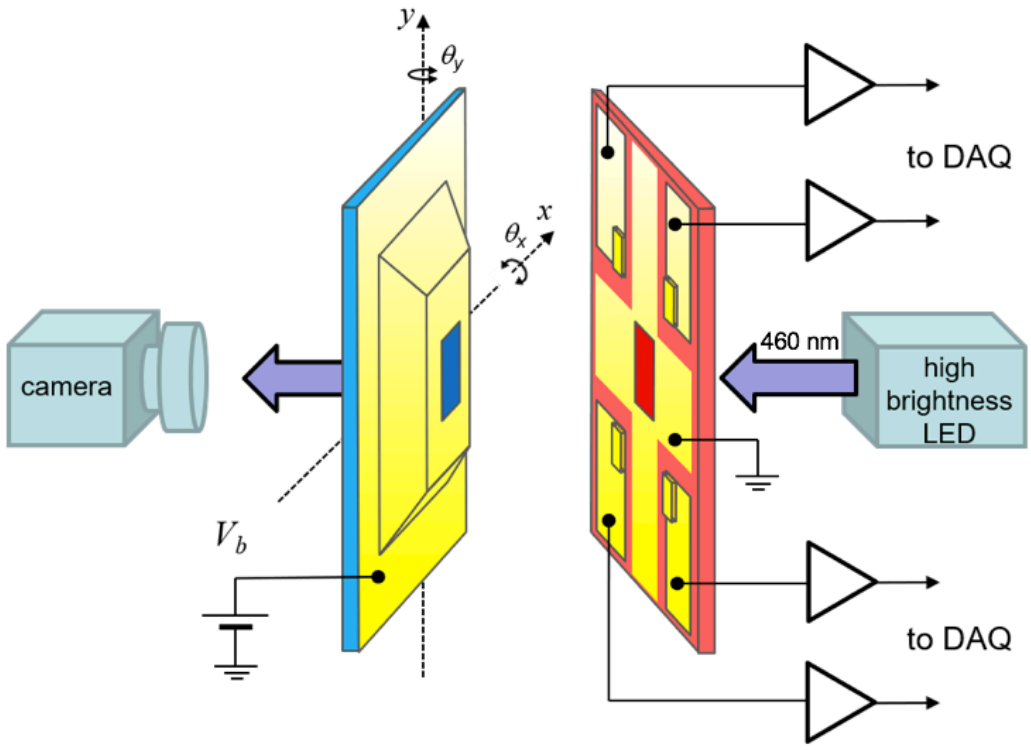

Figure 7.1.4 | Schematics of the parallel alignment setup.

Simultaneously, the parallelism between the membrane is monitored optically by examining the brightness distribution of the interference pattern, as shown in Figs. 7.1.5a and 7.1.5b. Aligned membranes show uniform optical images when varying the distance (Fig. 7.1.5a). By analyzing the optical intensity at different locations of the membrane while changing the membrane-membrane separation, we obtain the relative tilting angle of the membranes with respect to the *x* and *y* axes $\Delta\theta_x = 22 \pm 25$ μrad and $\Delta\theta_y = 43 \pm 24$ μrad (Fig. 7.1.5c). For comparison, images of the misaligned membranes are shown in Fig. 7.1.5b, which give rise to $\Delta\theta_x = 228 \pm 33$ μrad and $\Delta\theta_y = 179 \pm 39$ μrad (Fig. 7.1.5d).

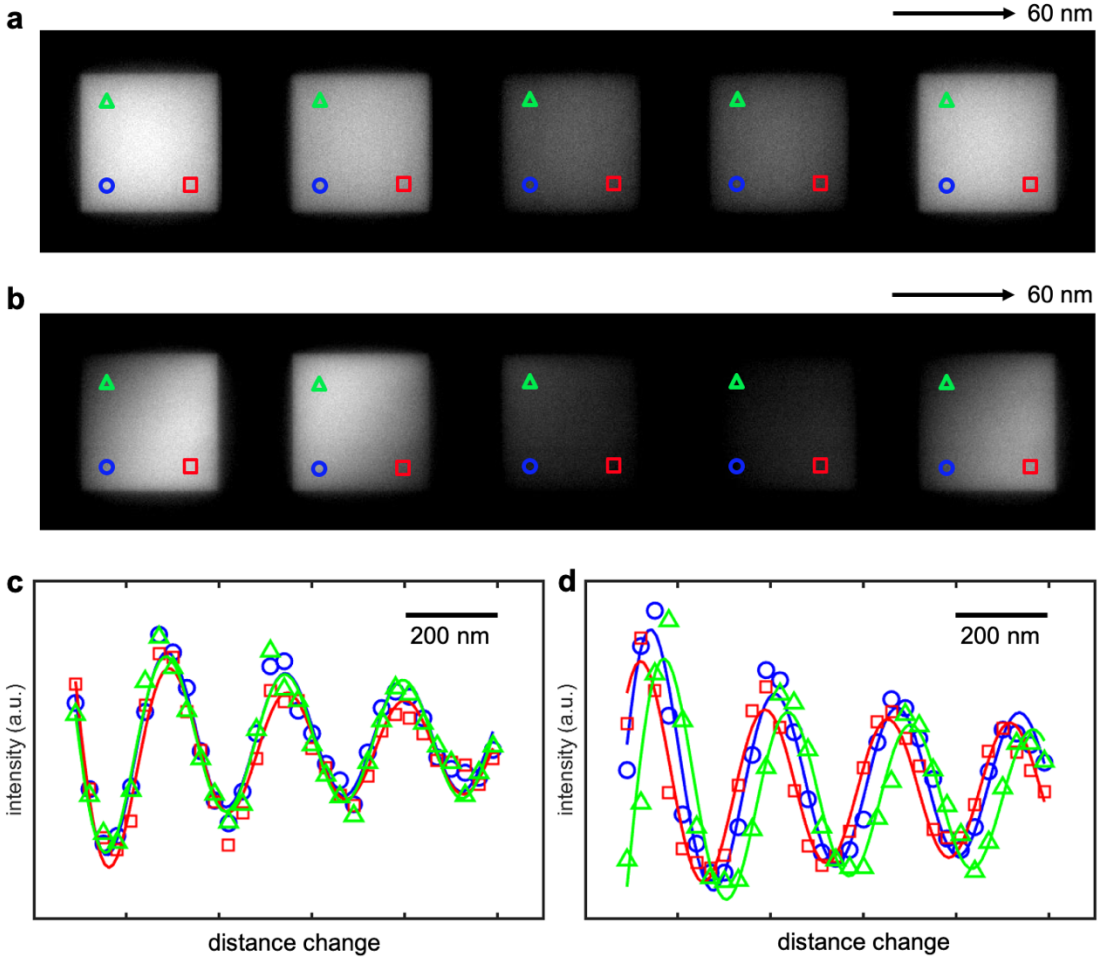

Figure 7.1.5 | **a, b,** Transmission optical images for the aligned (**a**) and misaligned (**b**) cases. **c**, **d**, Optical intensity at different locations of the membranes (markers in **a**, **b**) versus the separation change. Solid curves are sinusoidal fits with an attenuation factor. The periodicity (~230 nm) matches well with the half wavelength of the illumination (~460 nm).

7.2 Measurement setup and signal acquisition

The experimental setup is illustrated in Fig. 7.2.1. Two laser beams split from an intensity stabilized He/Ne laser (Thorlabs, HRS015B) are sent to the back sides of the membranes to interferometrically detect the thermal Brownian motion of the membrane modes. The distance between the mirrors and the membranes are controlled by piezo-actuators using the DC component of the reflected lights (monitored by photodetectors) as the feedback signal. This feedback control enables us to achieve long term stability of the detection sensitivity. The left/right samples are mounted on closed-loop TEC h cooler/heater using platinum RTD as temperature sensor. Feedback control of the bath temperatures allows stabilization and tuning of the mechanical resonances (see latter discussion). The right sample is mounted on a calibrated closed-loop piezo linear stage, which controls the relative distance between the membranes with a precision of ~5 nm.

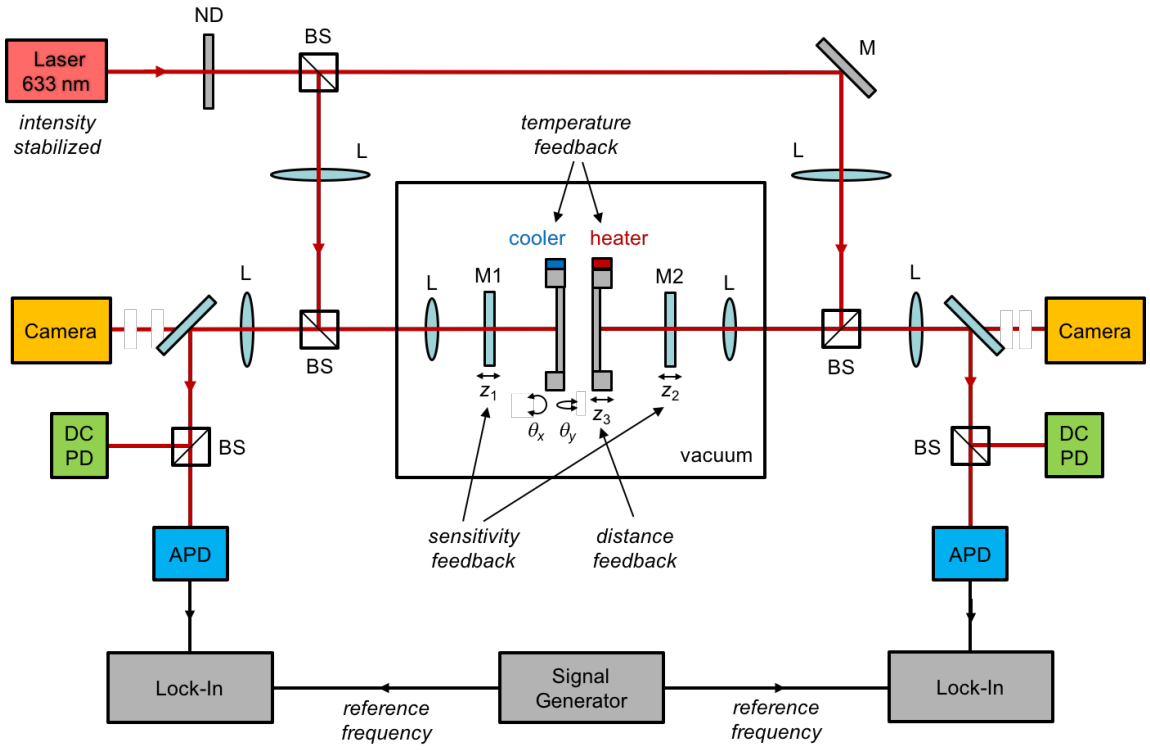

Figure 7.2.1 | Schematic of the double optical interferometry experimental setup with the integration of multiple feedback controls. (ND: neutral density filter, BS: beam splitter, M: mirror, L: lens, DC-PD: DC photodetector, APD: avalanche photodetector.)

An optical image of the sample mount assembly and the control stages is shown in Fig. 7.2.2. The left sample (with mesa structure) is attached to a custom-made copper plate using conductive silver paint. The right sample (with patterned electrodes) is mounted on a printed circuit board with the on-chip electrodes wire-bonded to the corresponding contact pads. During the measurement, the whole assembly is kept in high vacuum with a pressure below 10^{-6} Torr. To avoid excessive optical heating, laser powers are kept low at ~8 μW before entering the chamber.

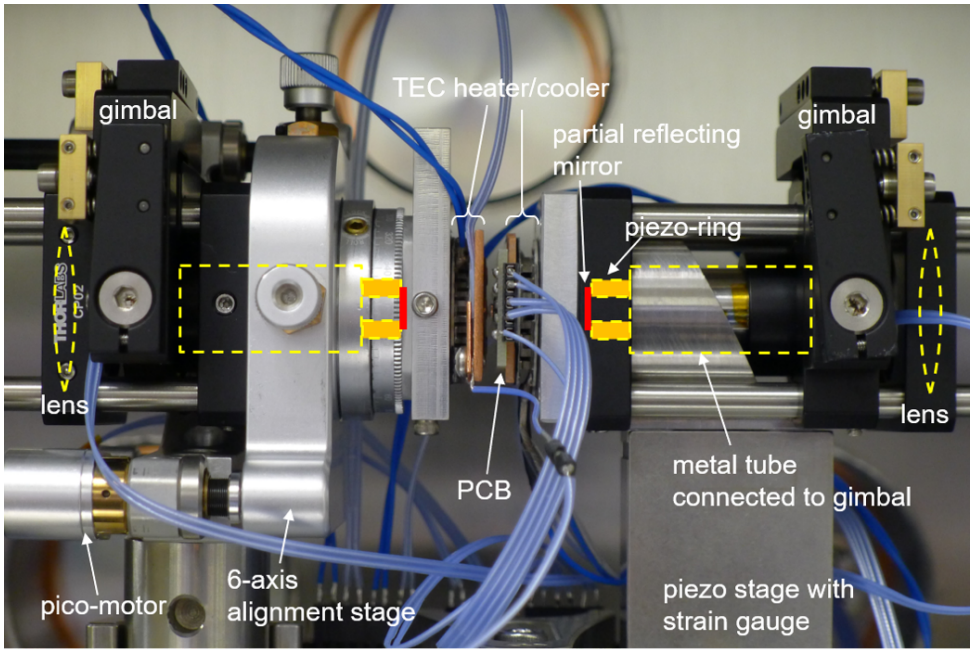

Figure 7.2.2 | Optical image of the sample mount assembly and control stages.

At room temperature (~296 K), the resonance frequencies of the phonon two modes are off by ~50 kHz because of the membrane size difference (330 × 330 μm^2 and 280 × 280 μm^2). We match the resonance frequency of the two modes by thermally tuning the stress of the membranes. At bath temperatures T_1 = 287.0 K and T_2 = 312.5 K, their resonances match at $\Omega/2\pi$ = 191.6 kHz (dashed line in Fig. 7.2.3a), with high quality factors of $Q_1 = 4.5 \times 10^4$ and $Q_2 = 2.0 \times 10^4$. Using optical interferometry, we resolve the thermal mechanical noise of the two modes with high signal-to-background ratios ~20 dB, as shown in Figs. 7.2.3b and 7.2.3c.

In the experiment, the maximum bath temperature difference and the minimum sample distance we can achieve are ~35 K and ~250 nm. These conditions set requirements on the resonance frequencies and the quality factors. Since both values can vary from sample to sample, we examined about five pairs of devices before reaching the final pair.

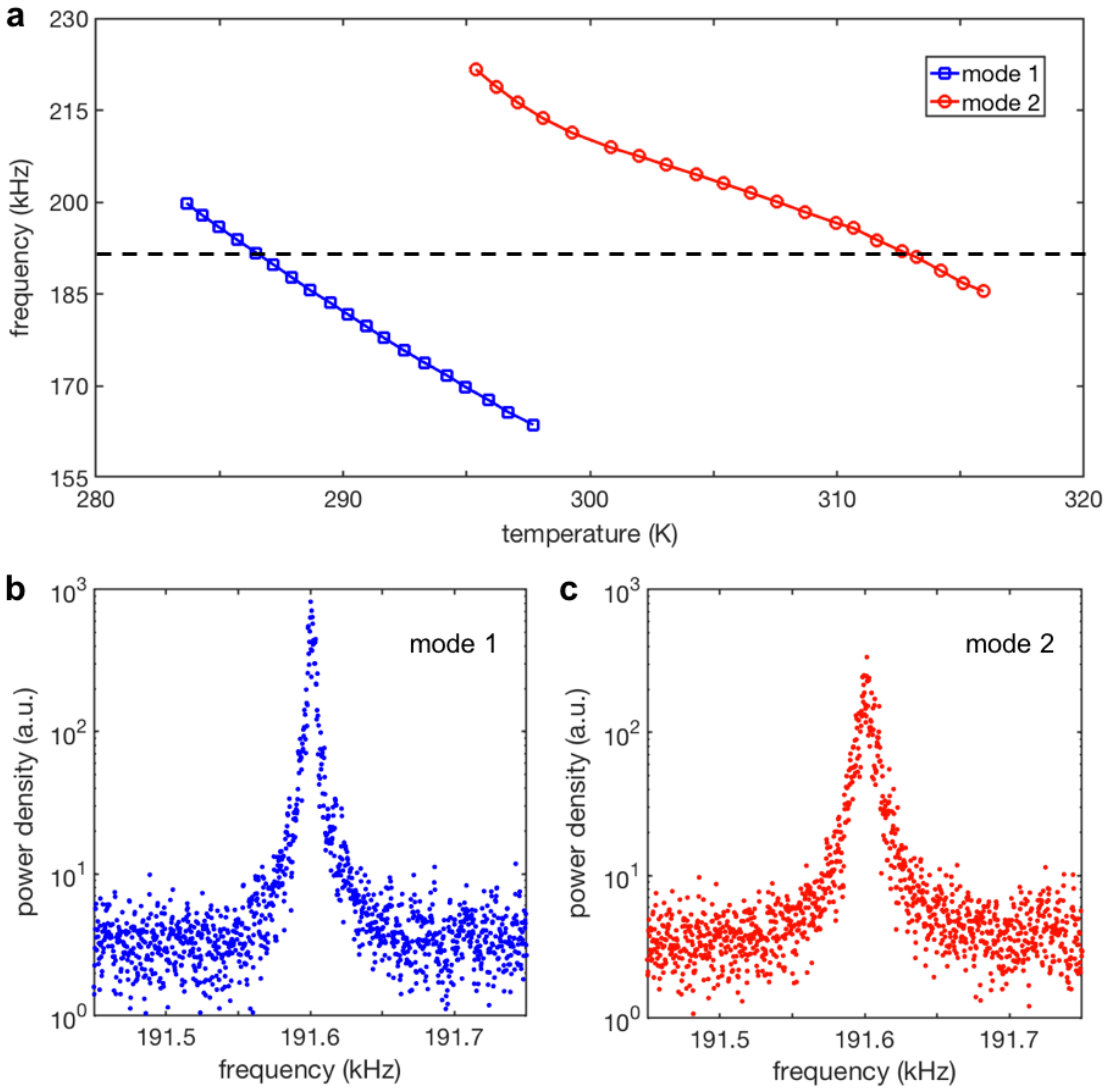

Figure 7.2.3 | **a**, Resonance frequencies of the two modes versus the bath temperatures. **b**, **c**, Thermal mechanical noise spectrum of mode 1 (**a**) and mode 2 (**b**).

Without any feedback control, the mechanical resonance frequencies typically drift at a rate of ~0.5 Hz/min. During the thermal transfer measurement, we control the bath temperatures and lock the mechanical resonance to a certain frequency. With this exquisite control, the frequency mismatch of the two phonon modes can be maintained below 2 Hz, which is well below the linewidths of the two mechanical modes (4.6 Hz and 9.6 Hz), as shown in Fig. 7.2.4. The bath temperatures were monitored during the feedback control. The fluctuations of the bath temperatures are unresolvable with the sensitivity (0.01 K) of our platinum resistance temperature detectors. Based on the fluctuations of the resonance frequencies (~2

Hz) and the measured frequency-temperature coefficient ~2 kHz/K of the membrane modes, we can estimate the fluctuation of the bath temperature to be ~0.001 K.

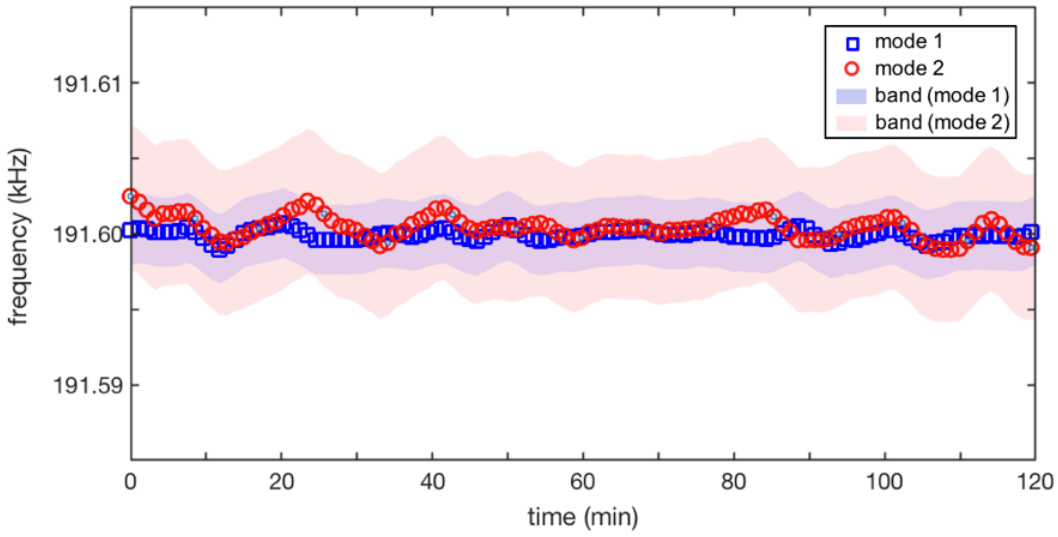

Figure 7.2.4 | Frequency stability under thermal feedback control. The shaded areas represent the bandwidths of the mechanical resonances.

7.3 Realization of the Casimir strong phonon coupling

To verify that the phonon mode coupling is originated from the Casimir force, we examine the phonon mode coupling characteristics. When the membranes are brought close, we observe an anti-crossing feature in the thermal noise spectra, as shown in Fig. 7.3.1a. This feature reveals the strong coupling of the two phonon modes. The upper and lower branch corresponds to the symmetric and antisymmetric eigenmode, respectively. The frequency splitting Δf of the two peaks is a direct indicator of the coupling strength.

Taking both Casimir and electrostatic effects into account, the observed frequency splitting can be expressed as $\Delta f = \Delta f_{Cas} + \Delta f_{Ele}$, with Δf_{Cas} ($\propto$ Casmir force gradient) and $\Delta f_{Ele} \propto [(V_b - V_0)^2 + V_{rms}^2]d^{-3}$ being the Casimir and the electrostatic component, respectively [100]. V_0 and V_{rms} represent the first and the second-moment of the surface potential difference between the two metallized membranes, which can result from oxidization, strains, impurities in the surfaces or different crystal orientation of the metal domains. The first-order electrostatic effect exhibits a unique dependence of $(V_b - V_0)^2 d^{-3}$, as shown in Fig. 7.3.1b, which provides an effective way to calibrate the absolute distance between the two nanomembranes [82,83,85], as discussed below.

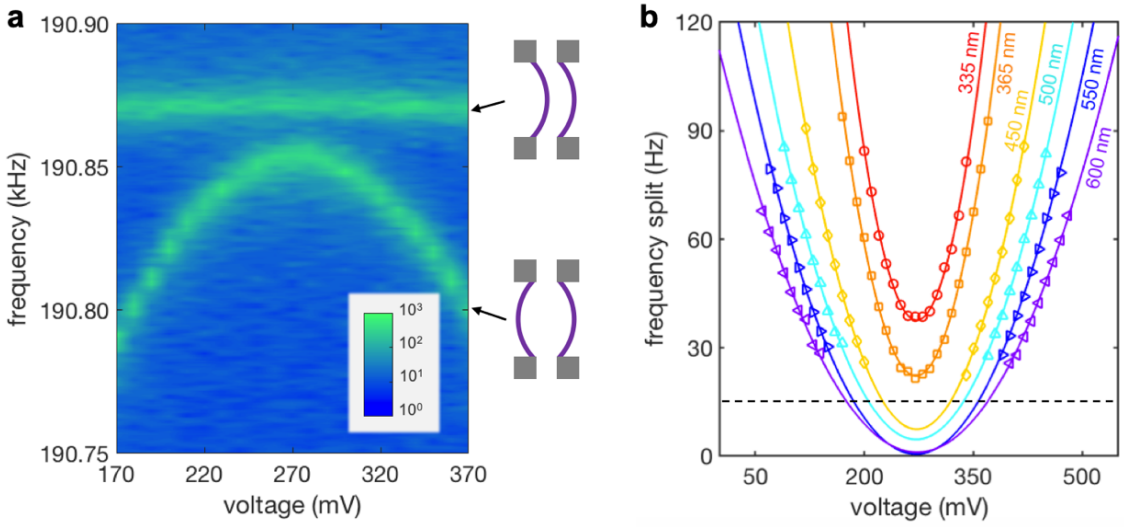

Figure 7.3.1 | **a,** Thermomechanical noise spectrum of membrane 2 at the distance d = 400 nm with different bias voltages. The upper and lower branch corresponds to the symmetric and antisymmetric eigenmode, respectively. **b,** Frequency splitting of the thermomechanical noise spectrum shows a parabolic dependence on the bias voltage between the membranes (solid curves are parabolic fits). The curvatures of the parabolas are proportional to the electrostatic interaction strength, which have a distance dependence of d^{-3} according to the Coulomb law. We determine the frequency splitting by fitting the two peak positions in the spectra, which gives a precision of ~1 Hz (smaller than the data markers).

In the experiment, the strain gauge sensor of the piezo linear stage only monitors the distance change δd between the membranes. We use the unique distance and voltage dependence of the electrostatic effect to calibrate the absolute distance between the two membranes $d = \delta d + d_0$. At each distance, the measured frequency splitting shows a parabolic dependence on the bias voltage. We fit the parabolic curvatures (electrostatic strength) with a distance power law of $(\delta d + d_0)^{-3}$ using d_0 as the fitting parameter. The results are shown in Fig. 7.3.2a. Using this method, we determine the absolute distance between the membrane with a precision of ~5 nm. From the same data, we also obtain the surface potential V_0 at each distance using the parabolic fits of the frequency splitting, as shown in Fig. 7.3.2b. The surface potential remains constant at different distances, which agrees with the theory prediction of parallel planes configuration [100]. In contrast, a distance dependence in V_0 is expected for sphere-plane configuration in other Casimir force experiments.

The bias voltage V_b is applied throughout the heat transfer measurement to compensate the surface potential V_0 at each separation. We apply the bias voltage by dividing the voltage output of a low noise source meter (Keithley 2400) by over 150 times. The noise power density of the bias voltage ($\overline{v_b^2}/\Delta f$) is <$10^{-17}$ V^2/Hz in the frequency ranges of 10-50 Hz and 182-194 kHz.

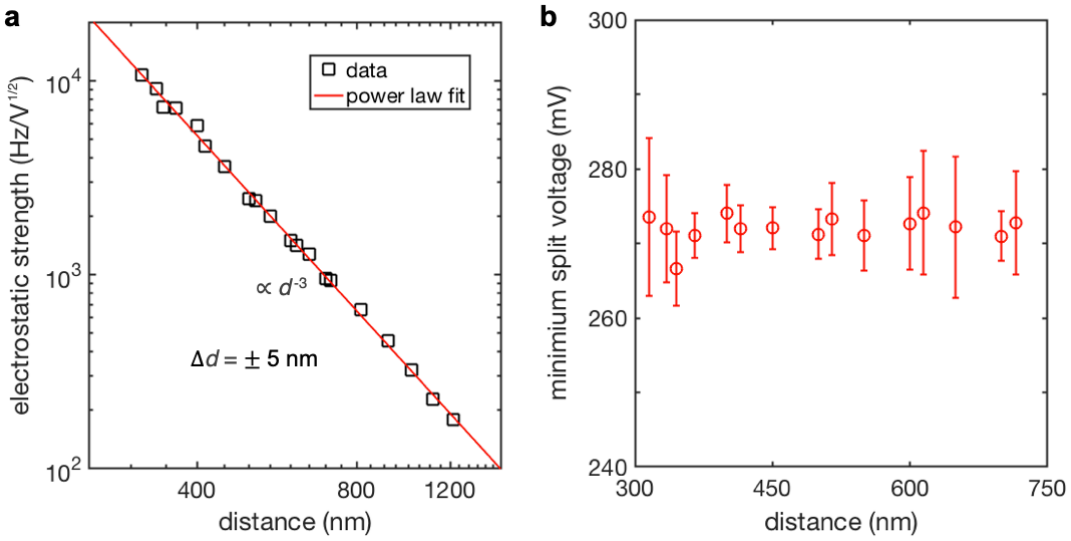

Figure 7.3.2 | Dependence of electrostatic strength (**a**) and minimum splitting voltage V_0 (**b**) on the distance between the membranes.

When V_0 is compensated by the applied bias voltage V_b, we observe that the frequency split shows a distance dependence of $d^{-4.91\pm0.12}$ (see below in Fig. 7.3.3). This verifies that the Casimir effect dominates over the electrostatic effect in our measurement. This result also represents the first demonstration of strong phonon coupling induced by the Casimir force.

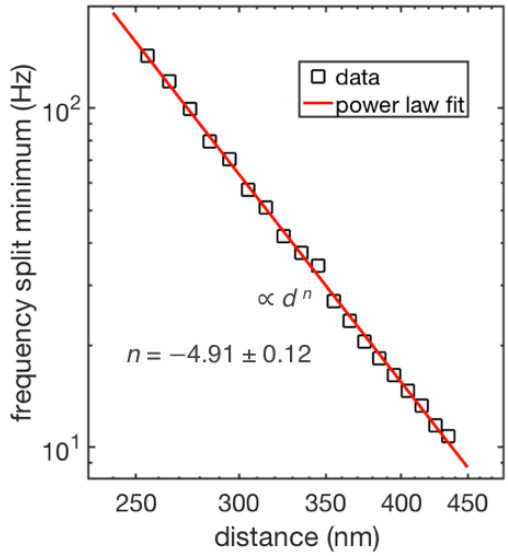

Figure 7.3.3 | The minimum frequency splitting for each distance shows a dependence of $d^{-4.91\pm0.12}$. This power law verifies that the Casimir interaction is dominant over the electrostatic interaction in our measurement.

7.4 Observation of the Casimir phonon heat transfer

We observe the heat transfer between the phonon modes of the membranes through the Casimir interaction. The mode temperatures exhibit a strong dependence on the distance, as shown in Fig, 7.4.1a. At large separation, the mode temperatures are the same as their thermal bath temperatures, while at small separation (d < 600 nm) they begin to deviate. As the distance further decreases to d < 400 nm, T_1' and T_2' become nearly identical, showing thermalization of the two phonon modes. In the measurement, the mode temperatures are determined by their thermal Brownian motions, i.e. $k_B T_i' = m_i \Omega^2 \langle z_i^2 \rangle$, where m_i is the effective mass and $\langle * \rangle$ represents the ensemble average. The mechanical motion can be decomposed into $z_i(t) = X_i(t)\cos\Omega t + Y_i(t)\sin\Omega t$, with $X_i(t)$ and $Y_i(t)$ being the two displacement quadrature components. The measured two quadrature components display circularly symmetric distribution in the phase space showing that the thermal motions are random with all phases being equally available (Figs. 7.4.1b and 7.4.1c). A plot of the probability distribution of the total energy (Fig. 7.4.1d), i.e. $E_i = m_i \Omega^2 (X_i^2 + Y_i^2)$, shows that the energy distribution follows the statistics of a canonical ensemble, i.e. $P(E_i) \propto e^{-E_i/k_B T_i'}$.

It is important to note that such a heat transfer effect is observed only when the resonance frequencies of the phonon modes are matched within the linewidth, i.e., $|\Omega_2 - \Omega_1| < \gamma_1, \gamma_2$. As a control experiment, we offset the resonance frequencies of the modes while fixing the distance between the membranes. When the frequency offset $(\Omega_2 - \Omega_1)$ is much larger than the linewidths, the mode temperatures keep the same as their bath temperatures, as shown in Fig. 7.4.2.

The observed phenomenon can be quantitatively explained by the competition between the Casimir coupling rate ($g_C \propto$ Casimir force gradient) and the mode-bath thermal exchange rate ($\gamma_i = \Omega/2Q_i$). When d decreases from 600 nm to 350 nm, g_C increases rapidly and the system evolves from weakly coupled ($g_C \ll \gamma_i$) to strongly coupled ($g_C \gg \gamma_i$), as shown before in Fig. 6.4.2. When $g_C \gg \gamma_i$, thermalization of the phonon modes occurs ($T_1' \approx T_2' \approx T_{th}'$) with the thermalized temperature determined by $T_{th}' = (T_1\gamma_1 + T_2\gamma_2)/(\gamma_1 + \gamma_2)$. At this regime, the net heat flux transferred across the two thermal baths mediated by the strongly coupled phonon modes is calculated to be $P_{2\to1} = 2k_B(T_2 - T_1)\gamma_1\gamma_2/(\gamma_1 + \gamma_2) = 6.5\times 10^{-21}$ J/s. Using the coupled-mode Langevin equations in the above Chapter, we calculate the distance dependence of the mode temperatures (solid lines in Fig. 7.4.1a), which well describes the experiment data.

In the experiment, the fluctuation of the electrostatic force would drive and thus heat up the mechanical modes. The voltage difference between the two membranes is given by $[(\overline{V_b} - V_0) + v_b(t)]$. The residual voltage $(\overline{V_b} - V_0)$ is estimated to be ~5 mV based on the precision in determining V_0 (see data in Fig. 7.3.2b). The fluctuation voltage is much smaller than the residual voltage, namely $v_b(t) \ll (\overline{V_b} - V_0)$. Under such condition, the

electrostatic force per area can be written as $\varepsilon_0(\overline{V_b} - V_0)[(\overline{V_b} - V_0) + 2v_b(t)]/2d^2$. Using the estimated noise power density of the bias voltage $(\overline{v_b^2}/\Delta f) \sim 10^{-18}$ V^2/Hz near the mechanical resonance frequency, the mode temperature rise is calculated to be less than 0.01 K when the distance is larger than 350 nm. Therefore, this electrostatic heating effect is neglectable in our experiment.

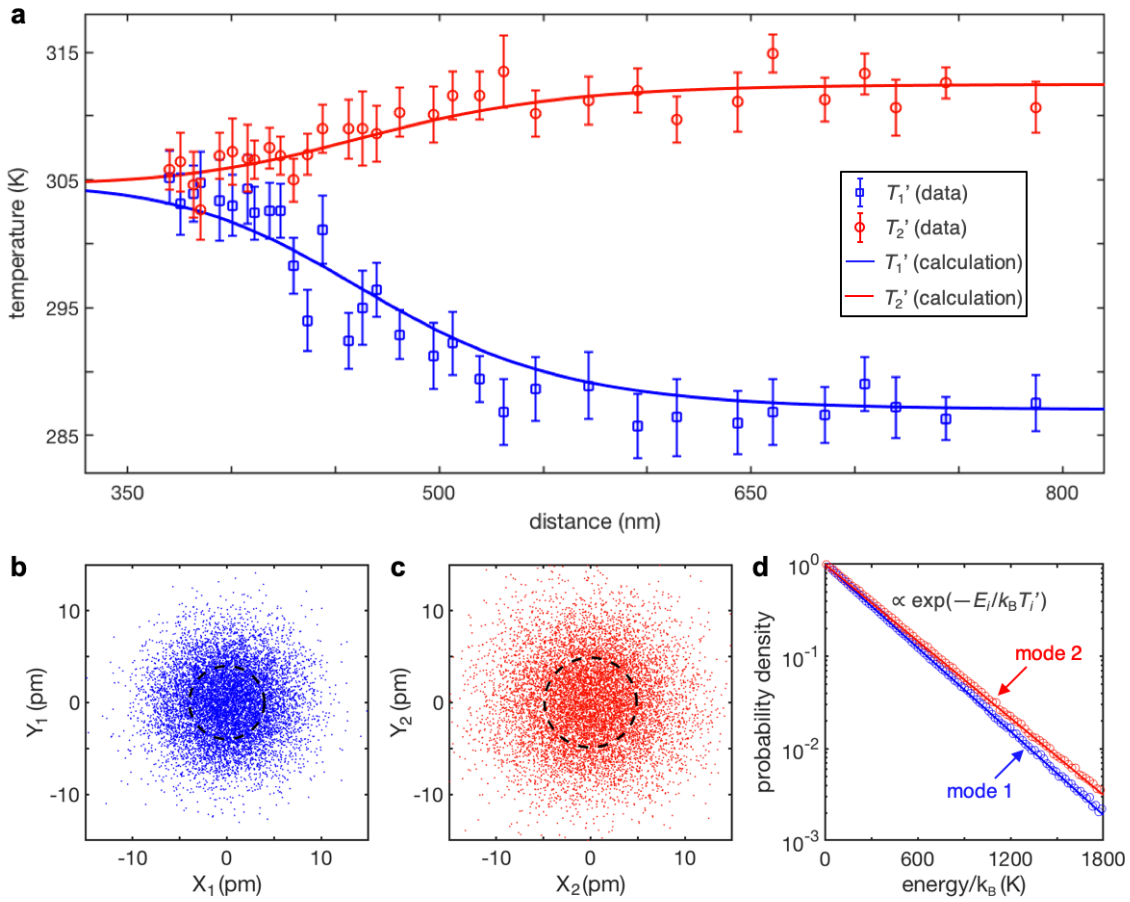

Figure 7.4.1 | **a,** Because of the Casimir interaction, the mode temperatures deviate from their bath temperatures when the two membranes are brought close. At $d < 400$ nm, T_1' and T_2' become nearly identical, showing thermalization of the two phonon modes. The mode temperatures are measured from the thermal Brownian motion $k_B T_i' = m_i \Omega^2 \langle z_i^2 \rangle$. The error bars represent the standard error determined by ~4 hours' continuous measurement. The data agrees well with the calculation using coupled-mode Langevin equations (solid lines). **b, c,** The measured quadrature components of the thermal displacement of phonon modes 1 (**b**) and 2 (**c**) at mode temperatures $T_1' = 287.0$ K and $T_2' = 312.5$ K, respectively. Dashed lines indicate the standard deviations of the distriubtions and the enclosed areas are proportional to the mode temperatures. **d,** Probability distributions of the phonon mode energy follow the statistics of a canonical ensemble $P(E_i) \propto e^{-E_i/k_B T_i'}$ represented by the solid lines.

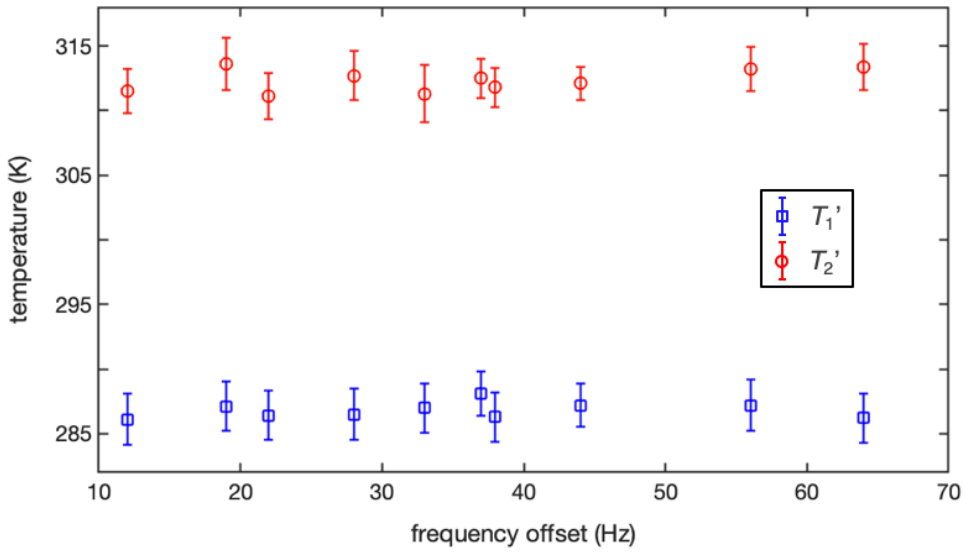

Figure 7.4.2 | When the frequency offset $(\Omega_2 - \Omega_1)$ is much larger than the linewidths of the modes, the mode temperatures T_1' and T_2' keep the same as their bath temperatures and no heat transfer effect is observed. Here, the distance between the membrane is d = 430 nm.

7.5 Analysis of thermal radiation effects

In this section, we distinguish the observed heat transfer from thermal radiation effects.

In the experiment, the bath temperatures are measured by platinum resistance temperature sensors attached to the sample holders. When the two membranes are brought close, near-field thermal radiation could induce a deviation of the local temperatures on the membrane surface, resulting a difference between the actual the measured bath temperatures. Above 300 nm separation, radiation heat transfer coefficient between gold surfaces has been measured to be <1.4 W/m^{2}K [101]. Using thermal conductivity of gold (~150 W/mK at 75 nm [102]) and silicon nitride (~10 W/mK [103]) thin films, the local temperature deviation is estimated to be <0.02 K, which is over two orders of magnitude smaller than the mode temperature change we observed (see Fig. 7.4.1).

The local temperature change due to thermal radiation also modifies the membrane stress and therefore induces a frequency shift down (up) of the mechanical mode 1 (2) when the membranes are close. Unlike the Casimir phonon coupling, this thermal radiation effect does not depend on the frequency matching of the two modes. To observe this effect, we offset the frequencies of the two modes by ~250 Hz and fix the output of the heater and cooler. The measured frequency shifts are shown in Fig. 7.5.1a. We note here that the observed

frequency shifts also include the contribution from the Casimir force, which is given by $-F'_{Cas}(d)/2\Omega\rho$. Excluding the Casimir force contribution, the frequency shifts are <40 Hz when d > 300 nm, as shown in Fig. 7.5.1b. Based on the measured frequency-temperature coefficient ~2 kHz/K of the membrane modes (see Fig. 7.2.3), these frequency shifts correspond to temperature changes of <0.02 K, which agrees well with our calculation.

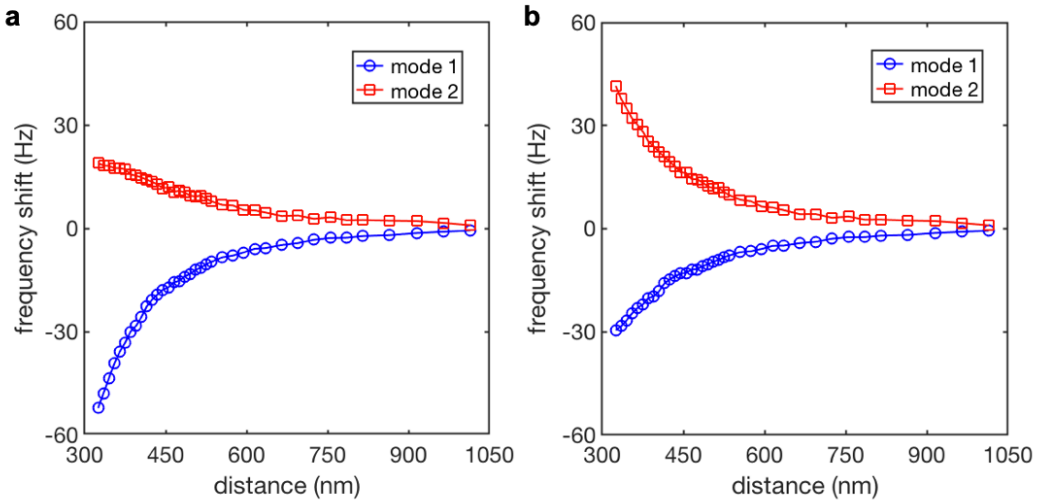

Figure 7.5.1 | | Frequency shifts of the two modes versus the distance (**a**). In (**b**), the Casimir force contribution is excluded. Measurement is performed at bath temperatures T_1 = 287.0 K and T_2 = 312.5 K, and the frequencies of the modes are offset by ~250 Hz.

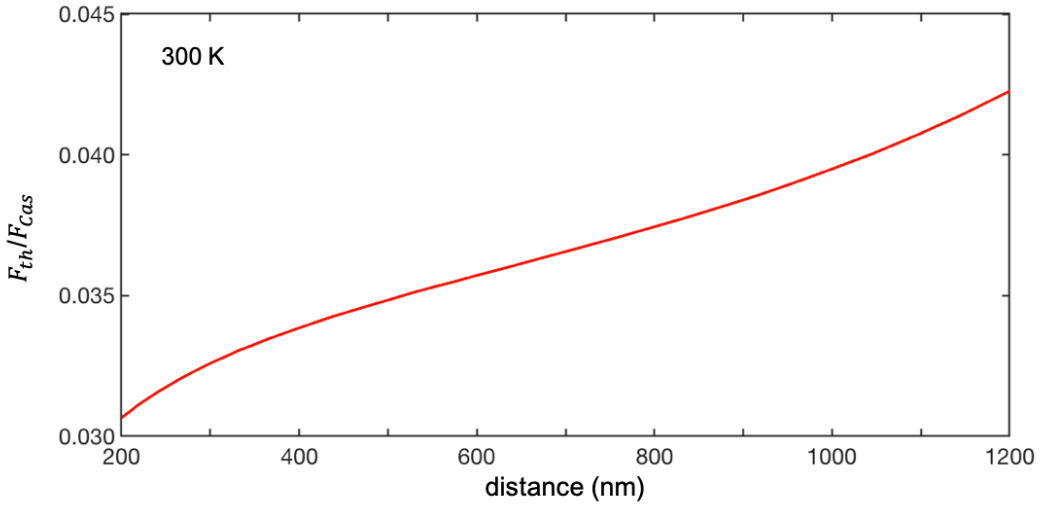

Figure 7.5.2 | | Distance dependence of the ratio between the radiation pressure driven by thermal fluctuations and the Casimir pressure driven by quantum fluctuations.

Thermal fluctuations of electromagnetic fields can also induce a pressure $F_{th}(d,T)$ on the membranes. In the Casimir force community, this pressure is interpreted as the thermal Casimir pressure [104], which can be calculated with the Lifshitz formula [78]. In our experimental condition (d < 800 nm), the thermal radiation pressure (at 300 K) is calculated to be less than 4% of the Casimir pressure driven by quantum fluctuations, as shown in Fig. 7.5.2, and therefore its effects are negligible.

7.6 Conclusion and outlook

In conclusion, we have experimentally demonstrated phonon thermal transfer induced by quantum vacuum fluctuations of electromagnetic fields using nanomechanical devices. Our observation is unambiguously distinct from other effects including electrostatic interaction and near-field thermal radiation**.** As the first demonstration of the principle, we focus on heat transfer between single phonon modes. When the majority of phonon modes in solid take part in the thermal exchange process, the effect generalizes to heat transfer between two bulk solids [11,105].

The ability of controlling thermal energy flow with quantum vacuum opens up a new arena to study quantum thermodynamics [106,107] and to implement quantum thermal machines [108]. Moreover, our method for achieving and controlling the strong Casimir phonon coupling provides a versatile platform to implement coherent phonon process (e.g. phonon state transfer and entanglement) using quantum vacuum. In particularly, when the frequency of the phonon oscillation is comparable to the electromagnetic mode frequency, the dynamic Casimir effect would emerge and influence the phonon coupling and energy transfer process [95]. This intriguing condition can be achieved in a microwave optical cavity with movable boundaries which can oscillate at high frequencies (in the gigahertz range).

Remark: Chapter 6 and Chapter 7 include materials from K. Y. Fong*, H.-K. Li*, et al. “Phonon thermal transfer induced by quantum vacuum fluctuations.” (under review) (*contributed equally).

Bibliography

1. L. D. Landau and E. Lifshitz. *Statistical Physics*. Vol. 5. (Elsevier, New York, 2013)

2. P. W. Anderson. *Basic Notions of Condensed Matter Physics*. 2nd ed. (Westview, Boulder, CO, 1997).

3. I. Bloch, J. Dalibard, and W. Zwerger. Many-body physics with ultracold gases. *Rev. Mod. Phys.* 80, 885 (2008).

4. H.-K Li, E. Urban, C. Noel, A. Chuang, Y. Xia, A. Ransford, B. Hemmerling, Y. Wang, T. Li, H. Haeffner, and X. Zhang. Realization of translational symmetry in trapped cold ion rings. *Phys. Rev. Lett.* 118, 053001 (2017).

5. H. G. Craighead. Nanoelectromechanical Systems. *Science* 290, 1532 (2000).

6. M. Roukes. Nanoelectromechanical systems face the future. *Phys. World* 14, 25 (2001).

7. L. Midolo, A. Schliesser, and A. Fiore. Nano-opto-electro-mechanical systems. *Nature Nanotechnol.* 13, 11 (2018).

8. X. Xu, W. Yao, D. Xiao, and T. F. Heinz. Spin and pseudospins in layered transition metal dichalcogenides. *Nature Phys.* 10, 343 (2014).

9. K. F. Mak, D. Xiao, and J. Shan, Light–valley interactions in 2D semiconductors. *Nature Photon.* 12, 451 (2018).

10. H.-K. Li, K. Y. Fong, H. Zhu, Q. Li, S. Wang, S. Yang, Y. Wang, and X. Zhang. Valley optomechanics in a monolayer semiconductor. *Nature Photon.* (in press).

11. J. B. Pendry, K. Sasihithlu, and R. V. Craster. Phonon-assisted heat transfer between vacuum-separated surfaces. *Phys. Rev. B* 94, 075414 (2016).

12. Y. Ezzahri and K. Joulain. Vacuum-induced phonon transfer between two solid dielectric materials: Illustrating the case of Casimir force coupling. *Phys. Rev. B* 90, 115433 (2014).

13. B. V. Budaev and D. B. Bogy. On the role of acoustic waves (phonons) in equilibrium heat transfer exchange across a vacuum gap. *App. Phys. Lett.* 99, 053109 (2011).

14. K. Y. Fong, H.-K. Li, R. Zhao, S. Yang, Y. Wang, X. Zhang. Phonon thermal transfer induced by quantum vacuum fluctuations. (under review).

15. J. D. Jackson. *Classical electrodynamics*. John Wiley & Sons (2007).

16. W. Paul. Electromagnetic traps for charged and neutral particles. *Rev. Mod. Phys*. 62, 531 (1990).

17. L. S. Brown and G. Gabrielse. Geonium theory: Physics of a single electron or ion in a Penning trap. *Rev. Mod. Phys.* 58, 233 (1986).

18. D. Leibfried, R. Blatt, C. Monroe, and D. Wineland. Quantum dynamics of single trapped ions. *Rev. Mod. Phys.* 75, 281 (2003).

19. B. Horstmann, B. Reznik, S. Fagnocchi, and J. I. Cirac. Hawking radiation from an acoustic black hole on an ion ring. *Phys. Rev. Lett.* 104, 250403 (2010).

20. E. Shimshoni, G. Morigi, and S. Fishman. Quantum zigzag transition in ion chains. *Phys. Rev. Lett.* 106, 010401 (2011).

21. H. Landa, S. Marcovitch, A. Retzker, M. B. Plenio, and B. Reznik. Quantum coherence of discrete kink solitons in ion traps. *Phys. Rev. Lett.* 104, 043004 (2010).

22. H. Landa, A. Retzker, T. Schaetz, and B. Reznik. Entanglement generation using discrete solitons in coulomb crystals. *Phys. Rev. Lett.* 113, 053001 (2014).

23. T. Li, Z.-X. Gong, Z.-Q. Yin, H. T. Quan, X. Yin, P. Zhang, L.-M. Duan, and X. Zhang. Space-time crystals of trapped ions. *Phys. Rev. Lett.* 109, 163001 (2012).

24. C. Champenois, M. Marciante, J. Pedregosa-Gutierrez, M. Houssin, M. Knoop, and M. Kajita. Ion ring in a linear multipole trap for optical frequency metrology. *Phys. Rev. A* 81, 043410 (2010).

25. G.-D. Lin, S.-L. Zhu, R. Islam, K. Kim, M.-S. Chang, S. Korenblit, C. Monroe, and L.-M. Duan. Large-scale quantum computation in an anharmonic linear ion trap. *Europhys. Lett.* 86, 60004 (2009).

26. I. Waki, S. Kassner, G. Birkl, and H. Walther. Observation of ordered structures of laser-cooled ions in a quadrupole storage ring. *Phys. Rev. Lett.* 68, 2007 (1992).

27. G. Birkl, S. Kassner, and H. Walther. Multiple-shell structures of laser-cooled $^{24}Mg^{+}$ ions in a quadrupole storage ring. *Nature* 357, 310 (1992).

28. T. Schätz, U. Schramm, and D. Habs. Crystalline ion beams. *Nature* 412, 717 (2001).

29. B. Tabakov, F. Benito, M. Blain, C. R. Clark, S. Clark, R. A. Haltli, P. Maunz, J. D. Sterk, C. Tigges, and D. Stick. Assembling a ring-shaped crystal in a microfabricated surface ion trap. *Phys. Rev. Applied* 4, 031001 (2015).

30. C. Monroe and J. Kim. Scaling the ion trap quantum processor. *Science* 339, 1164 (2013).

31. G. Littich. Electrostatic control and transport of ions on a planar trap for quantum information processing. MA thesis. ETH Zurich, 2011.

32. R. J. Clark. Ideal multipole ion traps from planar ring electrodes. *Appl. Phys. B* 113, 171 (2013).

33. P.-J. Wang, T. Li, C. Noel, A. Chuang, X. Zhang, and H. Häffner. Surface traps for freely rotating ion ring crystals. *J. Phys. B* 48, 205002 (2015).

34. E. Urban. Implementation of a rotationally symmetric ring ion trap and coherent control of rotational states. PhD thesis. University of California, Berkeley.

35. A. Kreuter, C. Becher, G. P. T. Lancaster, A. B. Mundt, C. Russo, H. Häffner, C. Roos, W. Hänsel, F. Schmidt-Kaler, R. Blatt, and M. S. Safronova. Experimental and theoretical study of the $3d^2D$–level lifetimes of $^{40}Ca^+$. Phys. Rev. A 71, 032504 (2005).

36. R. K. Joshi, P. Carbone, F. C. Wang, V. G. Kravets, Y. Su, I. V. Grigorieva, H. A. Wu, A. K. Geim, and R. R. Nair. Precise and ultrafast molecular sieving through graphene oxide membranes. *Science* 343, 752 (2014).

37. L. Chen, G. Shi, J. Shen, B. Peng, B. Zhang, Y. Wang, F. Bian, J. Wang, D. Li, Z. Qian, and G. Xu. Ion sieving in graphene oxide membranes via cationic control of interlayer spacing. *Nature* 550, 380 (2017).

38. A. Rycerz, J. Tworzydło, and C. W. J. Beenakker. Valley filter and valley valve in graphene. *Nature Phys.* 3, 172 (2007).

39. D. Culcer, A. L. Saraiva, B. Koiller, X. Hu, and S. D. Sarma. Valley-Based Noise-Resistant Quantum Computation Using Si Quantum Dots. *Phys. Rev. Lett.* 108, 126804 (2012).

40. D. Xiao, G.-B. Liu, W. Feng, X. Xu, and W. Yao. Coupled spin and valley physics in monolayers of MoS_2 and other group-VI dichalcogenides. *Phys. Rev. Lett.* 108, 196802 (2012).

41. H. Zeng, J. Dai, W. Yao, D. Xiao, and X. Cui. Valley polarization in MoS_2 monolayers by optical pumping. *Nature Nanotechnol.* 7, 490 (2012).

42. K. F. Mak, K. He, J. Shan, and T. F. Heinz. Control of valley polarization in monolayer MoS_2 by optical helicity. *Nature Nanotechnol.* 7, 494 (2012).

43. K. F. Mak, K. L. McGill, J. Park, and P. L. McEuen. The valley Hall effect in MoS_2 transistors. *Science* 344, 1489 (2014).

44. Z. Ye, D. Sun, and T. F. Heinz. Optical manipulation of valley pseudospin. *Nature Phys.* 13, 26 (2017).

45. G. Aivazian, Z. Gong, A. M. Jones, R.-L. Chu, J. Yan, D. G. Mandrus, C. Zhang, D. Cobden, W. Yao, and X. Xu. Magnetic control of valley pseudospin in monolayer WSe_2. *Nature Phys.* 11, 148 (2015).

46. A. Srivastava, M. Sidler, A. V. Allain, D. S. Lembke, A. Kis, and A. Imamoğlu. Valley Zeeman effect in elementary optical excitations of monolayer WSe_2. *Nature Phys.* 11, 141 (2015).

47. Y. Ye, J. Xiao, H. Wang, Z. Ye, H. Zhu, M. Zhao, Y. Wang, J. Zhao, X. Yin, and X. Zhang. Electrical generation and control of the valley carriers in a monolayer transition metal dichalcogenide. *Nature Nanotechnol.* 11, 598 (2016).

48. J. Lee, Z. Wang, H. Xie, K. F. Mak, and J. Shan. Valley magnetoelectricity in single-layer MoS_2. *Nature Mat.* 16, 887 (2017).

49. G. M. Rebeiz. *RF MEMS: Theory, Design, and Technology*. John Wiley and Sons (2004).

50. G. T. A. Kovacs. *Micromachined transducers sourcebook*, WCB/McGraw-Hill, Boston (1998).

51. A. D. O'Connell, M. Hofheinz, M. Ansmann, R. C. Bialczak, M. Lenander, E. Lucero, M. Neeley, D. Sank, H. Wang, M. Weides, J. Wenner, J. M. Martinis, and A. N. Cleland. Quantum ground state and single-phonon control of a mechanical resonator. *Nature* 464, 697 (2010).

52. T. A. Palomaki, J. W. Harlow, J. D. Teufel, R. W. Simmonds, and K. W. Lehnert. Coherent state transfer between itinerant microwave fields and a mechanical oscillator. *Nature* 495, 210 (2013).

53. Y. Chu, P. Kharel, W. H. Renninger, L. D. Burkhart, L. Frunzio, P. T. Rakich, R. J. Schoelkopf. Quantum acoustics with superconducting qubits. *Science* 358, 199 (2017).

54. J. S. Bunch, A. M. van der Zande, S. S. Verbridge, I. W. Frank, D. M. Tanenbaum, J. M. Parpia, H. G. Craighead, and P. L. McEuen. Electromechanical Resonators from Graphene Sheets. *Science* 315, 490 (2007).

55. C. Chen, S. Rosenblatt, K. I. Bolotin, W. Kalb, P. Kim, I. Kymissis, H. L. Stormer, T. F. Heinz, J. Hone. Performance of monolayer graphene nanomechanical resonators with electrical readout. *Nature Nanotechnol.* 4, 861 (2009).

56. A. Castellanos-Gomez, R. van Leeuwen, M. Buscema, H. S. J. van der Zant, G. A. Steele, and W. J. Venstra, Single-Layer MoS_2 Mechanical Resonators. *Adv. Mater.* 25, 6719 (2013).

57. C. Lee, X. Wei, J. W. Kysar, and J. Hone. Measurement of the elastic properties and intrinsic strength of monolayer graphene. *Science* 321, 385 (2008).

58. N. Morell, A. Reserbat-Plantey, I. Tsioutsios, K. G. Schädler, F. Dubin, F. H. L. Koppens, and A. Bachtold. High Quality Factor Mechanical Resonators Based on WSe_2 Monolayers. *Nano Lett.* 16, 5102 (2016).

59. K. Jensen, K. Kim, and A. Zettl. An atomic-resolution nanomechanical mass sensor. *Nature Nanotechnol.* 3, 533 (2008).

60. A. Castellanos-Gomez, M. Buscema, R. Molenaar, V. Singh, L. Janssen, H. S. J. van der Zant, and G. A. Steele. Deterministic transfer of two-dimensional materials by all-dry viscoelastic stamping. *2D Materials* 1, 011002 (2014).

61. H. Zhu, Y. Wang, J. Xiao, M. Liu, S. Xiong, Z. J. Wong, Z. Ye, Y. Ye, X. Yin, and X. Zhang. Observation of piezoelectricity in free-standing monolayer MoS_2. *Nature Nanotechnol.* 10, 151 (2015).

62. J. J. Bae, H. Y. Jeong, G. H. Han, J. Kim, H. Kim, M. S. Kim, B. H. Moon, S. C. Lim, and Y. H. Lee. The thickness-dependent in-plane thermal conductivity of suspended MoS_2 grown by chemical vapor deposition. *Nanoscale* 9, 2541 (2017).

63. R. Yan, J. R. Simpson, S. Bertolazzi, J. Brivio, M. Watson, X. Wu, A. Kis, T. Luo, A. R. H. Walker, and H. G. Xing. Thermal Conductivity of Monolayer Molybdenum Disulfide Obtained from Temperature-Dependent Raman Spectroscopy. *ACS Nano* 8, 986 (2014).

64. X. Wei, Y. Wang, Y. Shen, G. Xie, H. Xiao, J. Zhong, and G. Zhang. Phonon thermal conductivity of monolayer MoS_2: A comparison with single layer graphene. *Appl. Phys. Lett.* 105, 103902 (2014).

65. K. F. Mak, K. He, C. Lee, G. H. Lee, J. Hone, T. F. Heinz, and J. Shan. Tightly bound trions in monolayer MoS_2. *Nature Mat.* 12, 207 (2013).

66. Z. Wang and P. X.-L. Feng. Interferometric Motion Detection in Atomic Layer 2D Nanostructures: Visualizing Signal Transduction Efficiency and Optimization Pathways. *Sci. Rep.* 6, 28923 (2016).

67. D. Lagarde, L. Bouet, X. Marie, C. R. Zhu, B. L. Liu, T. Amand, P. H. Tan, and B. Urbaszek. Carrier and Polarization Dynamics in Monolayer MoS_2. *Phys. Rev. Lett.* 112, 047401 (2014).

68. L. Yang, N. A. Sinitsyn, W. Chen, J. Yuan, J. Zhang, J. Lou, and S. A. Crooker. Long-lived nanosecond spin relaxation and spin coherence of electrons in monolayer MoS_2 and WS_2. *Nature Phys.* 11, 830 (2015).

69. G. Plechinger, P. Nagler, A. Arora, R. Schmidt, A. Chernikov, J. Lupton, R. Bratschitsch, C. Schuller, and T. Korn. Valley dynamics of excitons in monolayer dichalcogenides. *Phys. Status Solidi RRL* 11, 1700131 (2017).

70. B. R. Carvalho, Y. Wang, S. Mignuzzi, D. Roy, M. Terrones, C. Fantini, V. H. Crespi, L. M. Malard, and M. A. Pimenta. Intervalley scattering by acoustic phonons in two-dimensional MoS_2 revealed by double-resonance Raman spectroscopy. *Nature Commun.* 8, 14670 (2017).

71. A. V. Stier, K. M. McCreary, B. T. Jonker, J. Kono, and S. A. Crooker. Exciton diamagnetic shifts and valley Zeeman effects in monolayer WS_2 and MoS_2 to 65 Tesla. *Nature Commun.* 7, 10643 (2016).

72. Y. Tao, A. Eichler, T. Holzherr, and C. L. Degen. Ultrasensitive mechanical detection of magnetic moment using a commercial disk drive write head. *Nature Commun.* 7, 12714 (2016).

73. J. Kim, C. Jin, B. Chen, H. Cai, T. Zhao, P. Lee, S. Kahn, K. Watanabe, T. Taniguchi, S. Tongay, M. F. Crommie, and F. Wang. Observation of ultralong valley lifetime in WSe_2/MoS_2 heterostructures. *Sci. Adv.* 3, e1700518 (2017).

74. M. O. Scully and M. S. Zubairy. *Quantum Optics* (Cambridge Univ. Press, 1997).

75. W. E. Lamb Jr. and R. C. Retherford. Fine Structure of the Hydrogen Atom by a Microwave Method. *Phys. Rev.* 72, 241 (1947).

76. S. W. Hawking. Particle Creation by Black Holes. *Commun. math. Phys.* 43, 199 (1975).

77. H. B. G. Casimir. On the attraction between two perfectly conducting plates. *Proc. K. Ned. Akad. Wet. B* 51, 793 (1948).

78. G. L. Klimchitskaya. U. Mohideen, and V. M. Mostepanenko. The Casimir force between real materials: experiment and theory. *Rev. Mod. Phys.* 81, 1827 (2009).

79. A. W. Rodriguez, F. Capasso, and S. G. Johnson. The Casimir effect in microstructured geometries. *Nat. Photon.* 5, 211 (2011).

80. S. K. Lamoreaux. Demonstration of the Casimir force in the 0.6 to 6 μm range. *Phys. Rev. Lett.* 78, 5 (1997).

81. U. Mohideen and A. Roy. Precision measurement of the Casimir force from 0.1 to 0.9 μ m. *Phys. Rev. Lett.* 81, 4549 (1998).

82. H. B. Chan, V. A. Aksyuk, R. N. Kleiman, D. J. Bishop, and F. Capasso. Quantum mechanical actuation of microelectromechanical systems by the Casimir force. *Science* 291, 1941 (2001).

83. G. Bressi, G. Carugno, R. Onofrio, and G. Ruoso. Measurement of the Casimir force between parallel metallic surfaces. *Phys. Rev. Lett.* 88, 041804 (2002).

84. J. N. Munday, F. Capasso, and V. A. Parsegian. Measured long-range repulsive Casimir–Lifshitz forces. *Nature* 457, 170–173 (2009).

85. D. Garcia-Sanchez, K. Y. Fong, H. Bhaskaran, S. Lamoreaux, and H. X. Tang. Casimir force and in situ surface potential measurements on nanomembranes. *Phys. Rev. Lett.* 109, 027202 (2012).

86. L. Tang, M. Wang, C. Y. Ng, M. Nikolic, C. T. Chan, A. W. Rodriguez, and H. B. Chan. Measurement of non-monotonic Casimir forces between silicon nanostructures. *Nat. Photon.* 11, 97 (2017).

87. D. A. Somers, J. L. Garrett, K. J. Palm, and J. N. Munday. Measurement of the Casimir torque. *Nature* 564, 386 (2018).

88. I. Altfeder, A. A. Voevodin, and A. K. Roy. Vacuum Phonon Tunneling. *Phys. Rev. Lett.* 105, 166101 (2010).

89. S. Xiong, K. Yang, Y. A. Kosevich, Y. Chalopin, R. D'Agosta, P. Cortona, and S. Volz. Classical to quantum transition of heat transfer between two silica clusters. *Phys. Rev. Lett.* 112, 114301 (2014).

90. M. Prunnila and J. Meltaus. Acoustic phonon tunneling and heat transport due to evanescent electric fields. *Phys. Rev. Lett.* 105, 125501 (2010).

91. S. Shen, A. Narayanaswamy, and G. Chen. Surface Phonon Polaritons Mediated Energy Transfer between Nanoscale Gaps. *Nano Lett.* 9, 2909 (2009).

92. T. L. Bergman, F. P. Incropera, D. P. DeWitt, and A. S. Lavine. *Fundamentals of heat and mass transfer*. John Wiley & Sons (2011).

93. L. H. Ford and A. Vilenkin. Quantum radiation by moving mirrors. *Phys. Rev. D* 25, 2569 (1982).

94. C. M. Wilson, G. Johansson, A. Pourkabirian, M. Simoen, J. R. Johansson, T. Duty, F. Nori and P. Delsing. Observation of the dynamical Casimir effect in a superconducting circuit. *Nature* 479, 376 (2011).

95. O. Di Stefano, A. Settineri, V. Macrì, A. Ridolfo, R. Stassi, A. F. Kockum, S. Savasta, and F. Nori. Interaction of Mechanical Oscillators Mediated by the Exchange of Virtual Photon Pairs. *Phys. Rev. Lett.* 122(3), 030402 (2019).

96. J. Błocki, J. Randrup, W. J. Świątecki, and C. F. Tsang. Proximity forces. *Annals of Physics* 105, 427 (1977).

97. G. Barton. Classical van der Waals heat flow between oscillators and between half-spaces. *J. Phys. Condens. Matter* 27, 214005 (2015).

98. M. Aspelmeyer, T. J. Kippenberg, and F. Marquardt. Cavity optomechanics. *Rev. Mod. Phys.* 86, 1391 (2014).

99. Y. Ganjeh, B. Song, K. Pagadala, K. Kim, S. Sadat, W. Jeong, K. Kurabayashi, E. Meyhofer, and P. Reddy. A platform to parallelize planar surfaces and control their spatial separation with nanometer resolution. *Rev. Sci. Instrum.* 83, 105101 (2012).

100. W. J. Kim, A. O. Sushkov, D. A. Dalvit, and S. K. Lamoreaux. Surface contact potential patches and Casimir force measurements. *Phys. Rev. A* 81, 022505 (2010).

101. S. Shen, A. Mavrokefalos, P. Sambegoro, and G. Chen. Nanoscale thermal radiation between two gold surfaces. *App. Phys. Lett.* 100, 233114 (2012).

102. G. Langer, J. Hartmann, and M. Reichling. Thermal conductivity of thin metallic films measured by photothermal profile analysis. *Rev. Sci. Instrum.* 68, 1510 (1997).

103. X. Zhang and C. P. Grigoropoulos. Thermal conductivity and diffusivity of free-standing silicon nitride thin films. *Rev. Sci. Instrum.* 66, 1115 (1995).

104. V. Chiloyan, J. Garg, K. Esfarjani, and G. Chen. Transition from near-field thermal radiation to phonon heat conduction at sub-nanometre gaps. *Nat. Commun.* 6, 6755 (2015).

105. A. O. Sushkov, W. J. Kim, D. A. R. Dalvit, and S. K. Lamoreaux. Observation of the thermal Casimir force. *Nat. Phys.* 7, 230 (2011).

106. R. Kosloff. Quantum thermodynamics: A dynamical viewpoint. *Entropy* 15, 2100 (2013).

107. S. Vinjanampathy and J. Anders. Quantum thermodynamics. *Contemporary Physics* 57, 545 (2016).

108. H. Terças, S. Ribeiro, M. Pezzutto, and Y. Omar. Quantum thermal machines driven by vacuum forces. *Phys. Rev. E* 95, 022135 (2017).